5

Modification of Electric and Magnetic Fields by Materials

Certain materials influence electric and magnetic fields through bound charges and currents. Their properties differ from those of metals where electrons are free to move. Dielectric materials contain polar molecules with spatially displaced positive and negative charge. Applied electric fields align the molecules. The resulting charge displacement reduces the electric field in the material and modifies fields in the vicinity of the dielectric. There are corresponding magnetic field effects in paramagnetic and ferromagnetic materials. These materials contribute to magnetic fields through orientation of atomic currents rather than a macroscopic flow of charge as in a metal.

   Although the responses of materials to fields differ in scale, the general behavior is similar in form. This is the reason the contributions of dielectric and magnetic materials were singled out in Section 4.5 as ρ_2 and j_2 It is often useful to define new field quantities that automatically incorporate the contributions of bound charges and currents. These quantities are **D** (the electric displacement vector) and **H** (the magnetic field intensity).

   The study of the properties of dielectric and magnetic materials (including subsidiary field quantities and boundary conditions) is not conceptually exciting. This is especially true for ferromagnetic materials where there is considerable terminology. Nonetheless, it is essential to understand the properties of dielectric and ferromagnetic materials since they have extensive uses in all types of accelerators.

A partial list of applications of dielectric materials includes the following:

1. Electric field distributions can be modified by adjustment of dielectric-vacuum boundaries. For example, dielectric boundary conditions must be applied to determine optimum shapes of high-voltage vacuum insulators.
2. Dielectrics can store more electrostatic field energy than vacuum. The high-energy storage density of water (80 times that of vacuum) is the basis for much of modern pulsed power technology.
3. Dielectrics reduce the velocity of propagation of electromagnetic waves (or photons). This helps to match the velocities of rf waves and high-energy particles for resonant acceleration. This effect is also important in designing energy storage transmission lines for pulse modulators.

All high-energy accelerators utilize ferromapetic materials. The following are some important applications.

1. Ferromagnetic materials shape magnetic fields. They play a role analogous to electrodes in electrostatics. Shaped iron surfaces (poles) are utilized to generate complex field distributions for focusing and bending magnets.
2. Ferromagnetic materials amplify the flux change produced by a real current. The resulting increased inductance is essential to the operation of transformers. Inductive isolation is the basis of the betatron and linear induction accelerator.
3. Ferromagnetic materials convey magnetic field lines in a manner analogous to the conduction of current by a low-resistivity wire. This effect leads to substantial reductions in power requirements for beam transport magnets.
4. The nonlinear response of a ferromagnetic material to an applied field can be utilized for fast, high-power switching.

The physics of dielectric and ferromagnetic materials is reviewed in this chapter. Special emphasis is placed on the concept of the magnetic circuit. A section is included on permanent magnet circuits.

5.1 DIELECTRICS

Dielectric materials are composed of *polar molecules*. Such molecules have spatially separated positive and negative charge. The molecules may be either bound in one position (solids) or free to move (liquids and gases). Figure 5.la shows a diagram of a water molecule. The electronegative oxygen atom attracts the valence electrons of the hydrogen atoms, leaving an excess of positive charge at the locations of the hydrogen atoms.
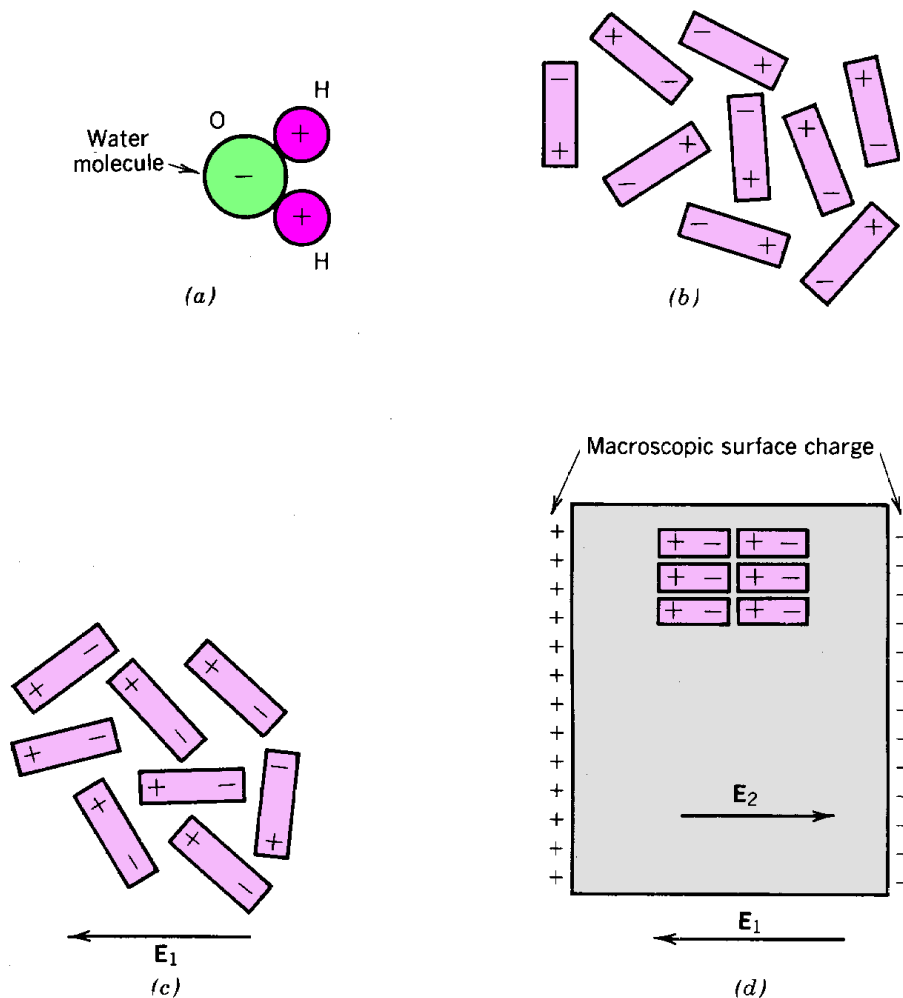
Figure 5.1 Behavior of dielectric materials. (*a*) Polar molecule (water). (*b*) Randomly oriented polar molecules. (*c*) Aligned polar molecules under the influence of an applied electric field. (*d*) Macroscopic charge on the surface of a dielectric material in an applied electric field from the alignment of polar molecules.

In the absence of an applied electric field, the molecules of a dielectric are randomly oriented (Fig. 5.1b). This results from the disordering effects of thermal molecular motion and collisions. Molecular ordering cannot occur spontaneously because a net electric field would result. With no external influence, there is no source of energy to generate such fields (Section 5.6). The randomized state is the state of lowest net energy (thermodynamic equilibrium).

Applied electric fields act on the charges of a polar molecule to align it as shown in Figure 5.1c. On the average, the molecular distribution becomes ordered as the change in electrostatic potential energy counteracts the randomizing thermal kinetic energy. The macroscopic effect of molecular alignment is shown in Figure 5.1d. Inside the material, a shifted positive charge in one molecule is balanced by a shifted negative charge of a nearby molecule. On the average, there

is no net internal charge to contribute to fields. This balance does not occur on the surfaces. An applied electric field results in positive and negative charge layers at opposite surfaces. The field produced by these layers inside the dielectric is opposed to the applied field.

The simplest geometry to consider is a one-dimensional dielectric slab in a region of uniform applied electric field. The applied field is produced by a voltage difference between two parallel plates (Fig. 5.1d). The electric field resulting from the charges on the plates (Section 3.2) is denoted E_1. The surface charges induced on the dielectric produce a field, $-E_2$. The total field inside the dielectric is $E = E_1 - E_2$. Most dielectrics have the property that the degree of orientation of polar molecules is linearly proportional to the applied field at typical field strengths. Thus, the surface charge density is proportional to applied field, and $E_2 \sim E_1$.

The linear response of dielectrics comes about because the degree of alignment of molecules is small at normal temperatures and field strength. Increased applied field strength brings about a proportional increase in the orientation. Nonlinear effects are significant when the dielectric approaches *saturation*. In a saturated state, all molecules are aligned with the field so that an increase in applied field brings about no increase in surface charge. We can estimate the magnitude of the saturation electric field. At room temperature, molecules have about 0.025 eV of thermal kinetic energy. Saturation occurs when the electrostatic potential energy is comparable to the thermal energy. The decrease in potential energy associated with orientation of a polar molecule with charge separation d is qE_1d. Taking $q = e$ and $d = 1$ Å (10^{-10} m), E_1 must be on the order of 250 MV/m. This is much higher than the strongest fields generated in rf accelerators, so that the linear approximation is well satisfied. In contrast, saturation effects occur in ferromagnetic materials at achievable values of applied magnetic field.

The net electric field inside a linear dielectric is proportional to the applied field. The constant of proportionality is defined by

$$E = \frac{E_1}{\varepsilon/\varepsilon_o} = E_1 + E_2. \tag{5.1}$$

The quantity $\varepsilon/\varepsilon_o$ is the relative dielectric constant. Ordinary solid or liquid dielectrics reduce the magnitude of the electric field, so that $\varepsilon/\varepsilon_o > 1$. Equation (5.1) is written in vector notation. This result can be derived from the above one-dimensional arguments by considering a differential cubic volume and treating each component of the field separately. This approach holds if the material is isotropic (liquids, glass). Equation (5.1) may not be valid for some solid materials. For instance, if polar molecules are bound in a crystal lattice, their response to an applied field may vary depending on the orientation of the field with respect to the crystal axes. The dielectric constant depends on the alignment of the field relative to the crystal. Such materials are called bifringent.

Water is a commonly encountered isotropic dielectric medium in electrical energy storage applications. The relative dielectric constant of liquid water is plotted in Figure 5.2 versus temperature and the frequency of an oscillating applied electric field. The low-frequency value is high since water molecules have large charge separation. The dielectric constant decreases with increasing temperature. This comes about because the molecules have higher thermal energy; therefore, they do not align as strongly in an applied electric field. At constant temperature, the relative dielectric constant decreases at high frequency (the microwave regime). This is because the inertia of the water molecules retards their response to the oscillating electric field. The alignment of the molecules lags in phase behind the electric field, so that the medium extracts energy from the field. Thus, water is not an ideal dielectric at high frequency. The loss process is usually denoted by an imaginary part of the dielectric constant, ε''. Higher temperatures randomize molecular motion and lessen the relative effect of the ordered phase lag. This explains the unusual result that the absorption of high-frequency electric fields in water is reduced at higher temperature.

It is useful to define the *displacement vector* **D** when the dielectric is linear. The displacement vector is proportional to the sum of field components excluding the contribution of dielectrics, or (in the notation of Chapter 4)

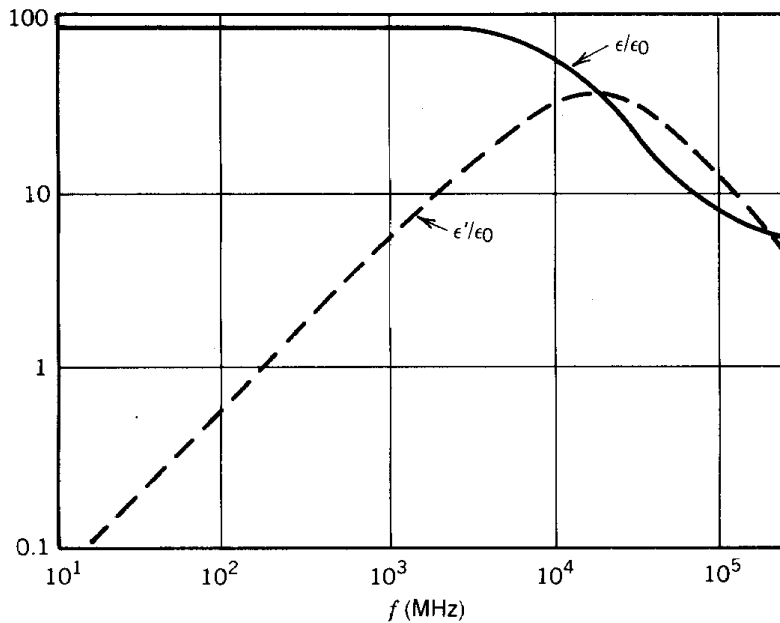$$D = \varepsilon_o \, (E_1 + E_3). \tag{5.2}$$

Figure 5.2 Real and imaginary parts of the relative dielectric constant of water as a function of the applied electric field frequency. (Adapted from J. B. Halstead, "Liquid Water—Dielectric Properties" in *Water—a Comprehensive Treatise*, F. Franks Ed., Plenum, New York, 1972.)

Thus, **D** arises from free charges (either on electrodes or in the volume). Combining Eqs. (5.1) and (5.2) the electric displacement is related to the net field inside a dielectric region by

$$\mathbf{D} = \varepsilon \mathbf{E}. \tag{5.3}$$

If a dielectric is inserted into a vacuum field region (Section 4.1), the following equations hold:

$$\nabla \cdot \mathbf{D} = 0, \quad \nabla \cdot \mathbf{E} \neq 0. \tag{5.4}$$

The meaning of these equations is illustrated in Figure 5.3. A thin differential volume element that includes a vacuum-dielectric boundary is illustrated. There is no flux of **D** lines out of the volume since there are no free charges to act as sources. The divergence of **E** is nonzero because the magnitude is different on both faces. The volume includes a net positive charge in the form of the dielectric surface charge.

When dielectrics are included in a vacuum region, the Laplace equation can be written

$$\nabla \cdot \left(\frac{\varepsilon(\boldsymbol{x})}{\varepsilon_o} \, \nabla \varphi \right) = 0. \tag{5.5}$$

Equation (5.5) proceeds from Eq. (5.4), which implies that $\nabla \cdot \varepsilon \mathbf{E} = 0$. The potential is still given by $-\nabla \varphi = \mathbf{E}$ since the force on a particle depends on the net electric field, independent of the sources of the field. Numerical methods to solve Eq. (5.5) are similar to those of Section 4.2. A
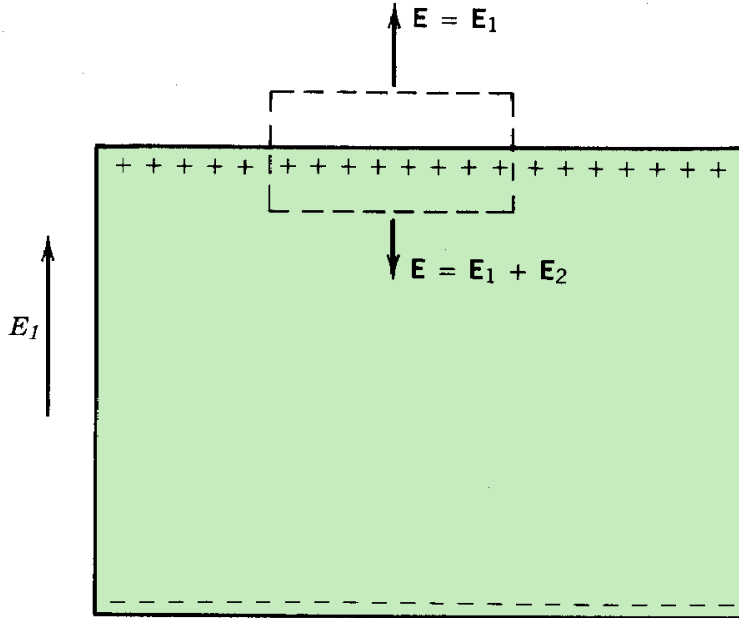

Figure 5.3   Electric fields at a vacuum–dielectric boundary.

value of the relative dielectric constant is associated with each point and must be included in the finite difference formulation of the Laplacian operator.

The concept of the dielectric constant often leads to confusion in treating plasmas. A plasma is a relatively dense region of equal positive and negative free charges (Fig. 5.4). The clearest approach to describe the interactions of plasmas and electric fields is to include the electron and ion space charge as contributions to ρ_3 (free space charge). Nonetheless, it is a common practice to introduce the concept of a plasma dielectric constant to describe phenomena such as the refraction of optical radiation. This permits utilization of familiar optical definitions and equations. Referring to the plasma slab illustrated in Figure 5.4a, the plasma dielectric constant is clearly undefined for a steady-state applied field since positive and negative charges are free to move in opposite directions. At very low frequency, plasmas support real currents, as in a metal conductor. When a medium-frequency ac electric field is applied, the heavy ions are relatively immobile. The electrons try to move with the field, but displacements lead to charge separation. The space charge tield acts to cancel the applied field. The electrons are thus bound to the ions. The result is that at medium frequency, electric fields are excluded from plasmas. Alternatively, the plasma can be described by a relative dielectric constant much greater than unity. Note the geometric similarity between Figure 5.4b and 5.1d. At high frequencies, electron inertia becomes an important factor. At high frequencies (such as the optical regime), the electron motion is $180°$ out of phase with applied electric fields. In this case, the electron space charge (oscillating about the immobile positive charge) adds to the applied field,
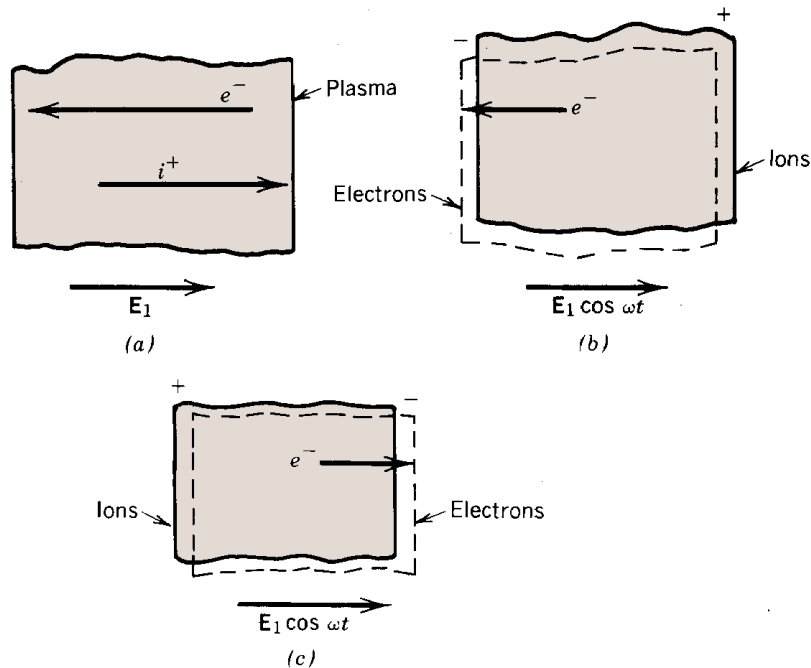

Figure 5.4 Response of particles in a plasma slab to an oscillating applied electric field. (*a*) Direct-current field (zero frequency). (*b*) Low-frequency ac field. (*c*) High-frequency ac field.
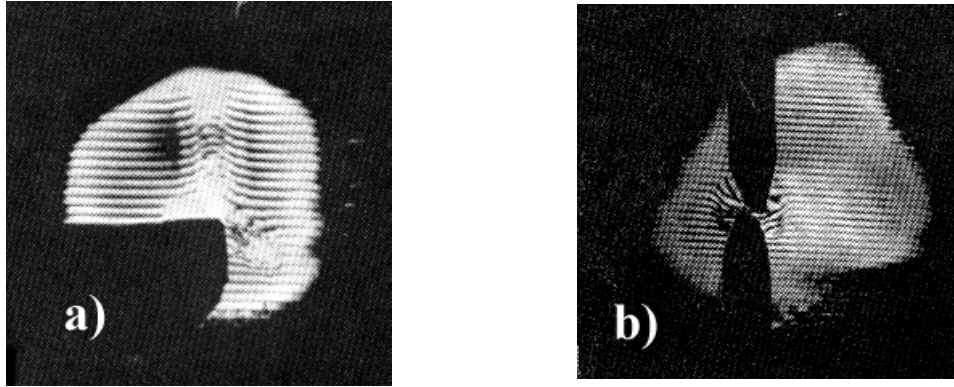
Figure 5.5. Infrared laser interferogram of plasma in dense neutral backgrounds. (a) Exploding wire: note that the dense expanding neutrals cause an upward shift of fringes ($\varepsilon/\varepsilon_o > 1$) while the electrode plasma causes a downward fringe shift ($\varepsilon/\varepsilon_o < 1$). (b) Spark in atmospheric air: dense plasma causes a downward shift. (Photographs by the author.)

so that $\varepsilon/\varepsilon_o < 1$. Plasmas are a very unusual dielectric material at high frequencies. This effect is important in laser interferometry of plasmas. Figure 5.5 shows far-infrared holographic interferograms of an exploding wire and a plasma spark in atmospheric air. The direction of displacement of the fringes shows the dielectric constant relative to vacuum. Note that there are displacements in both directions in Figure 5.5a because of the presence of a dense shock wave of neutrals ($\varepsilon/\varepsilon_o > 1$) and an electrode plasma ($\varepsilon/\varepsilon_o < 1$).

5.2 BOUNDARY CONDITIONS AT DIELECTRIC SURFACES

Methods for the numerical calculation for vacuum electric fields in the presence of dielectrics were mentioned in Section 5.1. There are also numerous analytic methods. Many problems involve uniform regions with different values of $\varepsilon/\varepsilon_o$. It is often possible to find general forms of the solution in each region by the Laplace equation, and then to determine a general solution by

matching field components at the interfaces. In this section, we shall consider how electric fields vary passing from a region with $\varepsilon/\varepsilon_o \neq 0$ to a vacuum. Extensions to interfaces between two dielectrics is straightforward.

   The electric fields at a dielectric-vacuum interface are divided into components parallel and perpendicular to the surface (Fig. 5.6). The magnitude of the electric field is different in each region (Section 5.1); the direction may also change. The relationship between field components normal to the interface is demonstrated by the construction of Figure 5.6b. A surface integral is taken over a thin volume that encloses the surface. The main contributions come from integration over the faces parallel to the surface. Using Eq. (5.3) and the divergence theorem,

$$\iint dA \; (\varepsilon_o E_{\perp\alpha} - \varepsilon E_{\perp\beta}) = 0.$$
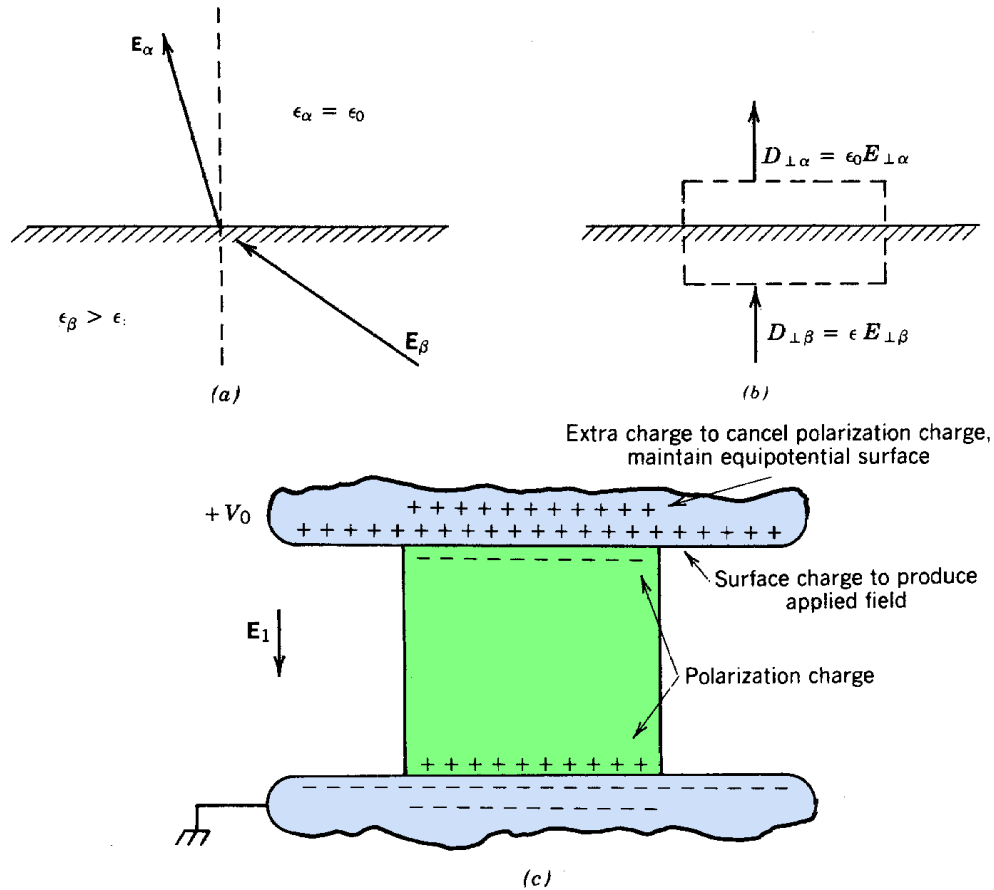

Figure 5.6 Boundary conditions for electric field components at a vacuum–dielectric boundary. (*a*) Electric field lines at boundary. (*b*) Geometry to find the relationship of normal field components. (*c*) Geometry to find the relationship of parallel field components.

This gives the matching condition for perpendicular field components,

$$E_{\perp\beta}/E_{\perp\alpha} \; = \; \varepsilon_o/\varepsilon, \tag{5.6}$$

Matching conditions for the parallel field components can be determined from the construction of Figure 5.6c. A slab of dielectric extends between two parallel metal plates at different voltages. The dielectric-vacuum interface is normal to the plates. The geometry of Figure 5.6c is the simplest form of capacitor. The charges that produce the electric field must be moved against the potential difference in order to charge the plates. During this process, work is performed on the system; the energy can be recovered by reversing the process. Thus, the capacitor is a storage device for electrostatic energy.

   In the absence of the dielectric, electric field lines normal to the plates are produced by positive and negative surface charge layers on the plates. When the dielectric is introduced, polarization charge layers are set up that try to reduce the electric field inside the dielectric. Because there is no net charge between the plates or inside the dielectric, the condition $\nabla\cdot\mathbf{E} = 0$ holds everywhere between the plates. Field lines are thus straight lines parallel to the dielectric-vacuum interface. The integral $-\int\mathbf{E}\cdot\mathbf{dx}$ has the constant value V_o on any path between the equipotential plates. In particular, the integral can be taken just inside and outside the dielectric interface. This implies that the parallel electric field is the same inside and outside the dielectric surface. This fact can be reconciled with the presence of the polarization charge by noting that additional surface charge is distributed on the plates. The extra charge cancels the effect of polarization charge on the electric field, as shown in Figure 5.6 c.

   The matching condition for parallel components of electric field at a dielectric-vacuum surface is

$$E_{\|\alpha} \; = \; E_{\|\beta}. \tag{5.7}$$

The construction also shows that a dielectric fill allows a capacitor to store more plate charge at the same voltage. Since the electrostatic energy is proportional to the charge, the energy density is proportional to $\varepsilon/\varepsilon_o$. This explains the predominance of water as a medium for high-power density-pulsed voltage systems. Compact high-voltage capacitors are produced using barium titanate, which has a relative dielectric constant which may exceed 10^4.

   The combined conditions of Eqs. (5.6) and (5.7) imply that the normal components of electric field lines entering a medium of high $\varepsilon/\varepsilon_o$ from vacuum are small. Inside such a medium, electric field lines are thus bent almost parallel to the interface. Figure 5.7 shows an example of applied dielectric boundary conditions. Equipotential lines are plotted at the output of a high-power, water-filled pulser. The region contains water ($\varepsilon/\varepsilon_o = 80$), a lucite insulator ($\varepsilon/\varepsilon_o \approx 3$), and a vacuum region ($\varepsilon/\varepsilon_o = 1$) for electron beam acceleration. The aim of the designer was to distribute equipotentials evenly across the vacuum side of the insulator for uniform field stress and to shape boundaries so that field lines enter the surface at a 45' angle for optimum hold-off (see Section
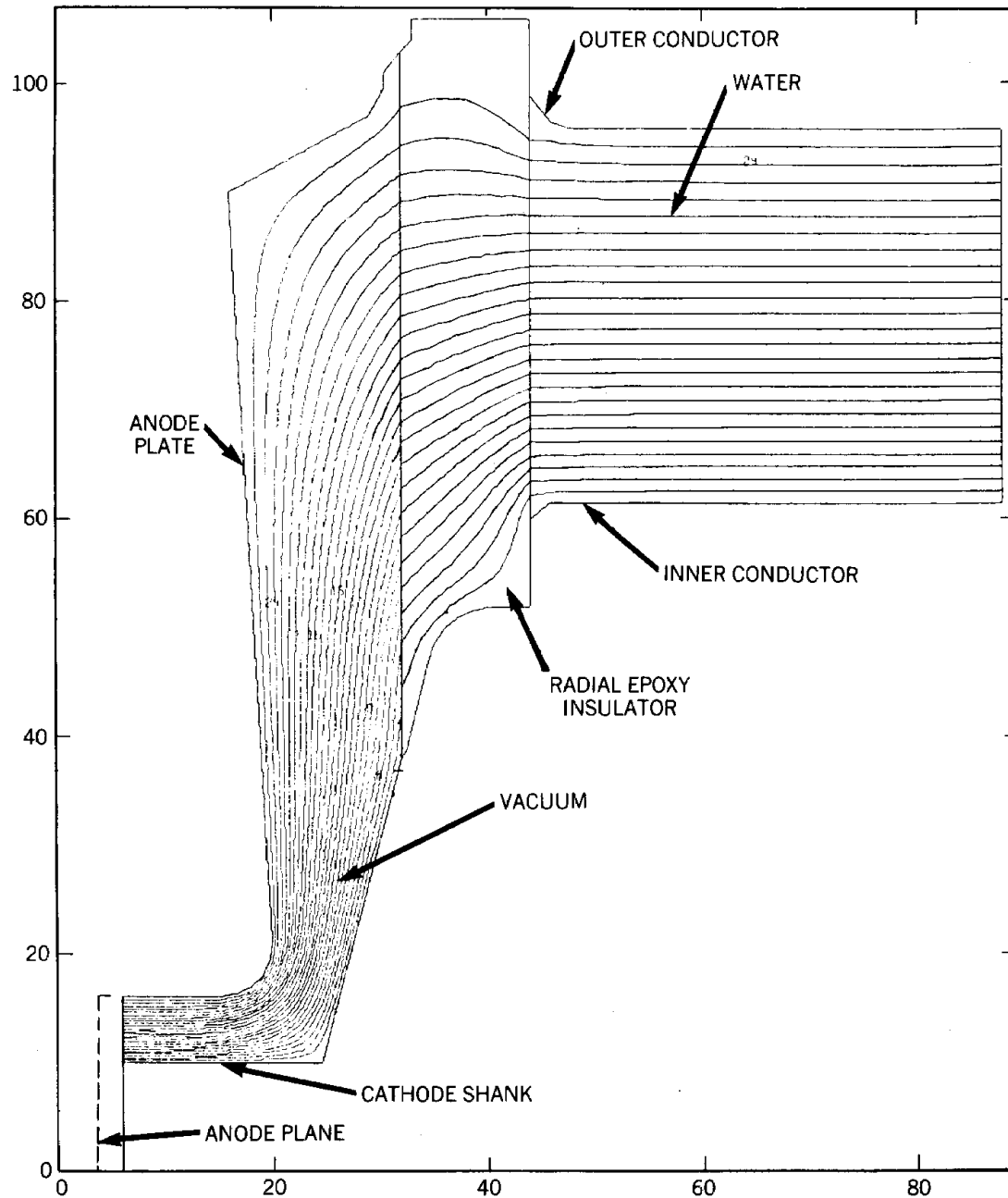
Figure 5.7 Equipotential lines near the vacuum insulator of a high-power pulse generator. (Courtesy J. Benford, Physics International Company.)

9.5). Note the sharp bending of equipotential lines at the lucite-water boundary. The equipotentials in the water are evenly spaced straight lines normal to the boundary. They are

relatively unaffected by the field distribution in the low dielectric constant region.

5.3 FERROMAGNETIC MATERIALS

Some materials modify applied magnetic fields by alignment of bound atomic currents. Depending on the arrangement of electrons, atoms may have a magnetic moment. This means that the circulating electrons produce magnetic fields outside the atom. The fields, illustrated in Figure 5.8, have the same form as those outside a circular current loop (Section 4.7); therefore, the circular loop is often used to visualize magnetic interactions of atoms. The magnetic moment p_m of a loop of radius a carrying a current I is
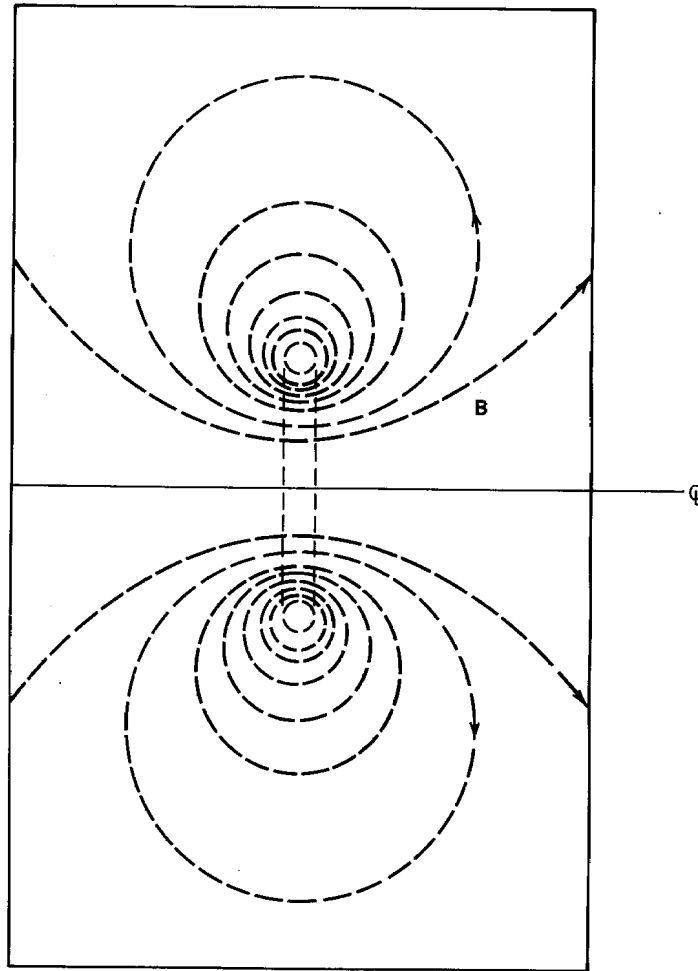
$$p_m = I \ (\pi a^2). \tag{5.8}$$

Figure 5.8 Magnetic field lines near an atom with a magnetic moment.

87

In classical physics, the atomic p_m is visualized to originate from the circular current loop of a valenc electron rotating about the atom. The current I is about $qev/2\pi a$ (where v is the orbital velocity) and a is about 1 Å. Although this gives a rough estimate of a typical atomic p_m the microscopic problem must be approached by quantum mechanics. The correct result is that the magnetic moment is quantified, and can have values

$$p_m = \pm meh/4\pi m_e, \tag{5.9}$$

where h is the Planck constant

$$h = 6.63 \times 10^{-34} \ J\text{-}s,$$

and m is an integer which depends on the arrangement of electrons in the atom.

On a macroscopic scale, when two fixed adjacent current loops have the same orientation, the magnetic forces act to rotate the loops to opposite polarity (Fig. 5.9a). This is a consequence of the fact that when the magnetic moments are aligned antiparallel, magnetic fields cancel so that the field energy is minimized. With no applied field, atomic currents are oriented randomly, and there is no macroscopic field. The situation is analogous to that of molecules in a dielectric. Material that can be described by this classical viewpoint is called *paramagnetic*, which means "along or parallel to the field." Reference to Figure 5.9b shows that when a magnetic field is applied to a paramagnetic material, the atomic currents line up so that the field inside the loop is in the same direction as the applied field while the return flux is in opposition. As in dielectrics, the fractional alignment is small since the change in magnetostatic energy is much less than the average thermal energy of an atom. Figure 5.9c shows what the net magnetic field looks like when magnetic moments of atoms in a dense medium are aligned; there is an increase of magnetic flux inside the material above the applied field. Negative flux returns around the outside of the material. A view of the atomic and real currents normal to the applied field clarifies the process (Fig. 5.9d). Alignment of magnetic moments does not produce a net atomic current inside the material, but results in a surface current in the same direction as the applied field. The surface current is the magnetic analogy of the surface charge of dielectrics.

The field inside a paramagnetic material is approximately proportional to the applied field, or

$$\boldsymbol{B} = (\mu/\mu_o) \ \boldsymbol{B_1} = \boldsymbol{B_1} + \boldsymbol{B_2}. \tag{5.10}$$

The quantity μ/μ_o is the *relative permeability*. The magnetic field intensity $\mathbf{H}$ is a vector quantity proportional to the magnetic field minus the contribution of atomic material currents, or

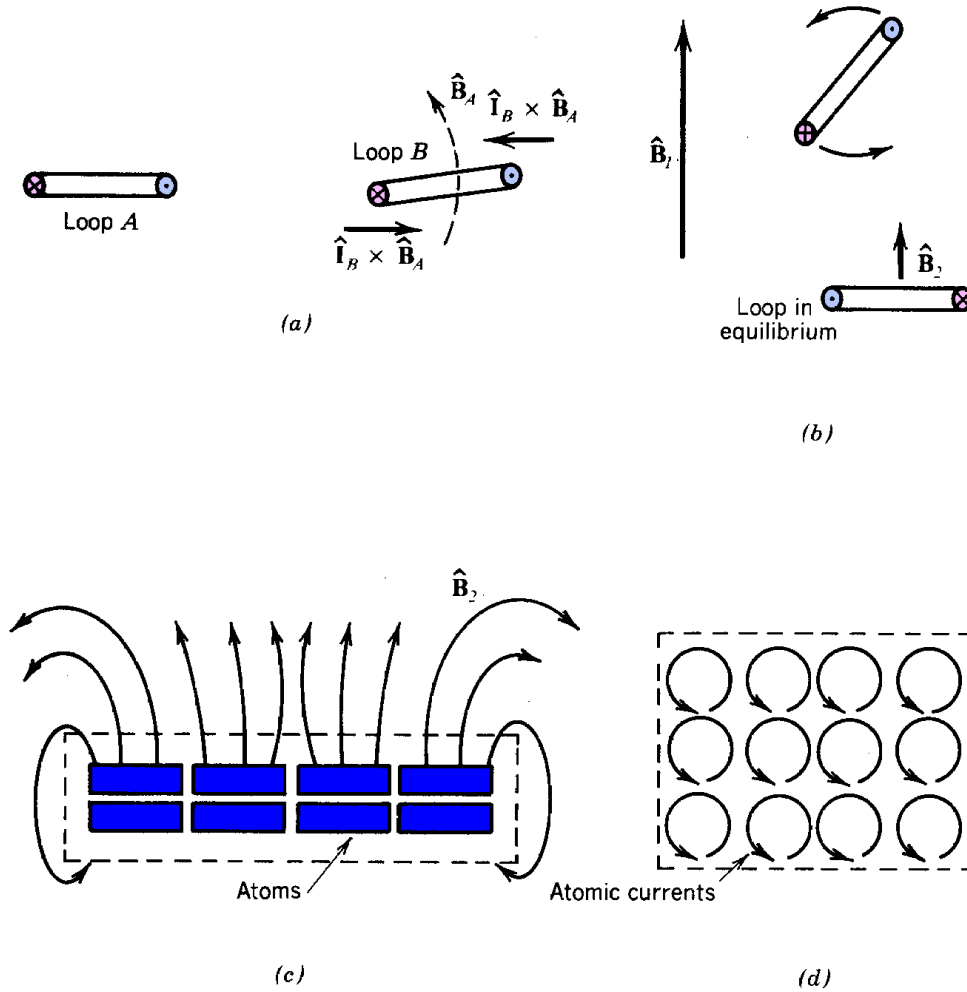$$\boldsymbol{H} = \boldsymbol{B_1}/\mu_o.$$

Figure 5.9 Behavior of magnetic materials. (*a*) Interactions between atoms with magnetic moments; force exerted on one current loop (*B*) by another (*A*). (*b*) Response of atoms in a paramagnetic material to an applied magnetic field. (*c*) Macroscopic magnetic fields produced by alignment of atomic currents in a material. (*d*) Macroscopic surface current in a material resulting from alignment of atoms with magnetic moments.

The field intensity is related to the magnetic field inside a magnetic material by

$$H = B/\mu. \tag{5.11}$$

Magnetic fields obey the principle of superposition. Equation (4.39) can be written

$$\int B_1 \cdot dl = \mu_o I_1.$$

for the applied fields. This can be expressed in terms of H by

$$\int \mathbf{H \cdot dl} = I_1. \tag{5.12}$$

Thus, the magnetic intensity is determined only by free currents and has the dimensions amperes per meter in the mks system.

The relative permeability in typical paramagnetic materials is only about a factor of 10^{-6} above unity. Paramagnetic effects are not important in accelerator applications. Ferromagnetic materials, on the other hand, have μ/μ_o factors that can be as high as 10,000. This property gives them many important uses in magnets for charged particle acceleration and transport. Ferromagnetism is a quantum mechanical phenomenon with no classical analogy. In some materials (chiefly iron, nickel, and iron alloys), the minimum energy state consistent with the exclusion principle has atomic magnetic moments aligned parallel rather than antiparallel. The energy involved in this alignment is greater than thermal kinetic energies at room temperature. On a microscopic scale, all the magnetic moments in a ferromagnetic material are aligned in the minimum energy state.

Alignment does not extend to macroscopic scales. Macroscopic alignment of magnetic moments produces fields outside the material which require additional energy. Two opposing factors are balanced in ferromagnetic materials in the minimum energy state. On the microscopic scale, minimum energy is associated with atomic alignment, while on the macroscopic scale minimum energy is equivalent to maximum disorder. The situation is resolved by the formation of domains, small regions in which all magnetic moments are aligned. On a macroscopic scale, the domains are randomized (Fig. 5.10) so that there is no magnetic field outside the ferromagnetic material in its ordinary state. The domain size (the separatrix between the quantum mechanical and classical regimes) is about 10^{-5} cm, or 1000 atoms wide.

Ferromagnetic materials respond to applied magnetic fields by shifting domain boundaries to favor domains aligned with the field. In contrast to paramagnetic materials, the resulting high degree of atomic orientation produces large magnetic effects. Saturation (total alignment) can occur at attainable applied field strengths (~2 T). Although the magnetic field is a monotonic
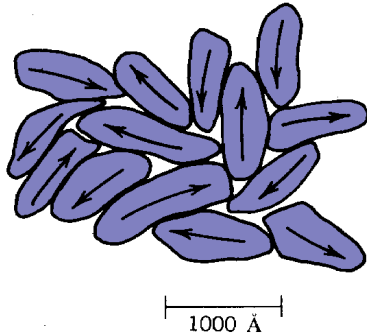

1000 Å

Figure 5.10 Random orientation of domains in unmagnetized material.

90

function of the applied field, we cannot expect the response to be linear or reversible. Equation (5.11) is no longer valid. We can preserve the concept of the permeability by considering the response of ferromagnetic materials to small excursions in the applied field about an equilibrium value. The small signal μ is defined by

$$\Delta B \ = \ \mu(H) \ \Delta H. \tag{5.13}$$

or

$$\mu(H) \ = \ (dB/dH)_H.$$

5.4 STATIC HYSTERESIS CURVE FOR FERROMAGNETIC MATERIALS

In this section we shall look in more detail at the response of ferromagnetic materials to an applied field. In unmagnetized material, the directions of domains are randomized because energy is required to generate magnetic fields outside the material. If the external magnetic field energy is supplied by an outside source, magnetic moments may become orientated, resulting in large amplified flux inside the material. In other words, an applied field tips the energy balance in favor of macroscopic magnetic moment alignment.

   A primary use of ferromagnetic materials in accelerators is to conduct magnetic flux between vacuum regions in which particles are transported. We shall discuss relationships between fields inside and outside ferromagnetic materials when we treat magnetic circuits in Section 5.7. In this section we limit the discussion to fields confined inside ferromagnetic materials. Figure 5.11 illustrates such a case; a ferromagnetic torus is enclosed in a tight uniform magnet wire winding. We want to measure the net toroidal magnetic field inside the material, B, as a function of the applied field B_1, or the field intensity H. The current in the winding is varied slowly so that applied field permeates the material uniformly. The current in the winding is related to B_1 through Eq. (4.42). By Eq. (5.1 1), $H = NI/L$, hence the designation of H in ampere-turns per meter. The magnetic field inside the material could be measured by a probe inserted in a thin gap. A more practical method is illustrated in Figure 5.11. The voltage from a loop around the torus in integrated electronically. According to Section 3.5, the magnetic field enclosed by the loop of area A can be determined from $B = \int Vdt/A$.

   With zero current in the windings, a previously unmagnetized core has randomly orientated domains and has no macroscopic magnetization ($H = 0, B = 0$). Domains become aligned as the applied field is raised. Both H and B increase, as shown in Figure 5.12. The field in the material (the sum of the applied and atomic contributions) may be over 1000 times that of the applied field alone; thus, the small signal μ is high. At some value of applied field, all the domains are aligned. This is called *saturation*. Beyond this point, there is no increase in the contribution of
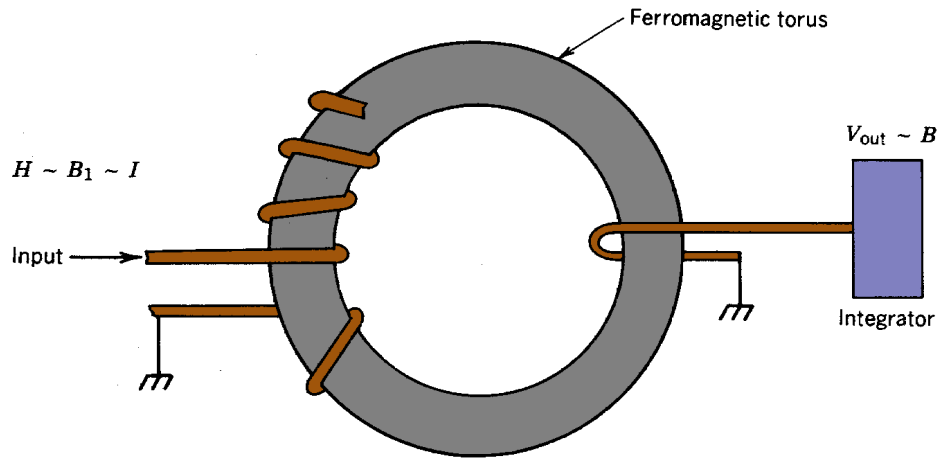
Figure 5.11 Circuit to measure response of atomic currents in a ferromagnetic material.

material currents to the field with increasing applied field; therefore, the small signal μ drops to μ_o. The portion of the *B-H* curve from ($H = 0$, $B = 0$) to saturation (the dashed line in Fig. 5.12) is called the *virgin magnetization curve*. Unless the material is completely demagnetized, it will not be repeated again.

The next step in the hypothetical measurement is to reduce the applied field. If the magnetization process were reversible, the B-H curve would follow the virgin magnetization
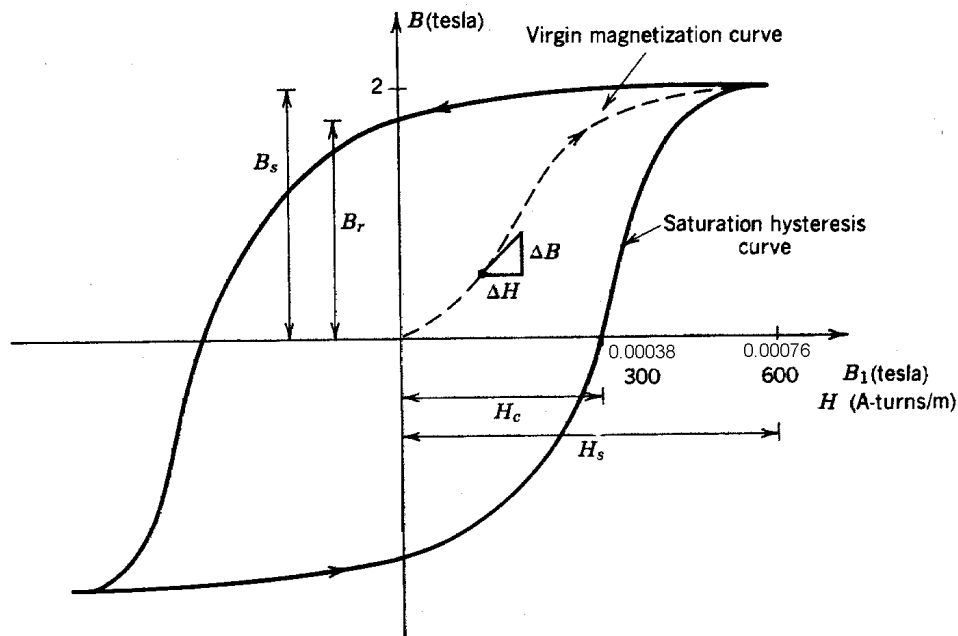

Figure 5.12 Hysteresis curve.

92

curve back to the origin. This does not happen since it takes energy to shift domain boundaries. When *H* is returned to zero, the domains are energetically able to retain much of their alignment so that the torus remains magnetized. This occurs because all field lines are contained in the torus and no energy need be expended to produce external fields. The magnetization would be reduced if there were an air gap in the core (see Section 5.8). If a reverse current is applied to the driving circuit, the magnetic field will return to zero and eventually be driven to reverse saturation. The *B-H* curve of a magnetic material exhibits *hysteresis* or nonreversibility. The term derives from a Greek word meaning shortcoming or lagging. The B-H curve described is a particular case, the *saturation hysteresis curve*. There is a nested family of hysteresis curves converging to the origin, depending on the magnitude of current in the driving circuit.

   Magnet engineering is based on some straightforward concepts and a large body of terminology. A clear understanding of the definitions of magnetic properties is essential to utilize data on magnetic materials. To facilitate this, important terms will be singled out in this section and in Sections 5.7 and 5.8. Terms related to the hysteresis curve are illustrated in Figure 5.12. Most data on magnetic materials and permanent magnets is given in cgs units, so it is important to know the transformation of quantities between mks and cgs.

H   Magnetic Intensity. Also called magnetizing force. The cgs unit is oersteds (Oe), where I A-turn/m = 0.01256 Oe.

B   Magnetic Induction Field. Also called magnetic field, magnetic induction, magnetic flux density. The cgs unit is the gauss (G), where 1 tesla (T) = 10^4 gauss.

B_s Saturation Induction. The magnetic field in a ferromagnetic material when all domains are aligned.

H_s   The magnetizing force necessary to drive the material to saturation.

H_c Coercive Force. The magnetic intensity necessary to reduce the magnetization of a previously saturated material to zero.

B_r Remanence Flux. Also called residual induction. The value of the magnetic field on the saturation hysteresis curve when the driving current is zero. It is assumed that all magnetic flux is contained in the material.

Soft Magnetic Material. Ferromagnetic materials which require a small magnetizing force to be driven to saturation, typically 10 Oe. The area enclosed by the saturation hysteresis curve is relatively small, and we shall see that this is equivalent to small energy input to magnetize or demagnetize the material. Soft magnetic materials are used to conduct field lines and as isolators in induction accelerators.

Hard Magnetic Materials. Ferromagnetic materials which require considerable energy to reorient the domains. The coercive force can be as high as 8000 Oe. The large amount of energy stored in hard magnetic materials during magnetization means that more energy is available to produce fields external to the material. Hard magnetic materials are used for permanent magnets.
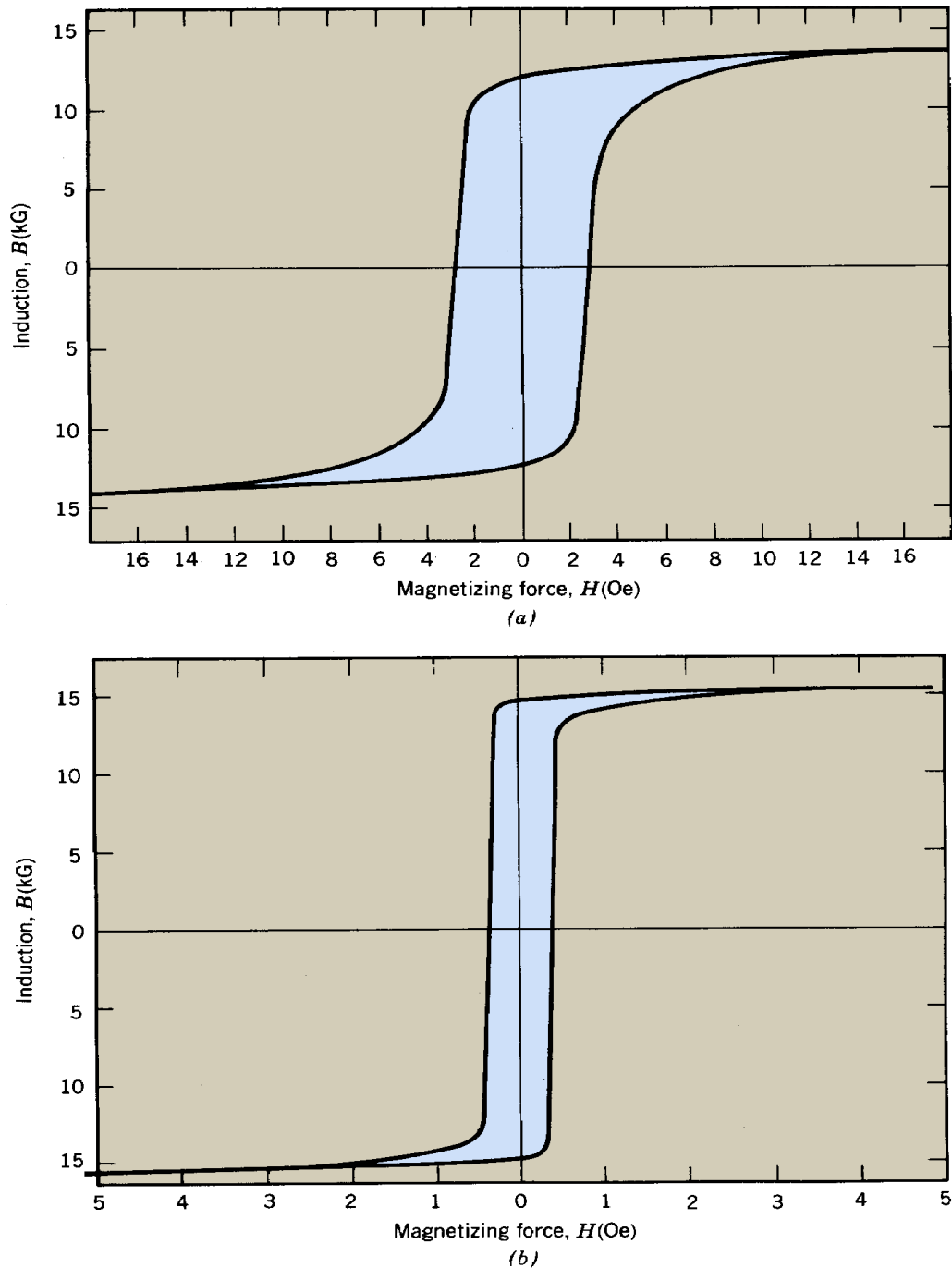

Figure 5.13 Saturation hysteresis curves. (*a*) Low-carbon steel. (*b*) Steel with 3.25% silicon. (Courtesy M. Wilson, National Bureau of Standards.)

94

Figure 5.13 shows hysteresis curves for carbon steel (a material used for magnet poles and return flux yokes) and silicon steel (used for pulsed transformer cores).

5.5 MAGNETIC POLES

Figure 5.14 shows a boundary between a magnetic material with permeability μ and vacuum with μ_o. A thin volume element encloses the boundary. The equation $\nabla \cdot \mathbf{B} = 0$ implies that the integral of the normal component of $\mathbf{B}$ on the surfaces of the volume is zero (Fig. 5.14a). The main contributions to the integral are from the upper and lower faces, so that

$$B_{\perp \alpha} = B_{\perp \beta}. \tag{5.14}$$

Noting that there is no free current enclosed, Eq. (5.12) can be applied around the periphery of the volume (Fig. 5.14b). The main contributions to the circuital integral are on the faces.

$$\int (\mathbf{H}_\alpha - \mathbf{H}_\beta) \cdot \mathbf{dl} = \tag{5.15}$$

or

$$B_{\| \alpha}/\mu_o = B_{\| \beta}/\mu. \tag{5.16}$$

For ferromagnetic materials ($\mu \gg \mu_o$), the parallel component of magnetic field outside the ferromagnetic material is much smaller than the parallel component inside the material. Thus, magnetic field lines just outside a ferromagnetic material are almost normal to the surface. This simple boundary condition means that ferromagnetic materials define surfaces of constant
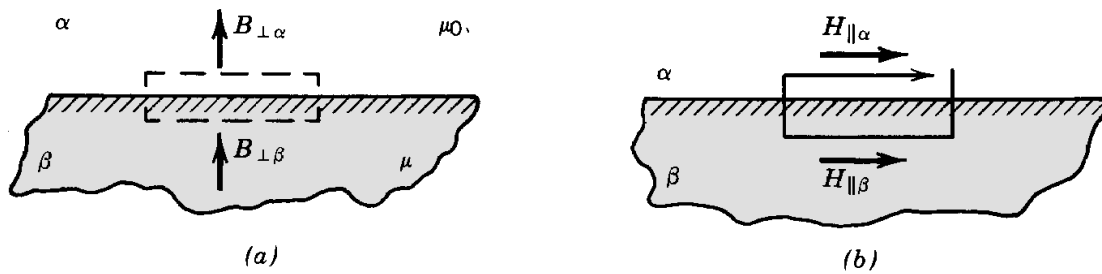

Figure 5.14 Boundary conditions for magnetic field components at a boundary between vacuum and a ferromagnetic material. (a) Geometry to find the relationship of normal field components. (b) Geometry to find the relationship of parallel field components.

magnetic potential U_m. Ferromagnetic surfaces can be used to generate magnetostatic field distributions in the same way that electrodes are used for electrostatic fields. Since both the electrostatic and magnetic potentials satisfy the Laplace equation, all electrostatic solutions can be applied to magnetic fields. Ferromagnetic surfaces used to shape magnetic field lines in a vacuum (or air) region are called *pole pieces*. By convention, magnetic field vectors point from the North to the South pole. Figure 5.15 shows an example of a numeric calculation of magnetic fields for a synchrotron magnet. Shaping of the pole piece near the gap provides the proper field gradient for beam focusing.

The boundary condition is not valid when the pole material becomes saturated. In high-field magnets, regions of high flux may become saturated before rest of the pole piece. This distorts the magnetic field pattern. The fields of partially saturated magnets are difficult to predict. Note that local saturation is avoided in the design of Figure 5.15 by proper shaping and avoidance of sharp edges. This allows the maximum magnetic field without distortion. In the limit of fields well above the saturation limit (» 2 T), the effective relative permeability decreases to unity and the field pattern approaches that of the exciting coil only.

   The analogy between electrostatic and magnetostatic solutions leads to the magnetic quadrupole, illustrated in Figure 5.16. The pole pieces follow hyperbolic surfaces of constant magnetic potential [Eq. (4.26)]. In contrast to the electrostatic quadrupole, the *x-y* forces on a beam moving along the *z* axis are perpendicular to the magnetic field lines. It is usually more convenient to analyze a magnetic quadrupole in terms of *x-y* axes rotated 45° from those used for
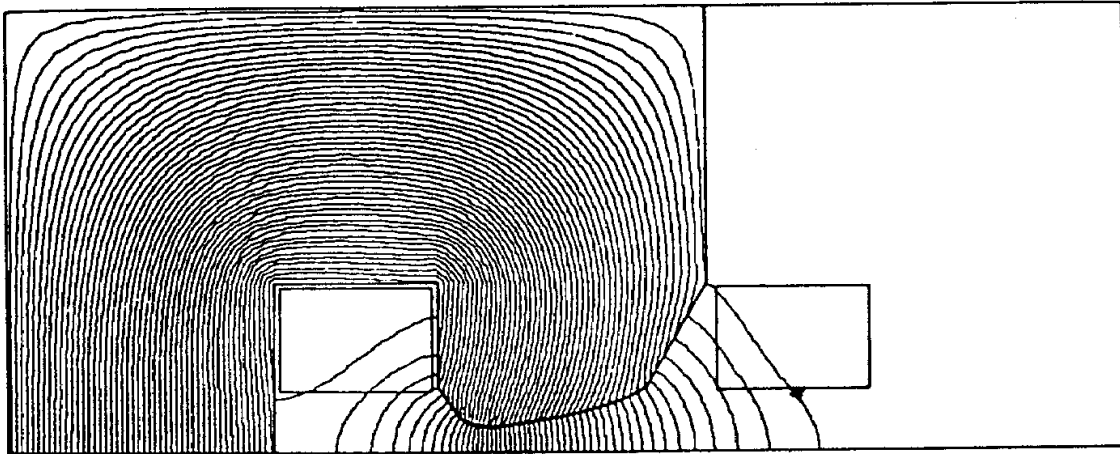

Figure 5.15   Numerical calculation of magnetic field lines in a synchrotron magnet. (Adapted from J. S. Colonias, *Particle Accelerator Design*; *Computer Programs*, used by permission, Academic Press.)
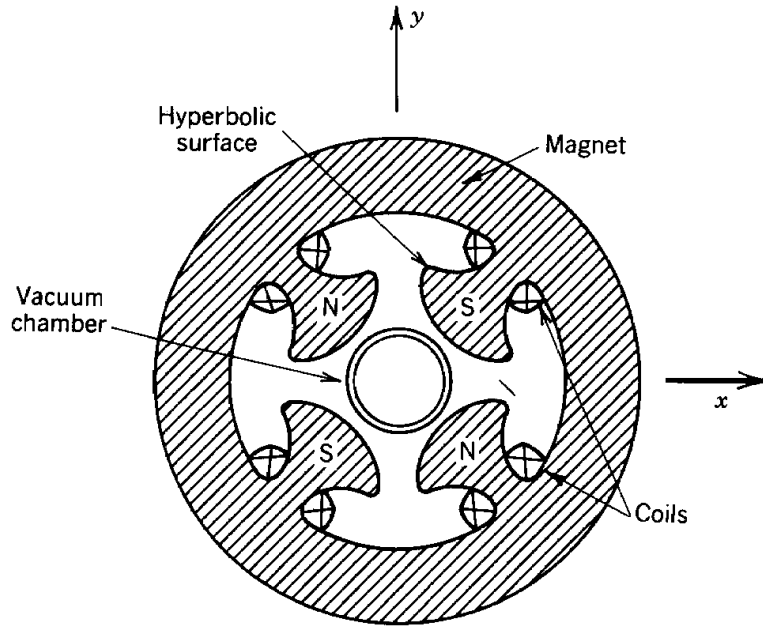
Figure 5.16 Magnetic quadrupole lens (cross section).

the electric field version. In the coordinate system of Figure 5.16, the magnetic field components are

$$B_x = B_o y/a, \quad B_y = B_o x/a. \tag{5.17}$$

5.6 ENERGY DENSITY OF ELECTRIC AND MAGNETIC FIELDS

As mentioned in Section 3.2, the field description summarizes the electromagnetic interactions between charged particles. Although exchange of energy in a system takes place between charged particles, it is often more convenient to imagine that energy resides in the fields themselves. In this section, we shall use two examples to demonstrate the correspondence between the electromagnetic energy of particles and the concept of *field energy density*.

  The electric field energy density can be determined by considering the parallel plate capacitor (Fig. 5.6c). Initially, there is no voltage difference between the plates, and hence no stored charge or energy. Charge is moved slowly from one plate to another by a power supply. The supply must perform work to move charge against the increasing voltage. If the plates have a voltage V', the differential energy transfer from the power supply to the capacitor to move an amount of charge dQ' is $\Delta U = V'dQ'$. Modifying Eq. (3.9) for the presence of the dielectric, the electric field is related to the total charge moved between the plates by

$$E = \frac{Q/A}{\varepsilon},$$

where A is the area of the plates. In terms of incremental quantities during the charging cycle, $dQ' = \varepsilon\, dE'A$. The voltage is related to the field through $V' = E'd$. The total energy stored in the capacitor proceeding from zero electric field to E is

$$U = \int_0^E (E'd)\ (\varepsilon A dE') = (\varepsilon E^2/2)\ (Ad). \tag{5.18}$$

   The total energy can be expressed as the product of an energy density associated with the field lines times the volume occupied by field (Ad). The electrostatic energy density is thus

$$U(E) = \varepsilon E^2/2 = \mathbf{D}\cdot\mathbf{E}/2. \quad (J/m^3) \tag{5.19}$$

The last form is the three-dimensional extension of the derivation.
   The magnetic field energy density can be calculated by considering the toroidal core circuit of Figure 5.11. Because the core is ferromagnetic, we will not assume a linear variation and well-defined μ. The coil has N turns around a circumference C. A power supply slowly increases the current in the coil. To do this, it must counteract the inductive voltage V'. The energy transferred from the power supply to the circuit is $\int V'Idt$. The inductive voltage is $V' = NA(dB'/dt)$, where B' is the sum of contributions to the field from I and the atomic current of the material. The applied field is related to the circuit current by $B_1 = \mu_o NI/C$. Summarizing the above considerations,

$$U = \int_0^B NA\ \frac{dB'}{dt}\ \frac{B_1 C}{N\mu_o} = AC \int_0^B H\ dB'. \tag{5.20}$$

Recognizing that the volume occupied by fields is AC, the magnetic field energy density is

$$U(B) = \int_0^B H\ dB'\quad (J/m^3). \tag{5.21}$$

If the relationship between B and H is known, the energy density of the final state can be evaluated. For instance, with a linear variation (constant μ)

$$U(B) = B^2/2\mu = \mathbf{H}\cdot\mathbf{B}/2\quad (J/m^3). \tag{5.22}$$

The magnetic field energy density in vacuum is $B^2/2\mu^o$.
   The magnetic field energy density can be determined for nonlinear materials given the appropriate B-H curve. For instance, consider magnetizing a ferromagnetic toroidal core following the saturation hysteresis curve (Fig. 5.17a). Assume initially that the material is biased
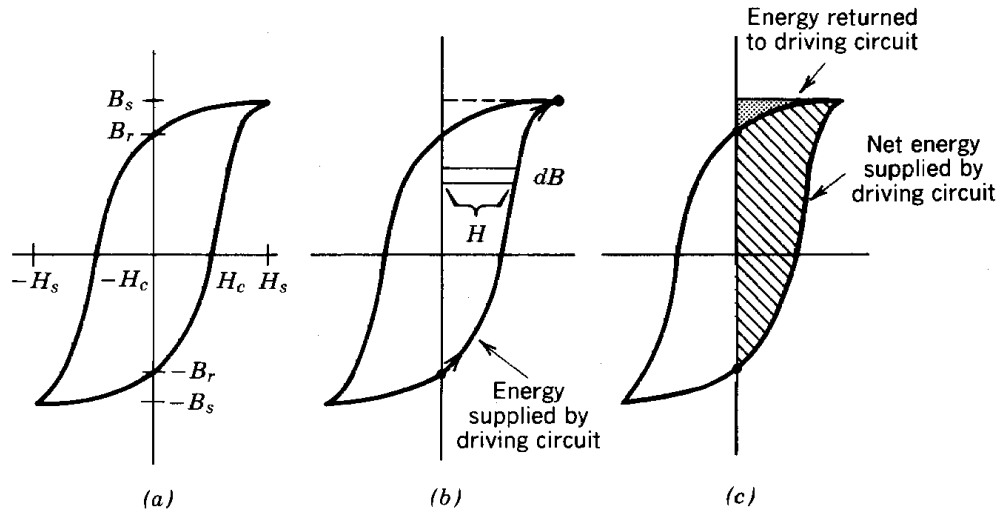
Figure 5.17 Energy required to magnetize and demagnetize a ferromagnetic material. (*a*) Saturation hysteresis curve. (*b*) Quantities to calculate energy changes moving along saturation hysteresis curve. (*c*) Energy supplied by circuit (cross-hatched area) and energy returned to circuit (shaded portion).

to $-B_r$ and a positive driving current is applied to bring it to $+B_s$ (Fig. 5.17b). Both H and dB are positive, so work must be performed by the power source. The energy transfer is given by the shaded area of the graph (Fig. 5.17c) multiplied by the volume of the core. If the power supply is turned off, the core returns to $+B_r$. During this part of the cycle, H is positive but dB is negative, so that some energy is returned to the supply as an induced voltage. This energy is denoted by the darkly shaded portion of the graph; the net energy transfer in a half-cycle is the lightly shaded remainder. A similar process occurs for negative H. In most induction accelerators, a full cycle is traversed around the saturation hysterests curve for each beam pulse. An amount of energy equal to the area circumscribed by the hysteresis curve is lost to the core in each full cycle. This energy is expended in the irreversible process of domain reorientation. It ultimately appears in the core in the form of heat. In applications with continued and rapid recycling, it is clearly advantageous to use a ferromagnetic material with the smallest hysteresis curve area (soft material).

5.7 MAGNETIC CIRCUITS

Magnetic fields used for charged particle transport are usually localized to small regions. This is the case for a bending magnet where the beam traverses a narrow vacuum region of parallel field lines. The condition of zero divergence implies that the field lines must curve around outside the transport region to return to the gap. Thus, most of the volume occupied by magnetic field serves no purpose for the application. If the surrounding region is vacuum or air ($\mu/\mu_o = 1$), most of the power input to the magnet is consumed to support the return flux. A more practical geometry for a bending magnet uses ferromagnetic material in the return flux region. We shall see that in this

case magnetic flux outside the gap is supported by the atomic currents in the material, with very little power required from the external supply.

The bending magnet is a circuit in the sense that the magnetic field lines circulate. The *magnetic circuit* has many analogies with electric circuits in which electrons circulate. The excitation windings provide the motive force (voltage), the vacuum gap is the load (resistance), and the ferromagnetic material completes the circuit (conducting wire). The magnetic circuit with iron is useful primarily when there is a small, well-defined gap. In applications requiring large-volume extended fields (such as hot plasma confinement devices for fusion reactors), there is little benefit in using ferromagnetic materials. Furthermore, ferromagnetic materials lose their advantages above their saturation field (typically 2 T). High-field applications (~ 6 T) have become practical through the use of superconductors. There is no energy penalty in supporting return flux lines in vacuum since the excitation windings draw no power.

Figure 5.18 illustrates the advantage of including ferromagnetic material in ordinary magnetic circuits. Assume that both the air core and iron core geometries produce the same field, B_g, in equal gaps. In order to compare the circuits directly, windings are included in the air core circuit so that the return flux is contained in the same toroidal volume. The magnetic flux in any cross section is a constant and is the same for both circuits. The gap has cross-sectional area A_g, and the core (or return flux coil) has area A_c. The length of the gap is g, while the length of the core (coil) is l. The excitation coils have an ampere turn product given by the number of windings multiplied by the current input to the windings, NI. The wires that carry the current have resistivity in an ordinary magnet; the power necessary to support the field is proportional to N (the length of the wire) and to I^2. It is desirable to make NI as small as possible.

The ampere turn products for the two circuits of Figure 5.18 can be related to the magnetic field in the circuit through Eq. (5.12):

$$\int (\boldsymbol{B}/\mu) \cdot \boldsymbol{dl} = NI. \tag{5.23}$$

The constant circuit flux is given by

$$\Psi = B_g A_g = B_c A_c. \tag{5.24}$$

For the air core circuit, Eq. (5.23) becomes

$$B_g\, (g/\mu_o) + B_c\, (l/\mu_o) = NI,$$

or

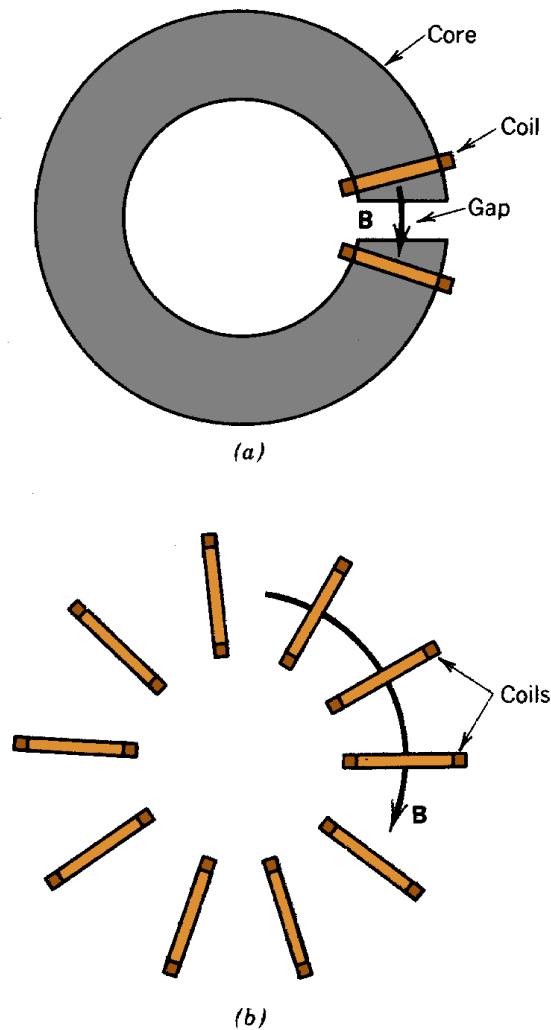$$\Psi\, (g/A_g \mu_o + l/A_c \mu_o) = NI. \tag{5.25}$$

Figure 5.18 Comparison of energy required to generate a gap field by (*a*) an iron core magnet and (*b*) an air core magnet.

Similarly, the following equation describes the ferromagnetic circuit:

$$\Psi \ (g/A_g\mu_o \ + \ l/A_c\mu) \ = \ NI. \tag{5.25}$$

Comparing Eqs. (5.25) and (5.26), the ampere turn product for equal flux is much smaller for the case with the ferromagnetic core when $\mu \ll \mu_o$ and $g \ll l$ (a small gap).

An iron core substantially reduces power requirements for a de magnet. An alternate view of the situation is that the excitation coil need support only the magnetic field in the gap since the second term in Eq. (5.26) is negligible. The return flux is supported by the atomic currents of the material. The excitation coils are located at the gap in Figure 5.18a to clarify this statement. In practice, the coils can be located anywhere in the circuit with about the same result. This follows

101

from the Laplace equation which implies that the field line configuration minimizes the net field energy of the system. The field energy is a minimum if the flux flows in the ferromagnetic material. The field lines are thus conducted through the core and cross the gap in a manner consistent with the boundary condition discussed in Section 5.5, relatively independent of the location of the exciting coils. Ferromagnetic materials also help in pulsed magnet circuits, such as those in the betatron. The *duty cycle* (time on/time off) of such magnets is usually low. Thus, the total field energy is of greater concern than the instantaneous power. Energy for pulsed fields is usually supplied from a switched capacitor bank. A ferromagnetic return flux core reduces the circuit energy and lowers the cost and size of the capacitor bank.

To summarize, ferromagnetic materials have the following applications in non-superconducting accelerator magnets:

      1.The iron can be shaped near the gap to provide accurate magnetic field gradients.
      2.The exciting coil power (or net field energy) is reduced significantly compared to an air core circuit.
      3.The iron conducts flux lines so that the exciting windings need not be located at the gap.

Equation (5.26) has the same form as that for an electric circuit consisting of a power source and resistive elements with the following substitutions.

Magnetic Flux Ψ. The analogy of current in an electric circuit. Although the magnitude of B may vary, the flux in any cross section is constant.

Magnetomotive Force. (Ampere turn product, NI.) The driving force for magnetic flux. Magnetomotive force corresponds to the voltage in an electric circuit.

Reluctance. Corresponds to the resistance. Equation 5.26 contains two reluctances in series, $R_g = g/A_g\mu_o$ and $R_c = l/A_c\mu$. The higher the reluctance, the lower the flux for a given magnetomotive force. The reluctance of the iron return flux core is much smaller than that of the gap (the load), so it acts in the same way as a low-resistivity wire in an electric circuit.

Permanence. The inverse of reluctance and the analogue of conductance.

The circuit analogy is useful for estimating operating parameters for complex magnets such as those found in electric motors. To illustrate a magnetic field calculation, consider the spectrometer magnet illustrated in Figure 5.19a. The components of reluctance already mentioned can be supplemented by additional paths representing fringing flux (magnetic field lines bulging out near the gap) and leakage flux (magnetic flux returning across the magnetic yoke without traversing the gap). These reluctances can be determined by a solution of the Laplace equation for the magnet. Reluctances are combined in series and in parallel, just as resistances. The equivalent circuit is illustrated in Figure 5.19b. The effect of leakage flux on the field in the gap can be
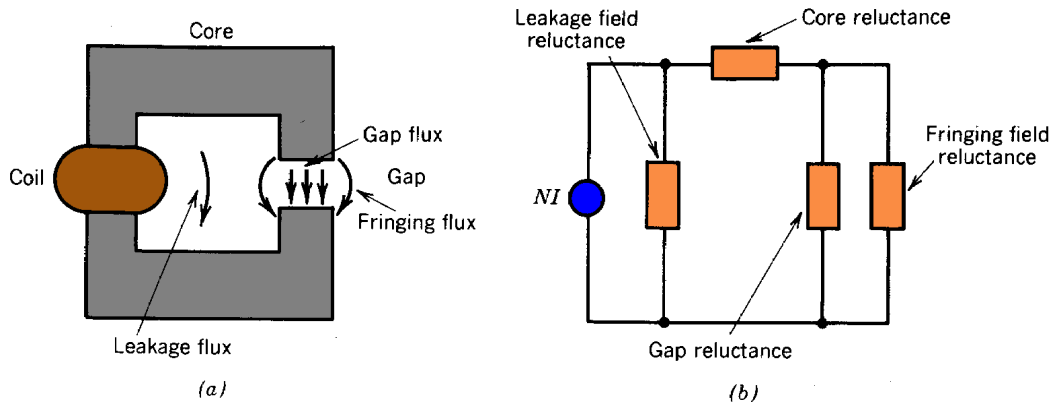
Figure 5.19 Magnet circuit. (*a*) Geometry of spectrometer magnet. (*b*) Equivalent magnetic circuit.

minimized by placing the excitation coils as close to the gap as possible.

   A first-order estimate of driving coil parameters can be derived by neglecting the leakage and fringing contributions and assuming that the circuit reluctance resides predominantly in the gap. In this case it is sufficient to use Eq. (5.23), so that $NI \simeq B_g g / \mu_o$. For example, production of a field of 1 T in a gap with a 0.02 in spacing requires 16-kA turns (160 turns of wire if a 100-A supply is available). For a given supply and excitation coil winding, the field magnitude is inversely proportional to the spacing of the magnet poles.

5.8 PERMANENT MAGNET CIRCUITS

Permanent magnet circuits have the advantage that a dc magnetic field can be maintained with no power input. There are two drawbacks of permanent magnet circuits: (1) it is difficult to vary the field magnitude in the gap and (2) bulky magnets are needed to supply high fields over large areas. The latter problem has been alleviated by the development of rare-earth samarium cobalt magnets which have a maximum energy product three times that of conventional Alnico alloys. In other words, the same field configuration can be produced with a magnet of one-third the volume. Permanent magnet quadrupole lenses (Section 6.10) are an interesting option for focusing in accelerators (See K. Halbach, *Physical and Optical Properties of Rare Earth Cobalt Magnets*, Nucl. Instrum. Methods **187**, 109 (1981). In this section, we shall review some of the properties of permanent magnetic materials and first-order principles for designing magnetic circuits.

103
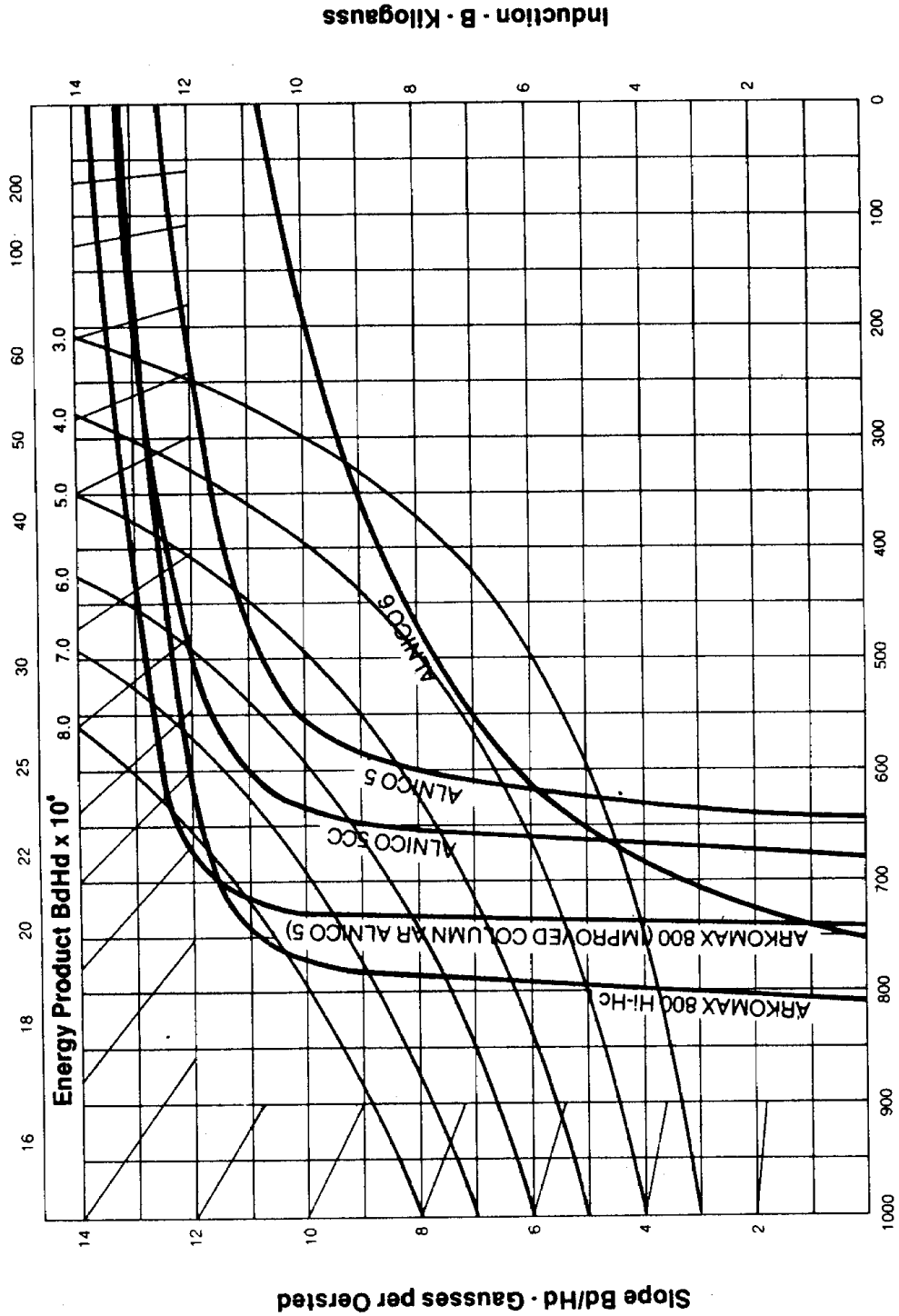
Figure 5.20 Demagnetization curve for some common permanent magnet materials. (Used by permission of Arnold Engineering Company.)

The second quadrant of a hysteresis curve for some common permanent magnet materials is shown in Figure 5.20. The plot is usually called the *demagnetization curve*. The most striking difference between Figure 5.20 and the hysteresis curve for soft iron (Fig. 5.13) is that the coercive force is about 100 times larger for the permanent magnets. In other words, it takes considerably more energy to align the domains and to demagnetize the material. Generation of magnetic fields in vacuum requires energy; a permanent magnet can produce fields because of the stored energy received during magnetization.

Figure 5.20 can be used to calculate the field produced in the gap of a magnetic circuit. The method used to find the operating point on the demagnetization curve is illustrated in Figure 5.21. In the first part of the figure, the permanent magnet is included in a zero reluctance circuit

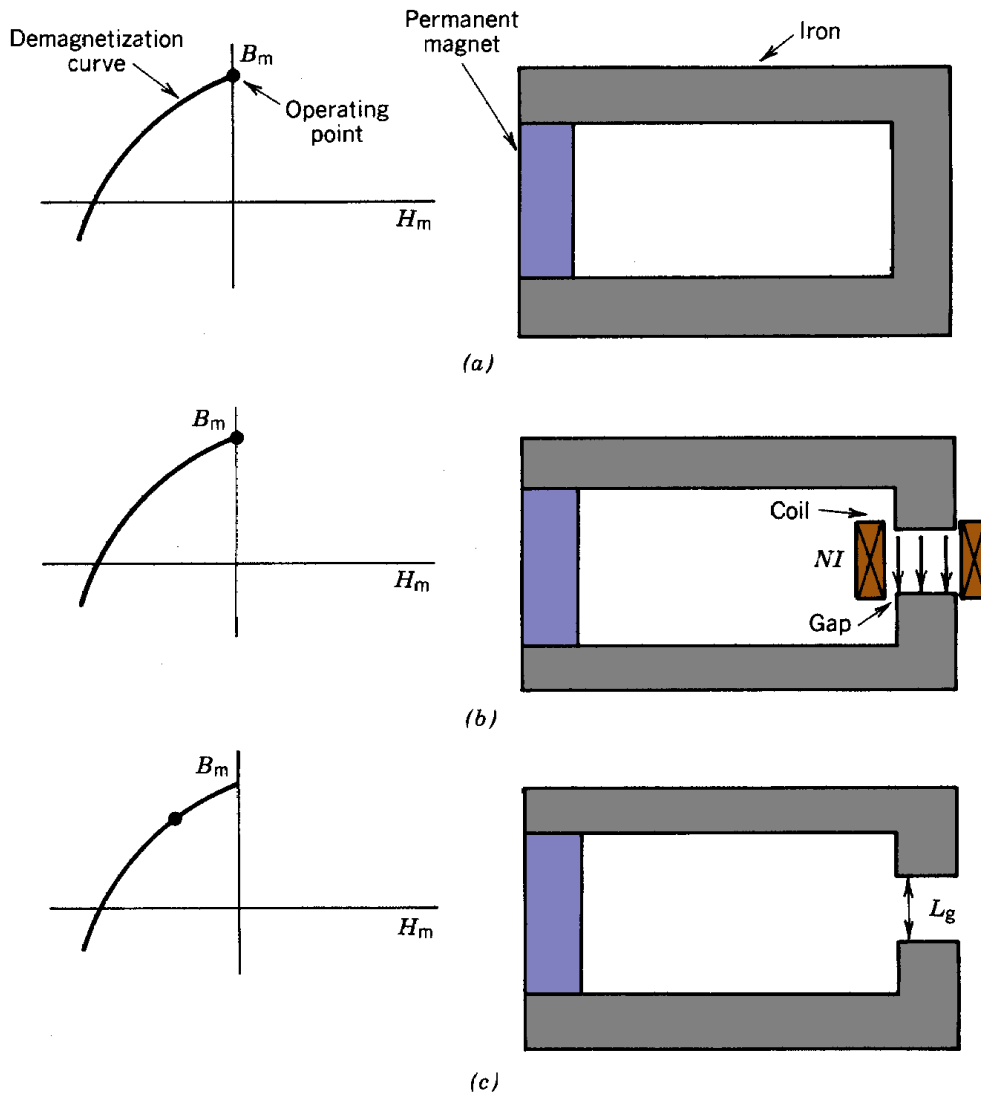
Figure 5.21 Operating point of a permanent magnet. (*a*) Permanent magnet with a continuous iron flux conductor, zero magnetizing force. (*b*) Addition of an air gap with a coil to supply field energy. (*c*) Deactivation of the gap coil.

105

containing an ideal iron core ($H_s = 0$) with no gap. There is no free current. The circuital integral of H is zero, so that H_m (the magnetic intensity in the permanent magnet) is zero. The magnetic field in the loop is equal to B_m, the remanence field of the permanent magnet. Next, assume that an air gap is introduced into the circuit, but excitation windings are placed around the gap with the proper current to produce a field equal to B_m (Fig. 5.21b). The current in the windings is in the same direction as the atomic currents in the ferromagnetic materials. Because the energy for the vacuum fields is supplied by an external source, the circuit still appears to have zero reluctance. The operating point of the permanent magnet remains at $H_m = 0$, $B_m = B_{rm}$.

In the final state (Fig. 5.21c), the current in the excitation coils drops to zero. This is equivalent to the addition of a negative current to the existing current. The negative current demagnetizes the permanent magnet, or moves the operating point in Figure 5.20 to the left. Thus, an air gap in a permanent magnet circuit acts like an excitation winding with a current opposed to the atomic currents. There is no net applied current in the circuit of Figure 5.21c so that $\int \boldsymbol{H} \cdot \boldsymbol{dl} = 0$. Neglecting the reluctance of the iron core, the operating point of the permanent magnet is determined by the gap properties through

$$H_m L_m \ = \ H_g L_g \ = \ B_g L_g / \mu_o. \tag{5.27}$$

where L_m is the length of the permanent magnet.

An important parameter characterizing the performance of a permanent magnet in a circuit is the energy product.

Energy Product. The product of magnet field times magnetic intensity at the operating point of a permanent magnet, or $H_m B_m$.

Equation (5.27) can be used to demonstrate the significance of the energy product. We again take the example of a simple circuit with a magnet, zero reluctance core, and air gap. Continuity of flux implies that $B_g A_g = B_m A_m$, where A_g and A_m are the cross-sectional areas of the gap and magnet respectively. This condition, combined with Eq. (5.27), yields

$$(B_g^2 / 2\mu_o) \ (A_g L_g) \ = \ (H_m B_m / 2) \ (A_m L_m). \tag{5.28}$$

The first factor on the left is the magnetic field energy density in the gap, and the second term is the gap volume. On the right, the first factor is one-half the energy product and the second factor is the magnet volume. Thus, the magnet volume and the energy product determine the magnetic field energy in the gap.

Energy product is given in joules per cubic meter (mks units) or in megagauss oersteds (MG-Oe) in CGS units. The conversion is I MG-Oe = 7940 J/m³. Hyperbolic lines of constant $B_m H_m$ are plotted in Figure 5.20. This is a graphic aid to help determine the energy product at different points of the demagnetization curve. A goal in designing a permanent magnet circuit is to produce the required gap field with the minimum volume magnet. This occurs at the point on the

demagnetization curve where $B_m H_m$ is maximum. In Figure 5.20, parameters of the circuit should be chosen so that H_m is about 550 Oe.

Two examples will serve to illustrate methods of choosing permanent magnets. Both involve first-order design of a simple circuit with no leakage or fringing flux; the second-order design must invoke field calculations, tabulated gap properties or modeling experiments for an accurate prediction. To begin, suppose that we constrain the gap parameters ($B_g = 8$ kG, $A_g = 10$ cm^2 and $L_g = 1$ cm and the type of magnetic material (Alnico 5). We must now determine the dimensions of the magnet that will produce the gap field. Using Eq. (5.27) with $H_g = 8$ kOe and $H_m = 600$ Oe, the length of the magnet must be 13.3 cm. The magnetic field is $B_m = 8$ kG, so that the minimum magnet cross-sectional is 10 cm^2.

In the second example, assume that the dimensions of the gap and magnet are constrained by the application. The goal is to determine what magnetic material will produce the highest gap flux and the value of this flux. For the simple circuit, the condition of constant flux can be combined with Eq. (5.27) to give

$$H_g L_g / B_g A_g \;=\; H_m L_m / B_m A_m \;=\; L_g / \mu_o A_g.$$

The expression on the right-hand side is the reluctance of the gap, R_g. We can then write

$$B_m / H_m \;=\; L_m / R_g A_m. \tag{5.29}$$

With the stated conditions, the quantity $B_m H_m$ must have a constant ratio. This motivates the definition of the permanence coefficient.

Permanence Coefficient, or Load Line. Equal to (B_m/H_m). The permanence coefficient is a function only of the geometries of the magnetic load (system reluctance) and the magnet.

Fiducial points are usually included in demagnetization curves to lay out load lines. Given the load line, operating points on various permanent magnet materials can be determined. The highest gap flux will be produced by the material with the highest energy product at the intersection. The gap flux can then be determined from the magnet operating point.

6

Electric and Magnetic Field Lenses

The subject of charged particle optics is introduced in this chapter. The concern is the control of the transverse motion of particles by shaped electric and magnetic fields. These fields bend charged particle orbits in a manner analogous to the bending of light rays by shaped glass lenses. Similar equations can be used to describe both processes. Charged particle lenses have extensive applications in such areas as electron microscopy, cathode ray tubes, and accelerator transport.

   In many practical cases, beam particles have small velocity perpendicular to the main direction of motion. Also, it is often permissible to use special forms for the electric and magnetic fields near the beam axis. With these approximations, the transverse forces acting on particles are linear; they increase proportional to distance from the axis. The treatment in this chapter assumes such forces. This area is called *linear* or *Gaussian* charged particle optics.

   Sections 6.2 and 6.3 derive electric and magnetic field expressions close to the axis and prove that any region of linear transverse forces acts as a lens. Quantities that characterize thick lenses are reviewed in Section 6.4 along with the equations that describe image formation. The bulk of the chapter treats a variety of static electric and magnetic field focusing devices that are commonly used for accelerator applications.

6.1 TRANSVERSE BEAM CONTROL

Particles in beams always have components of velocity perpendicular to the main direction of motion. These components can arise in the injector; charged particle sources usually operate at high temperature so that extracted particles have random thermal motions. In addition, the fields in injectors may have imperfections of shape. After extraction, space charge repulsion can accelerate particles away from the axis. These effects contribute to expansion of the beam. Accelerators and transport systems have limited transverse dimensions. Forces must be applied to deflect particles back to the axis. In this chapter, the problem of confining beams about the axis will be treated. When accelerating fields have a time dependence, it is also necessary to consider longitudinal confinement of particles to regions along the axis. This problem win be treated in Chapter 13.

Charged particle lenses perform three types of operations. One purpose of lenses is to *confine* a beam, or maintain a constant or slowly varying radius (see Fig. 6.1a). This is important in high-energy accelerators where particles must travel long distances through a small bore. Velocity spreads and space-charge repulsion act to increase the beam radius. Expansion can be countered
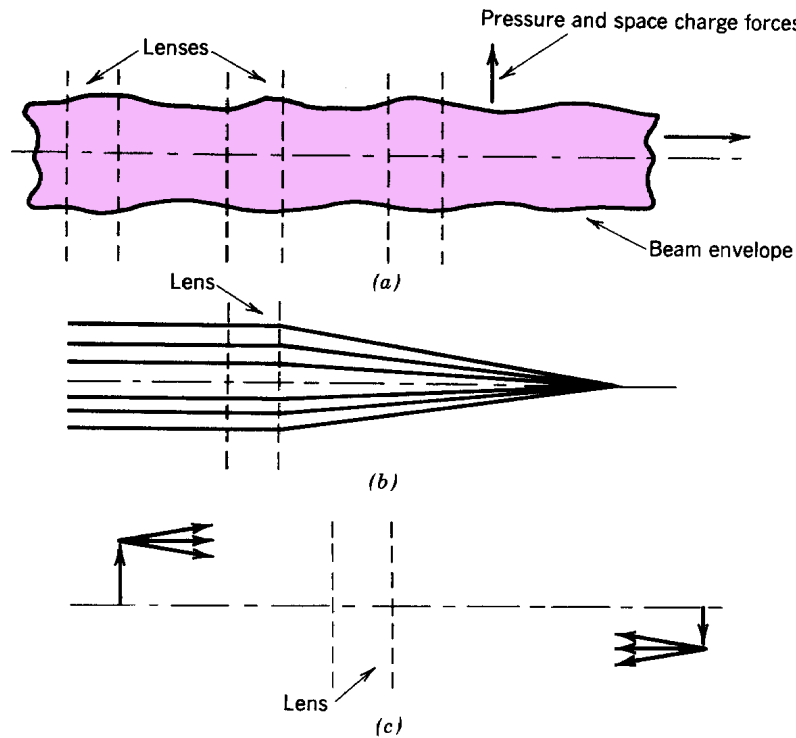

Figure 6.1 Functions of charged particle lenses. (*a*) Beam confinement. (*b*) Focusing to a spot. (*c*) Imaging.

109

by continuous confining forces which balance the outward forces or through a periodic array of lenses which deflect the particles toward the axis. In the latter case, the beam outer radius (or envelope) oscillates about a constant value.

A second function of lenses is to *focus* beams or compress them to the smallest possible radius (Fig. 6.1b). If the particles are initially parallel to the axis, a linear field lens aims them at a common point. Focusing leads to high particle flux or a highly localized beam spot. Focusing is important for applications such as scanning electron microscopy, ion microprobes, and ion-beam-induced inertial fusion.

A third use of charged particle lenses is forming an *image*. (Fig. 6.1c). When there is a spatial distribution of beam intensity in a plane, a lens can make a modified copy of the distribution in another plane along the direction of propagation. An image is formed if all particles that leave a point in one plane are mapped into another, regardless of their direction. An example of charged particle image formation is an image intensifier. The initial plane is a photo-cathode, where electrons are produced proportional to a light image. The electrons are accelerated and deflected by an electrostatic lens. The energetic electrons produce an enhanced copy of the light image when they strike a phosphor screen.

The terminology for these processes is not rigid. Transverse confinement is often referred to as focusing. An array of lenses that preserves the beam envelope may be called a focusing channel. The processes are, in a sense, interchangeable. Any linear field lens can perform all three functions.

6.2 PARAXIAL APPROXIMATION FOR ELECTRIC AND MAGNETIC FIELDS

Many particle beam applications require cylindrical beams. The electric and magnetic fields of lenses for cylindrical beams are azimuthally symmetric. In this section, analytic expressions are derived expressions for such fields in the paraxial approximation. The term *paraxial* comes from the Greek *para* meaning "alongside of." Electric and magnetic fields are calculated at small radii with the assumption that the field vectors make small angles with the axis. The basis for the approximation is illustrated for a magnetic field in Figure 6.2. The currents that produce the field are outside the beam and vary slowly in z over scale lengths comparable to the beam radius.

Cylindrical symmetry allows only components B_r and B_z for static magnetic fields. Longitudinal currents at small radius are required to produce an azimuthal field B_θ. The assumptions of this section exclude both particle currents and displacement currents. Similarly, only the electric field components E_r and E_z are included. In the paraxial approximation, **B** and **E** make small angles with the axis so that $E_r \ll E_z$ and $B_r \ll B_z$.
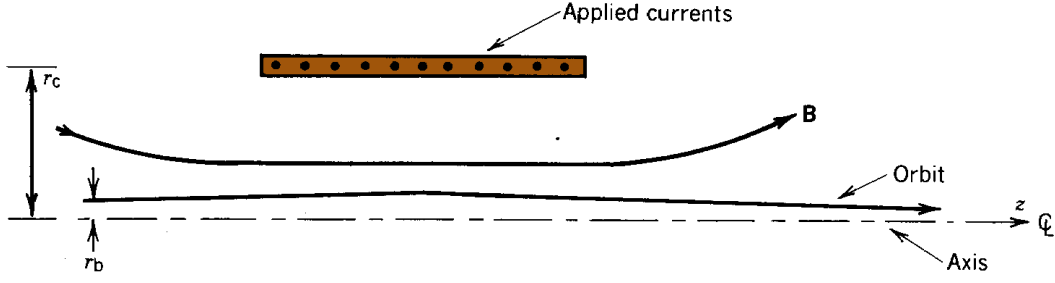
Electric and Magnetic Field Lenses

Figure 6.2 Validity conditions for the paraxial field approximation in a magnetic field lens. Paraxial approximation: $r_b \ll r_c$; $v_r \ll v_z$; $B_r \ll B_z$.

The following form for electrostatic potential is useful to derive approximations for paraxial electric fields:

$$\varphi(r,z) = \varphi(0,z) + Ar \, (\partial\varphi/\partial z)|_o + Br^2 \, (\partial^2\varphi/\partial z^2)|_o$$

$$+ Cr^3 \, (\partial^3\varphi/\partial z^3)|_o + Dr^4 \, (\partial^4\varphi/\partial z^4)|_o + ...$$

(6.1)

The z derivatives of potential are evaluated on the axis. Note that Eq. (6.1) is an assumed form, not a Taylor expansion. The form is valid if there is a choice of the coefficients *A, B, C,...*, such that $\varphi(r, z)$ satisfies the Laplace equation in the paraxial approximation. The magnitude of terms decreases with increasing power of r. A term of order *n* has the magnitude $\varphi_o(\Delta r/\Delta z)^n$, where Δr and Δz are the radial and axial scale lengths over which the potential varies significantly. In the paraxial approximation, the quantity $\Delta r/\Delta z$ is small.

   The electric field must go to zero at the axis since there is no included charge. This implies that *A = 0* in Eq. (6.1). Substituting Eq. (6.1) into (4.19), we find that the coefficients of all odd powers of *r* must be zero. The coefficients of the even power terms are related by

$$4B \, (\partial^2\varphi/\partial z^2) + 16D \, r^2 \, (\partial^4\varphi/\partial z^4)$$

$$+ ... + (\partial^2\varphi/\partial z^2) + B \, r^2 \, (\partial^4\varphi/\partial z^4) + ... = 0.$$

(6.2)

This is consistent if *B = - 1/4* and *D = - B/16 = 1/64*. To second order in $\Delta r/\Delta z$, $\varphi(r, z)$ can be expressed in terms of derivatives evaluated on axis by

$$\varphi(r,z) \cong \varphi(0,z) - (r^2/4) \, (\partial^2\varphi/\partial z^2)|_o.$$

(6.3)

The axial and radial fields are

$$E(0,z) \cong -(\partial\varphi/\partial z)|_o, \quad E_r(r,z) \cong (r/2) \, (\partial^2\varphi/\partial z^2)|_o.$$

(6.4)

111

This gives the useful result that the radial electric field can be expressed as the derivative of the longitudinal field on axis:

$$E_r(r,z) \cong -(r/2) \; [\partial E_z(0,z)/\partial z].$$ (6.5)

Equation (6.5) will be applied in deriving the paraxial orbit equation (Chapter 7). This equation makes it possible to determine charged particle trajectories in cylindrically symmetric fields in terms of field quantities evaluated on the axis. A major implication of Eq. (6.5) is that all transverse forces are linear in the paraxial approximation. Finally, Eq. (6.5) can be used to determine the radial variation of E_z. Combining Eq. (6.5) with the azimuthal curl equation ($\partial E_z/\partial r - \partial E_r/\partial z = 0$) gives

$$E_z(r,z) \cong E_z(0,z) - (r^2/4) \; [\partial^2 E_z(0,z)/\partial z^2].$$ (6.6)

The variation of E_z is second order with radius. In the paraxial approximation, the longitudinal field and electrostatic potential are taken as constant in a plane perpendicular to the axis. A parallel treatment using the magnetic potential shows that

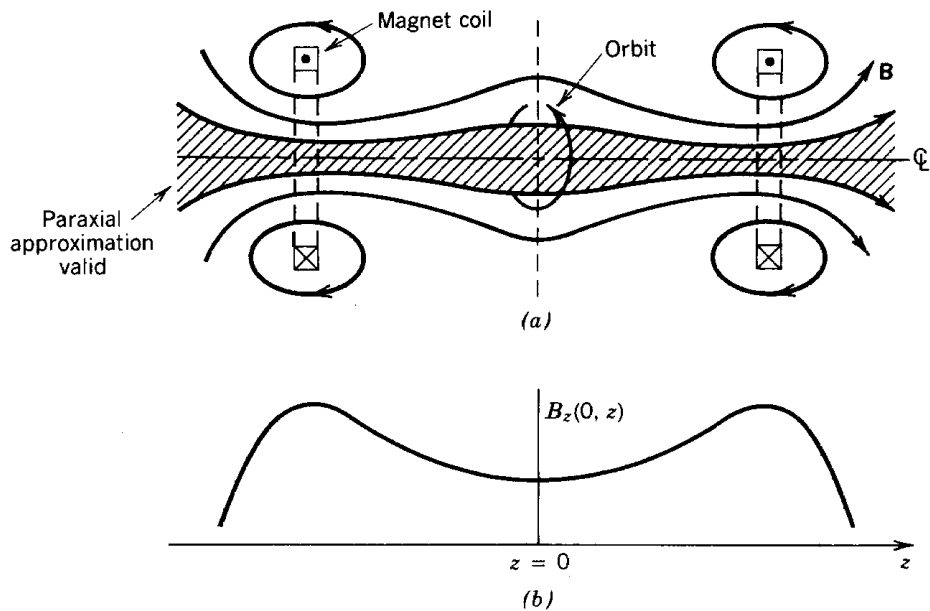$$B_r(r,z) \cong -(r/2) \; [\partial B_z(0,z)/\partial z].$$ (6.7)

Figure 6.3 Magnetic mirror field. (*a*) Geometry, field components, and forces on a particle with an axi-centered orbit. (*b*) Variation of axial field on-axis, $B_z(0, z)$.

Figure 6.3 is an example of a paraxial magnetic field distribution. The fields are produced by two axicentered circular coils with currents in the same direction. In plasma research, the field distribution is called a *magnetic mirror*. It is related to the fields used in cyclotrons and betatrons. The magnitude of $B_z(0, z)$ is maximum at the coils. The derivative of B_z is positive for $z > 0$ and negative for $z < 0$. Consider a positively charged particle with an axicentered circular orbit that has a positive azimuthal velocity. If the particle is not midway between the coils, there will be an axial force $qv_\theta B_r$. Equation (6.7) implies that this force is in the negative z direction for $z > 0$ and the converse when $z < 0$. A magnetic mirror can provide radial and axial confinement of rotating charged particles. An equivalent form of Eq. (6.6) holds for magnetic fields. Because $\partial B_z^2/\partial z^2$ is positive in the mirror, the magnitude of B_z decreases with radius.

6.3 FOCUSING PROPERTIES OF LINEAR FIELDS

In this section, we shall derive the fact that all transverse forces that vary linearly away from an axis can focus a parallel beam of particles to a common point on the axis. The parallel beam, shown in Figure 6.4, is a special case of *laminar* motion. Laminar flow (from *lamina*, or layer) implies that particle orbits at different radii follow streamlines and do not cross. The ideal laminar beam has no spread of transverse velocities. Such beams cannot be produced, but in many cases laminar motion is a valid first approximation. The derivation in this section also shows that linear forces preserve laminar flow.

   The radial force on particles is taken as $F_r(r) = -A(z,v_r)\, r$. Section 6.2 showed that paraxial electric forces obey this equation. It is not evident that magnetic forces are linear with radius since particles can gain azimuthal velocity passing through radial magnetic fields. The proof that the
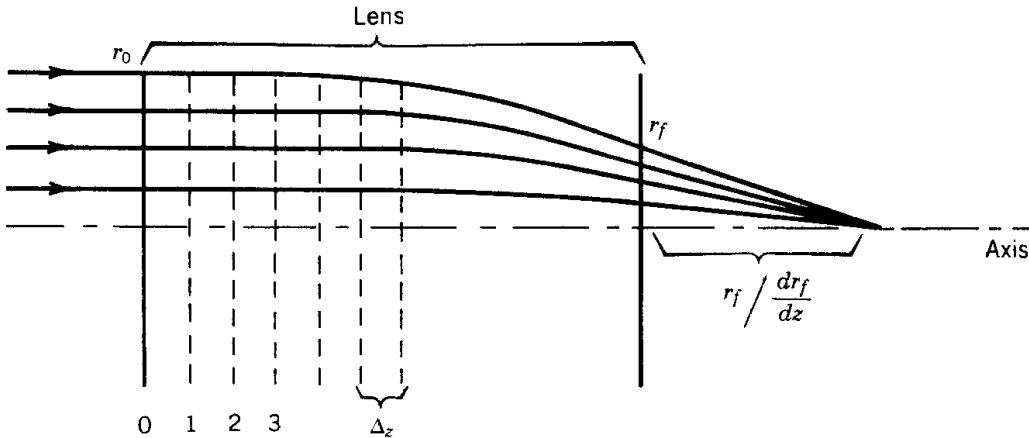

Figure 6.4 Finite difference calculation of the effect of linear focusing fields on particle orbits.

combination of magnetic and centrifugal forces gives a linear radial force variation is deferred to Section 6.7.

Particle orbits are assumed paraxial; they make small angles with the axis. This means that $v_r \ll v_z$. The total velocity of a particle is $v_o^2 = v_r^2 + v_z^2$. If v_o is constant, changes of axial velocity are related to changes of radial velocity by

$$\Delta v_z / v_z \cong -(v_r / v_z) \, (\Delta v_r / v_z).$$

Relative changes of axial velocity are proportional to the product of two small quantities in the paraxial approximation. Therefore, the quantity v_z is almost constant in planes normal to z. The average axial velocity may vary with z because of acceleration in E_z fields. If v_z is independent of r, time derivatives can be converted to spatial derivatives according to

$$d/dt \Rightarrow v_z \, (d/dz). \tag{6.8}$$

The interpretation of Eq. (6.8) is that the transverse impulse on a particle in a time Δt is the same as that received passing through a length element $\Delta z = v_z \Delta t$. This replacement gives differential equations expressing radius as a function of z rather than t. In treatments of steady-state beams, the orbits $r(z)$ are usually of more interest than the instantaneous position of any particle.

Consider, for example, the nonrelativistic transverse equation of motion for a particle moving in a plane passing through the axis in the presence of azimuthally symmetric radial forces

$$d^2 r / dt^2 = F_r(r,z,v_z)/m_o.$$

Converting time derivatives to axial derivatives according to Eq. 6.8 yields

$$d(v_z r')/dt = v_z r' v_z' + v_z^2 r'' = F_r/m_o,$$

or

$$dr'/dz = F_r(r,z,v_z)/m_o v_z^2 - v_z' r'/v_z, \qquad r' = dr/dz. \tag{6.9}$$

A primed quantity denotes an axial derivative. The quantity r' is the angle between the particle orbit and the axis. The motion of a charged particle through a lens can be determined by a numerical solution of Eqs. (6.9). Assume that the particle has $r = r_o$ and $r' = 0$ at the lens entrance. Calculation of the final position, r_f and angle, r_f' determines the focal properties of the fields. Further, assume that F_r is linear and that $v_z(0, z)$ is a known function calculated from $E_z(0, z)$. The region over which lens forces extend is divided into a number of elements of length Δz. The following numerical algorithm (the *Eulerian difference method*) can be used to find a

particle orbit.

$$r(z+\Delta z) \; = \; r(z) \; + \; r^{/}(z)\Delta z,$$

$$r^{/}(z+\Delta z) \; = \; r^{/}(z) \; - \; [A(z,v_z)r/m_o v_z^2 \; + \; v_z^{/} r^{//}v_z]\Delta z \qquad (6.10)$$

$$r^{/}(z) \; - \; [a_1(z)r \; + \; a_2(z)r^{/}] \; \Delta z.$$

More accurate difference methods will be discussed in Section 7.8.

Applying Eq. (6.10), position and velocity at the first three positions in the lens are

$$r_o \; = \; r_o, \quad r_o^{/} \; = \; 0,$$

$$r_1 \; = \; r_o, \quad r_1^{/} \; = \; -a_1(0)r_o\Delta z,$$

$$r_2 \; = \; r_o - a_1(0)r_o, \qquad (6.11)$$

$$r_2^{/} \; = \; -a_1(0)r_o\Delta z \; - \; a_1(\Delta z)r_o\Delta z \; + \; a_2(\Delta z)a_1(0)r_o\Delta z.$$

Note that the quantity r_o appears in all terms; therefore,, the position and angle are proportional to r_o at the three axial locations. By induction, this conclusion holds for the final position and angle, r_f and r_f'. Although the final orbit parameters are the sum of a large number of terms (becoming infinite as Δz approaches zero), each term involves a factor of r_o. There are two major results of this observation.

1. The final radius is proportional to the initial radius for all particles. Therefore, orbits do not cross. A linear force preserves laminar motion.
2. The final angle is proportional to r_o; therefore, r_f' is proportional to r_f. In the paraxial limit, the orbits of initially parallel particles exiting the lens form similar triangles. All particles pass through the axis at a point a distance r_f/r_f' from the lens exit (Fig. 6.4).

The conclusion is that any region of static, azimuthally symmetric electric fields acts as a lens in the paraxial approximation. If the radial force has the form $+A(z,v_z)r$, the final radial velocity is positive. In this case, particle orbits form similar triangles that emanate from a point upstream. The lens, in this case, is said to have a *negative focal length*.

6.4 LENS PROPERTIES

The lenses used in light optics can often be approximated as thin lenses. In the thin-lens
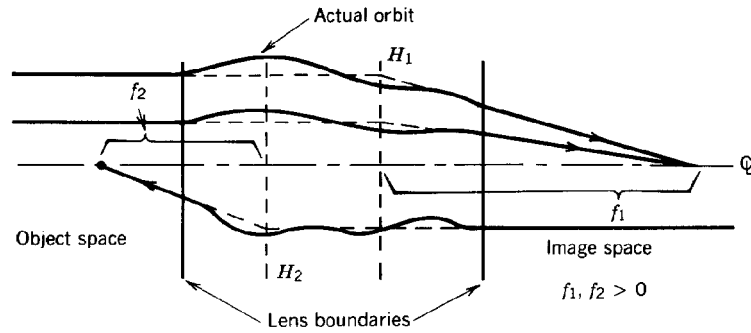
Electric and Magnetic Field Lenses

Figure 6.5 Charged particle lens. Definition of quantities used in linear approximation (Gaussian optics): principal planes (H_1, H_2) and focal lengths (f_1, f_2).

approximation, rays are deflected but have little change in radius passing through the lens. This approximation is often invalid for charged particle optics; the Laplace equation implies that electric and magnetic fields extend axial distances comparable to the diameter of the lens. The particle orbits of Figure 6.4 undergo a significant radius change in the field region. Lenses in which this occurs are called *thick lenses*. This section reviews the parameters and equations describing thick lenses.

   A general charged particle lens is illustrated in Figure 6.5. It is an axial region of electric and magnetic fields that deflects (and may accelerate) particles. Particles drift in *ballistic orbits* (no acceleration) in field-free regions outside the lens. The upstream field-free region is called the *object space* and the downstream region is called the *image space*. Lenses function with particle motion in either direction, so that image and object spaces are interchangeable.

   Orbits of initially parallel particles exiting the lens form similar triangles (Fig. 6.5). If the exit orbits are projected backward in a straight line, they intersect the forward projection of entrance orbits in a plane perpendicular to the axis. This is called the *principal plane*. The location of the principal plane is denoted H_1. The distance from H_1 to the point where orbits intersect is called the *focal length*, f_1. When H_1 and f_1 are known, the exit orbit of any particle that enters the lens parallel to the axis can be specified. The exit orbit is the straight line connecting the focal point to the intersection of the initial orbit with the principal plane. This construction also holds for negative focal lengths, as shown in Figure 6.6.

   There is also a principal plane (H_2) and focal length (f_2) for particles with negative v_z. The focal lengths need not be equal. This is often the case with electrostatic lenses where the direction determines if particles are accelerated or decelerated. Two examples of $f_1 \neq f_2$ are the aperture lens (Section 6.5) and the immersion lens (Section 6.6). A *thin lens* is defined as one where the axial length is small compared to the focal length. Since the principal planes are contained in the field region, $H_1 = H_2$. A thin lens has only one principal plane. Particles emerge at the same radius they entered but with a change in direction.
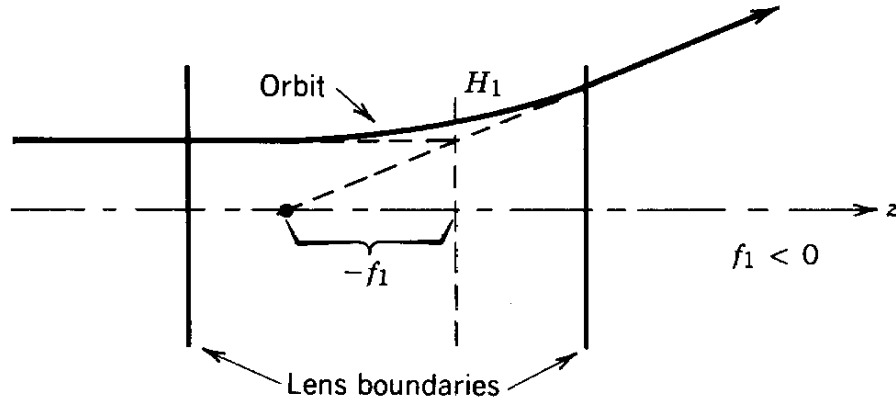
116

Figure 6.6 Construction of a particle orbit in a lens with a negative focal length.

There are two other common terms applied to lenses, the lens power and the *f-number*. The strength of a lens is determined by how much it bends orbits. Shorter focal lengths mean stronger lenses. The lens power P is the inverse of the focal length, $P = 1/f$. If the focal length is measured in meters, the power is given in m^{-1} or *diopters*. The *f*-number is the ratio of focal length to the lens diameter: *f*-number $= f/D$. The *f*-number is important for describing focusing of nonlaminar beams. It characterizes different optical systems in terms of the minimum focal spot size and maximum achievable particle flux.

If the principal planes and focal lengths of a lens are known, the transformation of an orbit between the lenses entrance and exit can be determined. This holds even for nonparallel entrance orbits. The conclusion follows from the fact that particle orbits are described by a linear, second-order differential equation. The relationship between initial and final orbits (r_1, $r_1' \Rightarrow r_f$, r_f') can be expressed as two algebraic equations with four constant coefficients. Given the two initial conditions and the coefficients (equivalent to the two principal planes and focal lengths), the final orbit is determined. This statement will be proved in Chapter 8 using the ray transfer matrix formalism.

Chapter 8 also contains a proof that a linear lens can produce an image. The definition of an image is indicated in Figure 6.7. Two special planes are defined on either side of the lens: the *object plane* and the *image plane* (which depends on the lens properties and the location of the object). An image is produced if all particles that leave a point in the object plane meet at a point in the image plane, independent of their initial direction. There is a mapping of spatial points from one plane to another. The image space and object space are interchangeable, depending on the direction of the particles. The proof of the existence of an image is most easily performed with matrix algebra. Nonetheless, assuming this property, the principal plane construction gives the locations of image and object planes relative to the lens and the magnification passing from one to another.

Figure 6.7 shows image formation by a lens. Orbits in the image and object space are related by the principal plane construction; the exit orbits are determined by the principal plane and focal length. These quantities give no detailed information on orbits inside the lens. The arrows
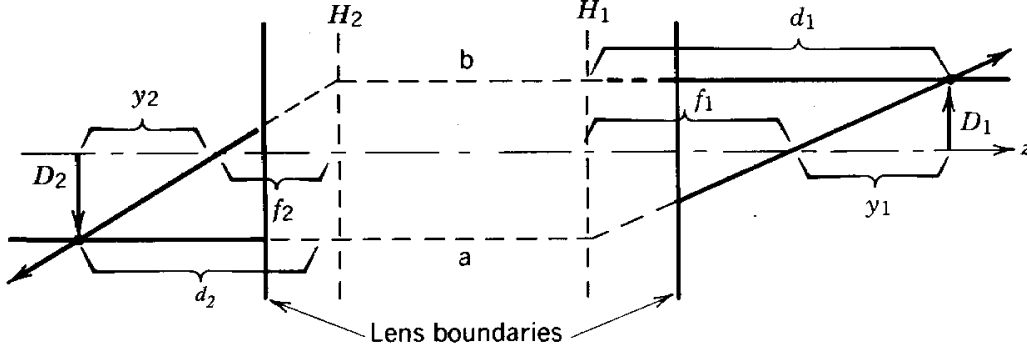
(Actual orbits unspecified in this region)

Figure 6.7   Quantities for calculating the imaging properties of a thick lens.

represent an intensity distribution of particles in the transverse direction. Assume that each point on the source arrow (of length D_2) is mapped to a point in the image plane. The mapping produces an image arrow of length D_1. Parallel orbits are laminar, and the distance from the axis to a point on the image is proportional to its position on the source. We want to find the locations of the image and object planes (d_1 and d_2) relative to the principal planes, as well as the magnification, $M_{21} = D_1/D_2$.

   The image properties can be found by following two particle orbits leaving the object. Their intersection in the image space determines the location of the image plane. The orbit with known properties is the one that enters the lens parallel to the axis. If a parallel particle leaves the tip of the object arrow, it exits the lens following a path that passes through the intersection with the principal plane at $r = D_2$ and the point f_1. This orbit is marked a in Figure 6.7. In order to determine a second orbit, we can interchange the roles of image and object and follow a parallel particle that leaves the right-hand arrow in the $-z$ direction. This orbit, marked b, is determined by the points at H_2 and f_2. A property of particle dynamics under electric and magnetic forces is time reversibility. Particles move backward along the same trajectories if $-t$ is substituted for t. Thus, a particle traveling from the original object to the image plane may also follow orbit b. If the two arrows are in object and image planes, the orbits must connect as shown in Figure 6.7.

   The image magnification for particles traveling from left to right is $M_{21} = D_1/D_2$. For motion in the opposite direction, the magnification is $M_{12} = D_2/D_1$. Therefore,

$$M_{21}\, M_{12}\ =\ 1. \tag{6.12}$$

Referring to Figure 6.7, the following equations follow from similar triangles:

$$D_1/y_1\ =\ D_2/f_1, \quad D_1/f_2\ =\ D_2/y_2. \tag{6.13}$$

These are combined to give $f_1f_2 = y_1y_2$. This equation can be rewritten in terms of the distances d_1 and d_2 from the principal planes as $f_1f_2 = (d_2 - f_2)(d_1 - f_1)$. The result is the thick-lens equation

$$f_1/d_1 \ + \ f_2/d_2 \ = \ 1. \tag{6.14}$$

In light optics, the focal length of a simple lens does not depend on direction. In charged particle optics, this holds for magnetic lenses or *unipotential* electrostatic lenses where the particle energy does not change in the lens. In this case, Eq. (6.14) can be written in the familiar form

$$1/d_1 \ + \ 1/d_2 \ = \ 1/f, \tag{6.15}$$

where $f_1 = f_2 = f$.

In summary, the following procedure is followed to characterize a linear lens. Measured data or analytic expressions for the fields of the lens are used to calculate two special particle orbits. The orbits enter the lens parallel to the axis from opposite axial directions. The orbit calculations are performed analytically or numerically. They yield the principal planes and focal lengths. Alternately, if the fields are unknown, lens properties may be determined experimentally. Parallel particle beams are directed into the lens from opposite directions to determine the lens parameters. If the lens is linear, all other orbits and the imaging properties are found from two measurements.

In principle, the derivations of this section can be extended to more complex optical systems. The equivalent of Eq. (6.14) could be derived for combinations of lenses. On the other hand, it is much easier to treat optical systems using ray transfer matrices (Chapter 8). Remaining sections of this chapter are devoted to the calculation of optical parameters for a variety of discrete electrostatic and magnetostatic charged particle lenses.

6.5 ELECTROSTATIC APERTURE LENS

The electrostatic aperture lens is an axicentered hole in an electrode separating two regions of axial electric field. The lens is illustrated in Figure 6.8. The fields may be produced by grids with applied voltage relative to the aperture plate. If the upstream and downstream electric fields differ, there will be radial components of electric field near the hole which focus or defocus particles. In Figure 6.8, axial electric fields on both sides of the plate are positive, and the field at the left is stronger. In this case, the radial fields point outward and the focal length is negative for positively charged particles traveling in either direction. With reversed field direction (keeping the same relative field strength) or with stronger field on the right side (keeping the same field polarity), the lens has positive focal length. The transverse impulse on a particle passing through the hole is
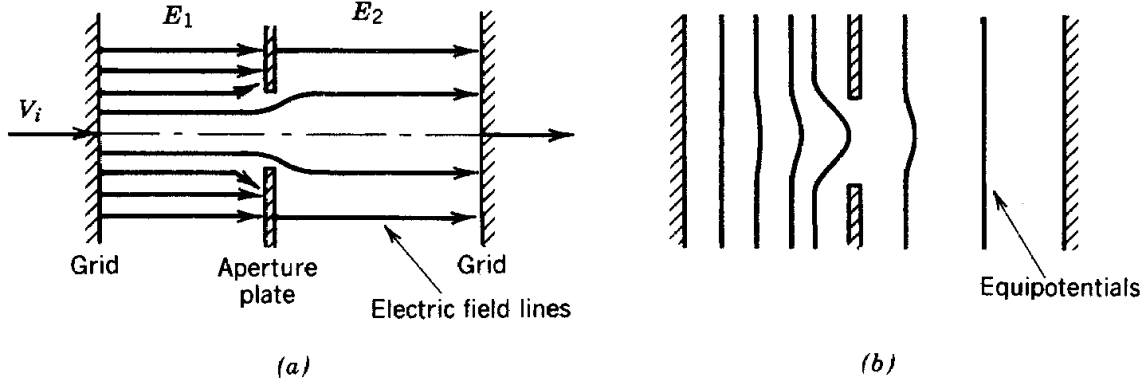
Figure 6.8 Electrostatic aperture lens. (*a*) Geometry, showing electric field lines. (*b*) Equipotential lines.

proportional to the time spent in the radial electric fields. This is inversely proportional to the particle velocity which is determined, in part, by the longitudinal fields. Furthermore, the final axial velocity will depend on the particle direction. These factors contribute to the fact that the focal length of the aperture lens depends on the transit direction of the particle, or $f_1 \neq f_2$.

Radial electric fields are localized at the aperture. Two assumptions allow a simple estimate of the focal length: (1) the relative change in radius passing through the aperture is small (or, the aperture is treated in the thin lens approximation) and (2) the relative change in axial velocity is small in the vicinity of the aperture. Consider a particle moving in the $+z$ direction with $v_r = 0$. The change in v_r for nonrelativistic motion is given by the equation

$$dv_r/dz = qE_r/m_o v_z \cong -(q/2m_o v_z) \; r \; [dE_z(0,z)/dz]. \tag{6.16}$$

In Eq. (6.16), the time derivative was converted to a spatial derivative and E_r was replaced according to Eq. (6.5).

With the assumption of constant r and v_z in the region of nonzero radial field, Eq. (6.16) can be integrated directly to yield

$$v_{rf} / v_{zf} = r_f^{\,/} \cong -qr \; (E_{z2} - E_{z1})/2m_o v_{za} v_{zf}. \tag{6.17}$$

where v_{za} is the particle velocity at the aperture and v_{rf} is the radial velocity after exiting. The quantity v_{zf} is the final axial velocity; it depends on the final location of the particle and the field E_{z2}. The focal length is related to the final radial position (r) and the ratio of the radial velocity to the final axial velocity by $v_{rf}/v_{zf} \approx r/f$. The focal length is
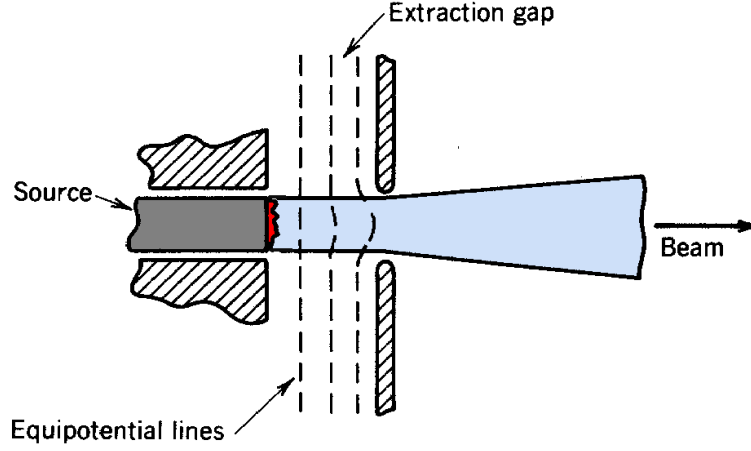
120

Figure 6.9 Extraction gap of an electron gun showing negative-lens effect.

$$f \cong 2m_o v_{za} v_{zf} \, q \ (E_{z2} - E_{z1}).$$

(6.18)

When the particle kinetic energy is large compared to the energy change passing through the lens, $v_{za} \simeq v_{zf}$, and we find the usual approximation for the aperture lens focal length

$$f \cong 2m_o v_{zf}^2 \, / q(E_{z2} - E_{z1}) \; = \; 4T/q(E_{z2} - E_{z1}).$$

(6.19)

The *charged particle extractor* (illustrated in Fig. 6.9) is a frequently encountered application of Eq. (6.19). The extractor gap pulls charged particles from a source and accelerates them. The goal is to form a well-directed low-energy beam. When there is high average beam flux, grids cannot be used at the downstream electrode and the particles must pass through a hole. The hole acts as an aperture lens, with $E_1 > 0$ and $E_2 = 0$. The focal length is negative; the beam emerging will diverge. This is called the *negative lens effect* in extractor design. If a parallel or focused beam is required, a focusing lens can be added downstream or the source can be constructed with a concave shape so that particle orbits converge approaching the aperture.

6.6 ELECTROSTATIC IMMERSION LENS

The geometry of the electrostatic immersion lens is shown in Figure 6.10. It consists of two tubes at different potential separated by a gap. Acceleration gaps between drift tubes of a standing-wave linear accelerator (Chapter 14) have this geometry. The one-dimensional version of this lens occurs in the gap between the Dees of a cyclotron (Chapter 15). Electric field distributions for a cylindrical lens are plotted in Figure 6.10.
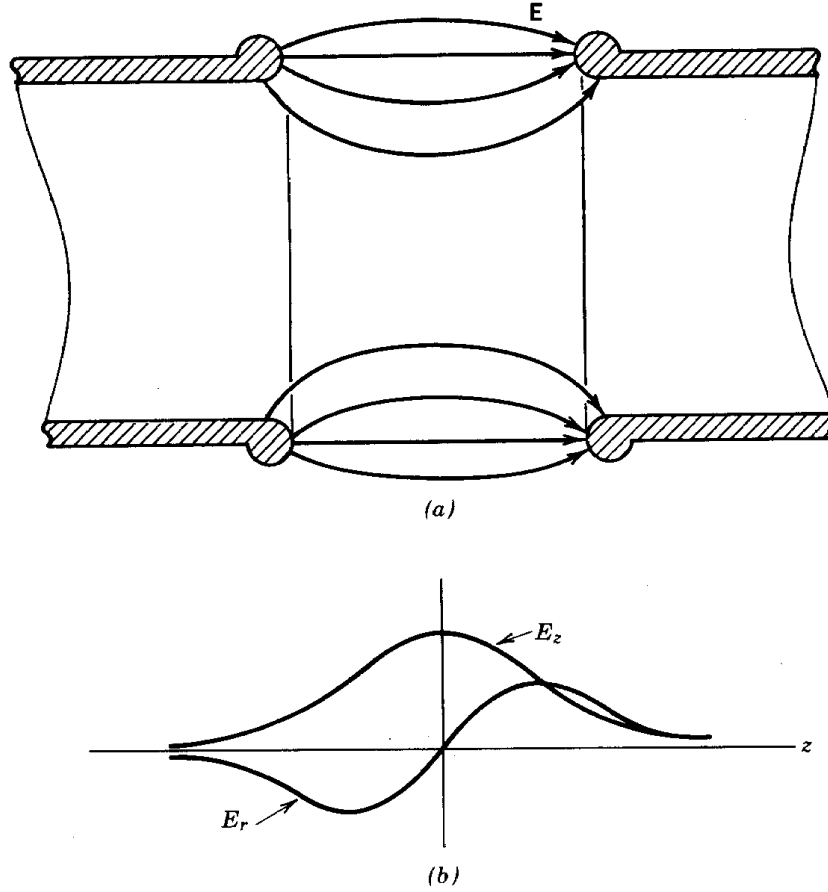
Figure 6.10 Electrostatic immersion lens. (*a*) Geometry and electric field lines. (*b*) Relative variations of longitudinal electric field, $E_z(0, z)$ (on-axis), and transverse field, $E_r(r, z)$ (off-axis), moving through the lens.

Following the treatment used for the aperture lens, the change in radial velocity of a particle passing through the gap is

$$\Delta v_r = v_{rf} = \int dz \; [qE_r(r,z)/m_o v_z]. \tag{6.20}$$

The radial electric field is symmetric. There is no deflection if the particle radius and axial velocity are constant. In contrast to the aperture lens, the focusing action of the immersion lens arises from changes in r and v_z in the gap region. Typical particle orbits are illustrated in Figure 6.11. When the longitudinal gap field accelerates particles, they are deflected inward on the entrance side of the lens and outward on the exit side. The outward impulse is smaller because (1) the particles are closer to the axis and (2) they move faster on the exit side. The converse holds for a deceleratin-gap. Particles are deflected to larger radii on the entrance side and are therefore more strongly influenced by the radial fields on the exit side. Furthermore, v_z is lower at the exit side enhancing
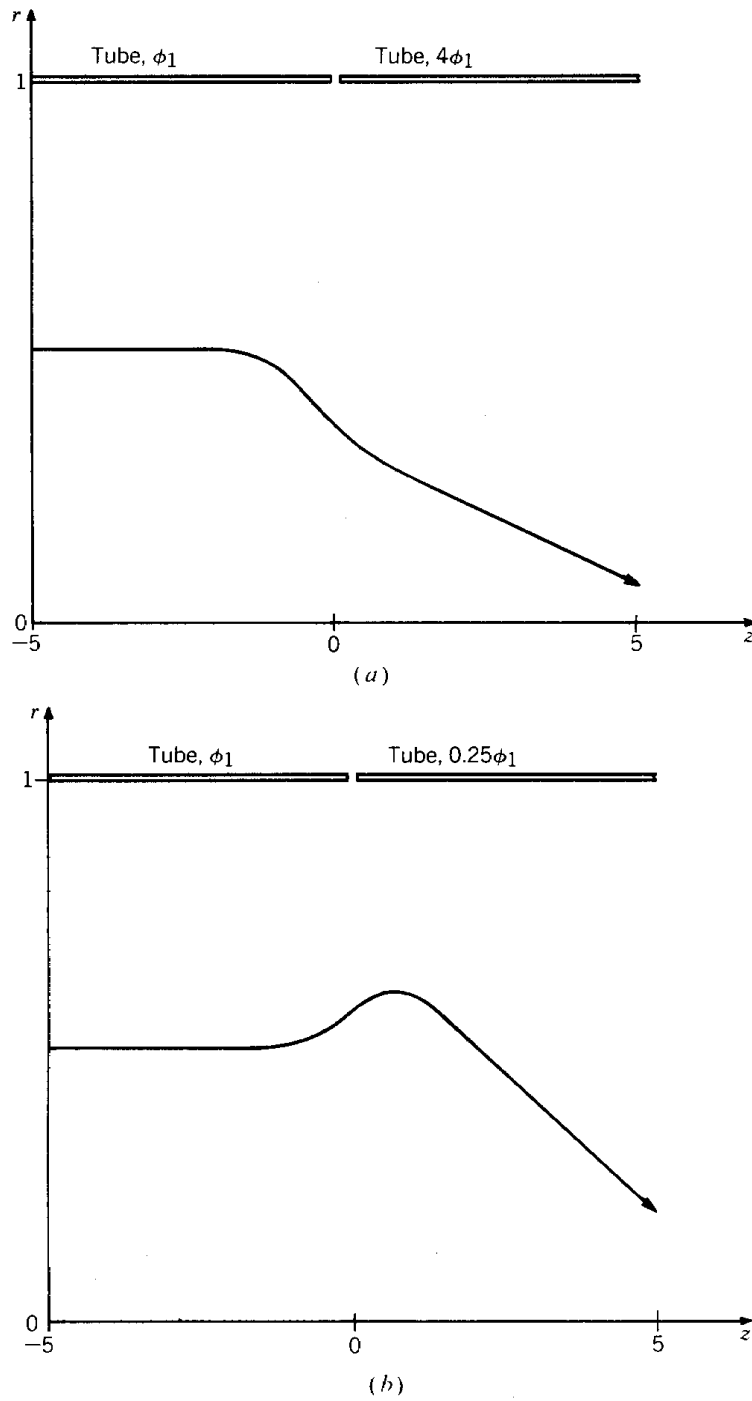
122

Figure 6.11 Particle trajectories in an immersion lens. (a) Accelerating lens (final kinetic energy equals 4 times initial energy). (b) Decelerating lens (final kinetic energy equals 0.25 times initial energy). (Note expanded radial scale).

focusing. The focal length for either polarity or charge sign is positive.

The orbits in the immersion lens are more complex than those in the aperture lens. The focal length must be calculated from analytic or numerical solutions for the electrostatic fields and numerical solutions of particle orbits in the gap. In the paraxial approximation, only two orbits need be found. The results of such calculations are shown in Figure 6.12 for varying tube diameter with a narrow gap. It is convenient to reference the tube potentials to the particle source so that the exit energy is given by $T_f = qV_2$. With this convention, the abscissa is the ratio of exit to entrance kinetic energy. The focal length is short (lens power high) when there is a significant change in kinetic energy passing through the lens. The *einzel lens* is a variant of the immersion lens often encountered in low-energy electron guns. It consists of three colinear tubes, with the middle tube elevated to high potential. The einzel lens consists of two immersion lenses in series; it is a unipotential lens.

An interesting modification of the immersion lens is *foil* or *grid focusing*. This focusing method, illustrated in Figure 6.13, has been used in low-energy linear ion accelerators. A conducting foil or mesh is placed across the downstream tube of an accelerating gap. The resulting field pattern looks like half of that for the immersion lens. Only the inward components of radial field are present. The paraxial approximation no longer applies; the foil geometry has first-order focusing. Net deflections do not depend on changes of r and v_z as in the immersion lens. Consequently, focusing is much stronger. Foil focusing demonstrates one of the advantages gained by locating charges and currents within the beam volume, rather than relying on external electrodes or coils.
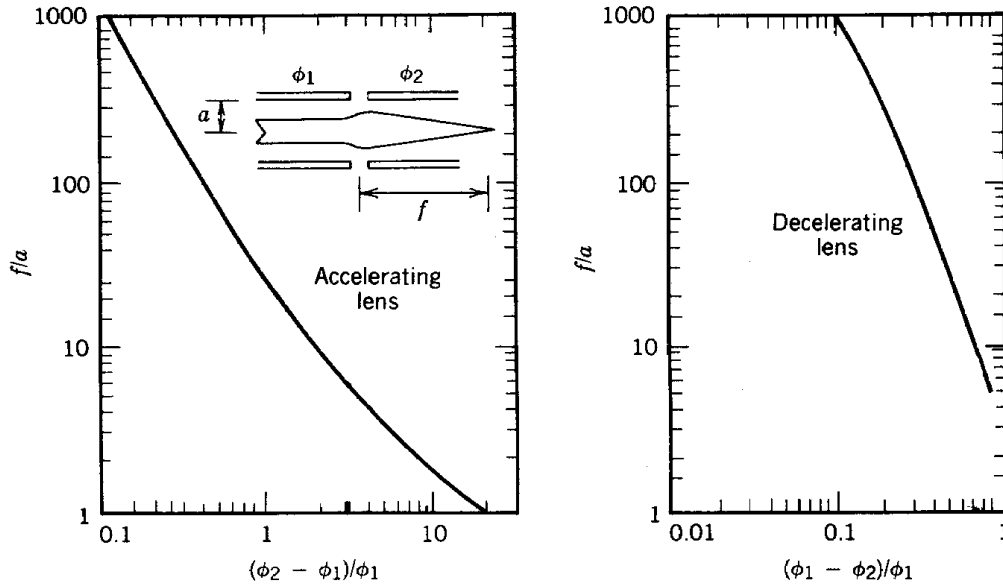

Figure 6.12   Focal lengths of immersion lenses in terms of relative kinetic energy change in lens. (*a*) Accelerating lenses. (*b*) Decelerating lenses.
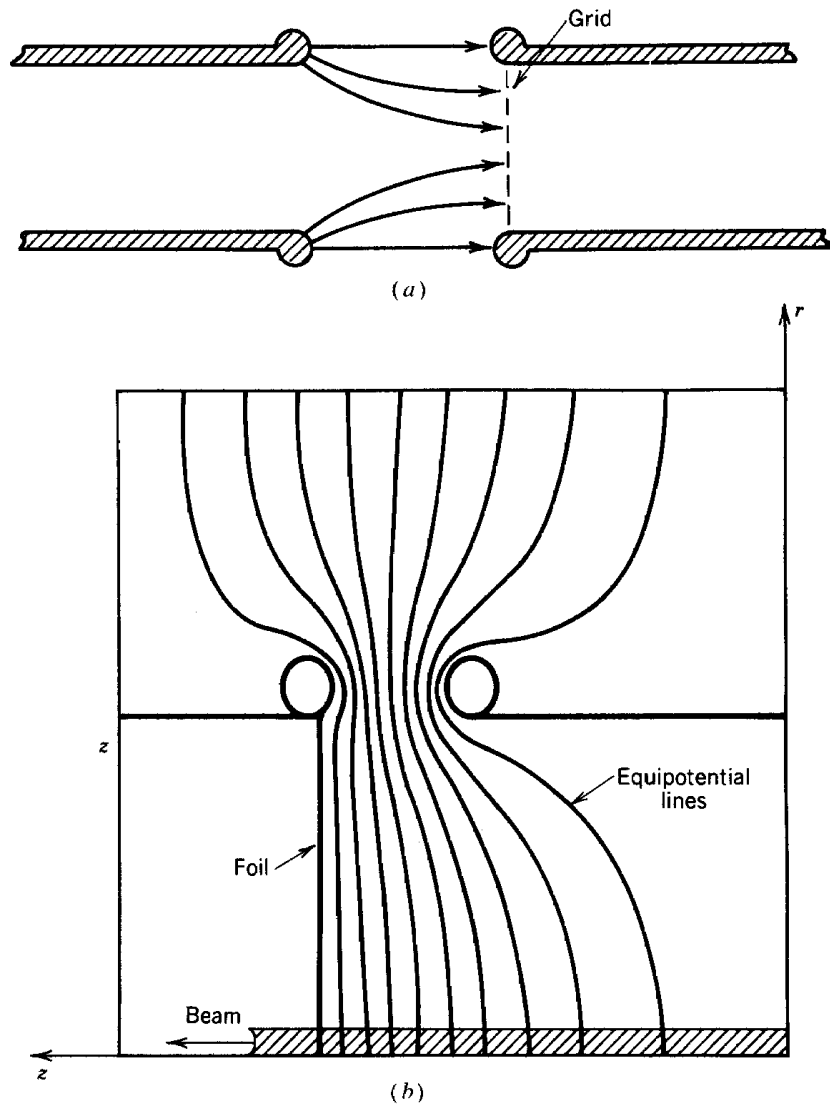
Figure 6.13 Accelerating gap of a drift tube linear accelerator with a grid for enhanced electrostatic focusing. (*a*) Geometry. (*b*) Equipotential lines.

The charges, in this case, are image charges on the foil. An example of internal currents, the toroidal field magnetic sector lens, is discussed in Section 6.8.

6.7 SOLENOIDAL MAGNETIC LENS

The *solenoidal magnetic lens* is illustrated in Figure 6.14. It consists of a region of cylindrically
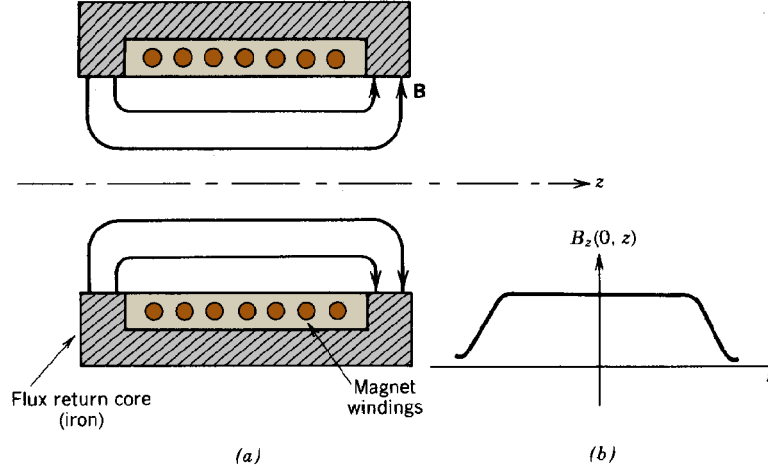
Figure 6.14 Solenoidal magnetic lens. (*a*) Geometry and field lines. (*b*) Variation of longitudinal magnetic field on axis, $B_z(0, z)$.

symmetric radial and axial magnetic fields produced by axicentered coils carrying azimuthal current. This lens is the only possible magnetic lens geometry consistent with cylindrical paraxial beams. It is best suited to electron focusing. It is used extensively in cathode ray tubes, image intensifiers, electron microscopes, and electron accelerators. Since the magnetic field is static, there is no change of particle energy passing through the lens; therefore, it is possible to perform relativistic derivations without complex mathematics.

Particles enter the lens through a region of radial magnetic fields. The Lorentz force ($ev_z \times B_r$) is azimuthal. The resulting v_θ leads to a radial force when crossed into the B_z fields inside the lens. The net effect is a deflection toward the axis, independent of charge state or transit direction. Because there is an azimuthal velocity, radial and axial force equations must be solved with the inclusion of centrifugal and coriolis forces.

The equations of motion (assuming constant γ) are

$$\gamma m_o \, (dv_r/dt) = -qv_\theta B_z + \gamma m_o v_\theta^2/r, \tag{6.21}$$

$$\gamma m_o(dv_\theta/dt) = -qv_z B_z - \gamma m_o v_r v_\theta/r. \tag{6.22}$$

The axial equation of motion is simply that v_z is constant. We assume that r is approximately constant and that the particle orbit has a small net rotation in the lens. With the latter condition, the Coriolis force can be neglected in Eq. (6.22). If the substitution $dv_\theta/dt \cong v_z \, (dv_\theta/dz)$ is made and Eq. (6.7) is used to express B_r in terms of $dB_z(0, z)/dz$, Eq. (6.22) can be integrated to give

$$v_\theta - qrB_z/2\gamma m_o = constant = 0. \tag{6.23}$$

Equation (6.23) is an expression of conservation of canonical angular momentum (see Section

126

7.4). It holds even when the assumptions of this calculation are not valid. Equation (6.23) implies that particles gain no net azimuthal velocity passing completely through the lens. This comes about because they must cross negatively directed radial magnetic field lines at the exit that cancel out the azimuthal velocity gained at the entrance. Recognizing that $d\theta/dt = v_\theta/r$ and assuming that B_z is approximately constant in r, the angular rotation of an orbit passing through the lens is

$$(\theta - \theta_o) = [qB_z(0,z)/2\gamma m_o v_z] \ (z - z_o). \tag{6.24}$$

Rotation is the same for all particles, independent of radius. Substituting Eq. (6.23) and converting the time derivative to a longitudinal derivative, Eq. (6.21) can be integrated to give

$$r_f' = \frac{v_{rf}}{v_z} \cong \frac{-\int dz \ [qB_z(0,z)/\gamma m_o v_z]^2 \ r}{4} \ . \tag{6.25}$$

The focal length for a solenoidal magnetic lens is

$$f = \frac{-r_f}{r_f'} = \frac{4}{\int dz \ [qB_z(0,z)/\gamma m_o v_z]^2} \ . \tag{6.26}$$

The quantity in brackets is the reciprocal of a gyroradius [Eq. (3.38)]. Focusing in the solenoidal lens (as in the immersion lens) is second order; the inward force results from a small azimuthal velocity crossed into the main component of magnetic field. Focusing power is inversely proportional to the square of the particle momentum. The magnetic field must increase proportional to the relativistic mass to maintain a constant lens power. Thus, solenoidal lenses are effective for focusing low-energy electron beams at moderate field levels but are seldom used for beams of ions or high-energy electrons.

6.8 MAGNETIC SECTOR LENS

The lenses of Sections 6.5-6.7 exert cylindrically symmetric forces via paraxial electric and magnetic fields. We now turn attention to devices in which focusing is one dimensional. In other words, if the plane perpendicular to the axis is resolved into appropriate Cartesian coordinates *(x, y)*, the action of focusing forces is different and independent in each direction. The three examples we shall consider are (1) horizontal focusing in a sector magnet (Section 6.8), (2) vertical focusing at the edge of a sector magnet with an inclined boundary (Section 6.9), and (3) quadrupole field lenses (Section 6.10).

   A sector magnet (Fig. 6.15) consists of a gap with uniform magnetic field extending over a bounded region. Focusing about an axis results from the location and shape of the field
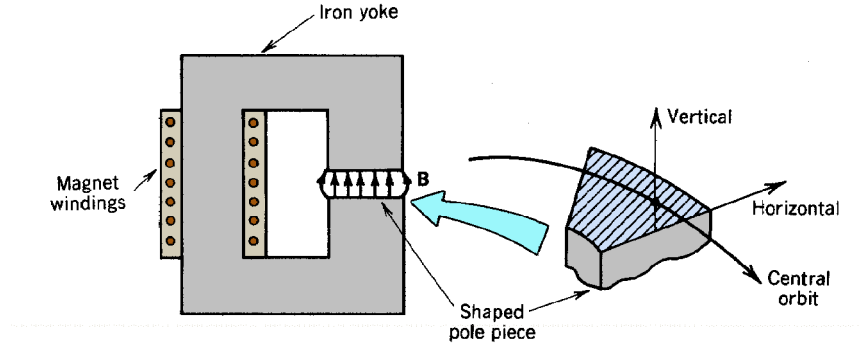
Figure 6.15 Sector field magnet for deflecting a beam showing definition of horizontal and vertical directions with respect to the main beam orbit.

boundaries rather than variations of the field properties. To first approximation, the field is uniform [$\boldsymbol{B} = B_x(x, y, z) \boldsymbol{x} = B_o \boldsymbol{x}$] inside the magnet and falls off sharply at the boundary. The x direction (parallel to the field lines) is usually referred to as the vertical direction. The y direction (perpendicular to the field lines) is the horizontal direction. The beam axis is curved. The axis corresponds to one possible particle orbit called the *central orbit*. The purpose of focusing devices is to confine non-ideal orbits about this line. Sector field magnets are used to bend beams in transport lines and circular accelerators and to separate particles according to momentum in charged particle spectrometers.

   The 180° spectrograph (Fig. 6.16) is an easily visualized example of horizontal focusing in a sector field. Particles of different momentum enter the field through a slit and follow circular orbits with gyroradii proportional to momentum. Particles entering at an angle have a displaced orbit center. Circular orbits have the property that they reconverge after one half revolution with only a second-order error in position. The sector magnet focuses all particles of the same
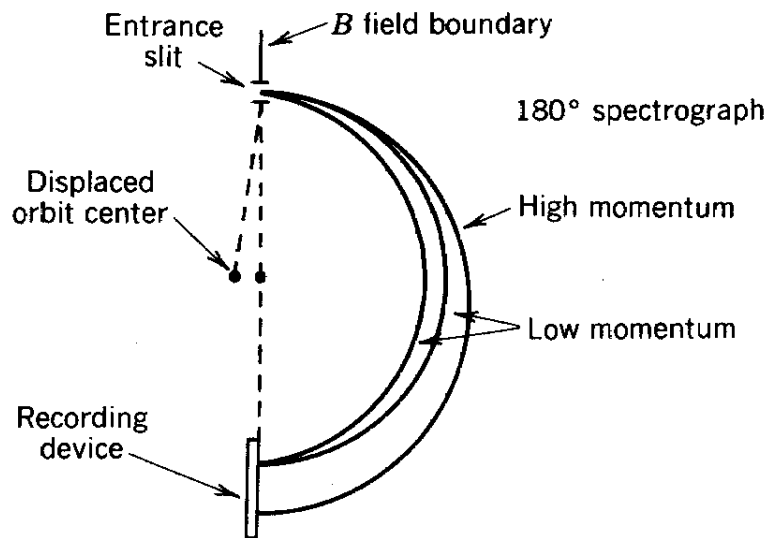

Figure 6.16   Particle focusing by a 180° sector magnet.

128

momentum to a line, independent of entrance angle.Focusing increases the acceptance of the spectrometer. A variety of entrance angles can be accepted without degrading the momentum resolution. The input beam need not be highly collimated so that the flux available for the measurement is maximized. There is no focusing in the vertical direction; a method for achieving simultaneous horizontal and vertical focusing is discussed in Section 6.9.

  A sector field with angular extent less than 180° can act as a thick lens to produce a horizontal convergence of particle orbits after exiting the field. This effect is illustrated in Figure 6.17. Focusing occurs because off-axis particles travel different distances in the field and are bent a different amount. If the field boundaries are perpendicular to the central orbit, we can show, for initially parallel orbits, that the difference in bending is linearly proportional to the distance from the axis.

  The orbit of a particle (initially parallel to the axis) displaced a distance Δr_l from the axis is shown in Figure 6.17. The final displacement is related by $\Delta y_f = \Delta y_l \cos\alpha$, where α is the angular extent of the sector. The particle emerges from the lens at an angle $\Delta\theta = -\Delta y_l \sin\alpha/r_g$, where r_g, is the gyroradius in the field B_o. Given the final position and angle, the distance from the field boundary to the focal point is

$$f' = r_g \, / \tan \, \alpha. \tag{6.27}$$

The focal distance is positive for $\alpha < 90°$; emerging particle orbits are convergent. It is zero at $\alpha = 90°$; initially parallel particles are focused to a point at the exit of a 90° sector. At 180° the focusing distance approaches infinity.
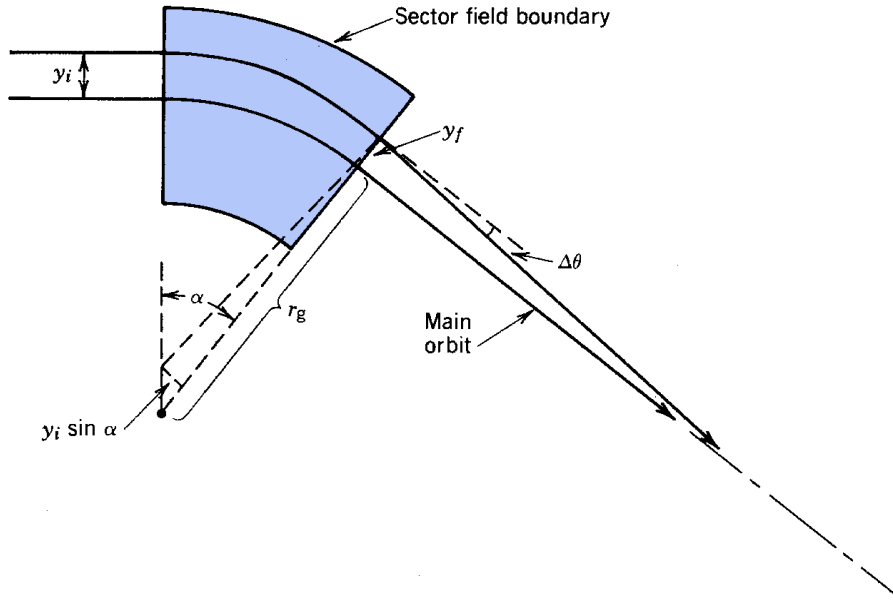

Figure 6.17 Geometry for calculating horizontal focal properties of a sector magnet.

The sector field magnet must usually be treated as a thick lens. This gives us an opportunity to reconsider the definition of the principal planes, which must be clarified when the beam axis is curved. The plane H_1 is the surface that gives the correct particle orbits in the image space. The appropriate construction is illustrated in Figure 6.18a. A line parallel to the beam axis in the image plane is projected backward. The principal plane is perpendicular to this line. The exit orbit intersects the plane at a distance equal to the entrance distance. If a parallel particle enters the sector field a distance y_1 from the beam axis, its exit orbit is given by the line joining the focal point with a point on the principal plane y_1 from the axis. The focal length is the distance from the principal plane to the focal point. The plane H_2 is defined with respect to orbits in the $-z$ direction.

The focal length of a sector can be varied by inclining the boundary with respect to the beam axis. Figure 18b shows a boundary with a positive inclination angle, β. When the inclination angle is negative, particles at a larger distance from the central orbit gyrocenter travel longer distances
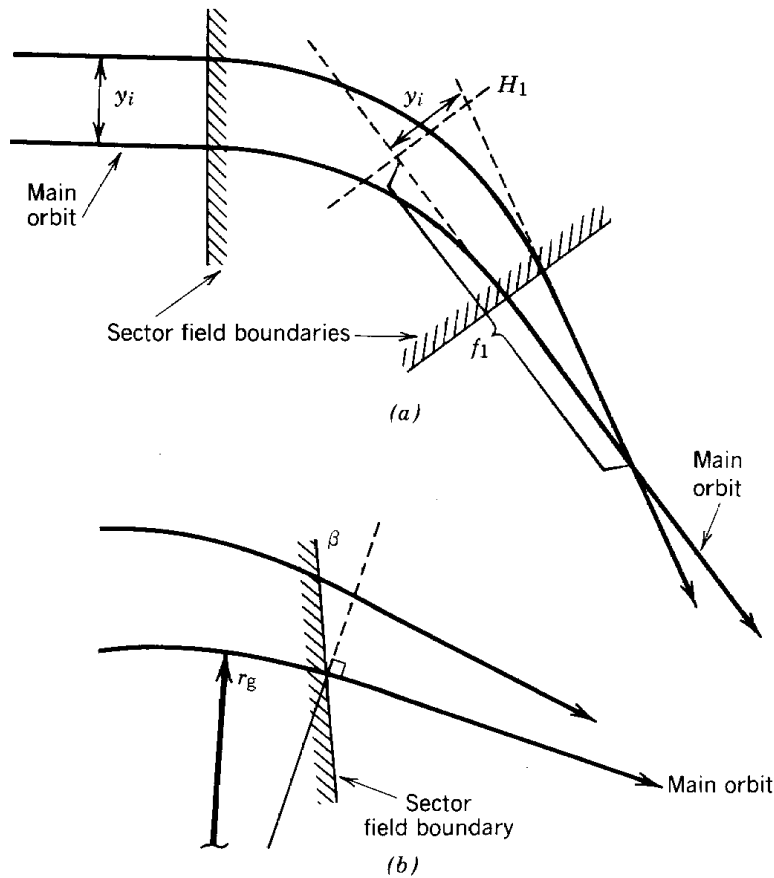

Figure 6.18 Focal properties of a sector magnet. (*a*) Definition of principal planes and focal lengths with a curved main orbit; thick-lens treatment of horizontal focusing in a sector magnet. (*b*) Effect on horizontal focusing of an inclination of the field boundary with respect to the main orbit.

130

in the field and are bent more. The focusing power of the lens in the horizontal direction is increased. Conversely, for $\beta > 0$, horizontal focusing is decreased. We will see in Section 6.9 that in this case there is vertical focusing by the fringing fields of the inclined boundary.

A geometric variant of the sector field is the toroidal field sector lens. This is shown in Figure 6.19. A number of magnet coils are arrayed about an axis to produce an azimuthal magnetic field. The fields in the spaces between coils are similar to sector fields. The field boundary is determined by the coils. It is assumed that there are enough coils so that the fields are almost symmetric in azimuth. The field is not radially uniform but varies as $B_\theta(R,Z) = B_o R_o/R$, where R is the distance from the lens axis. Nonetheless, boundaries can still be determined to focus particles to the lens axis; the boundaries are no longer straight lines. The figure shows a toroidal field sector lens designed to focus a parallel, annular beam of particles to a point.

The location of the focal point for a toroidal sector lens depends on the particle momentum. Spectrometers based on the toroidal fields are called *orange spectrometers* because of the resemblance of the coils to the sections of an orange when viewed from the axis. They have the advantage of an extremely large solid angle of acceptance and can be used for measurements at
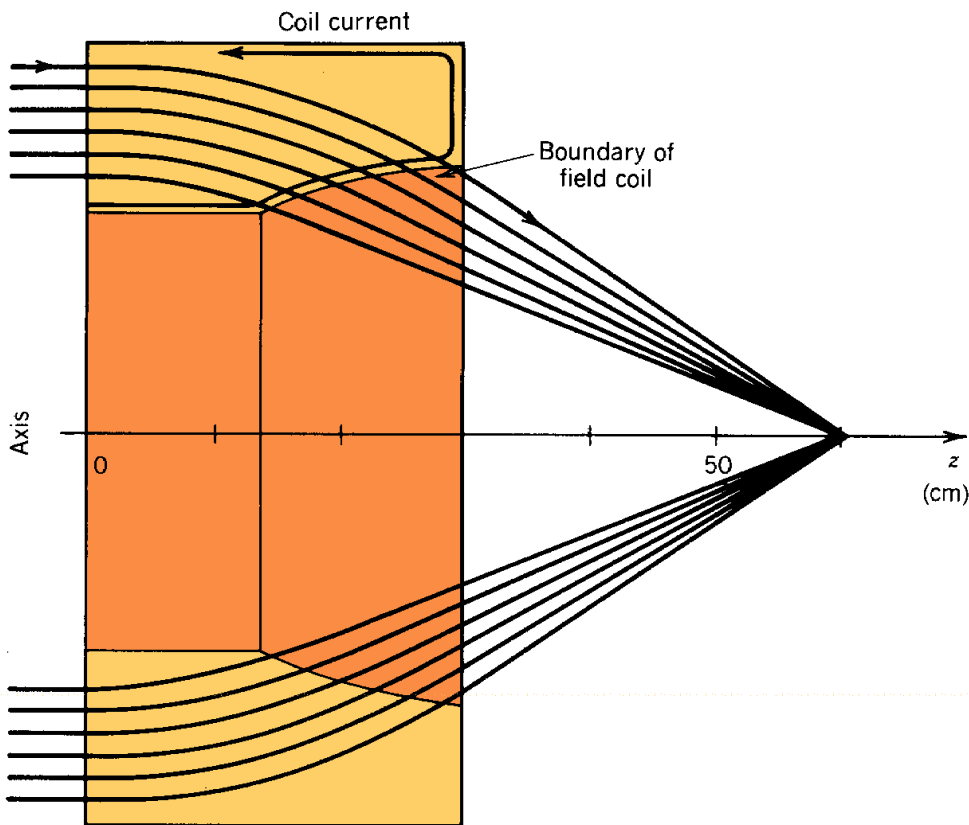

Figure 6.19 Particle orbits in a toroidal field lens with an exit boundary optimized for focusing an annular beam to a spot.

low flux levels. The large acceptance outweighs the disadvantage of particle loss on the coils.

The toroidal field sector lens illustrates the advantages gained by locating applied currents within the volume of the beam. The lens provides first-order focusing with cylindrical symmetry about an axis, as contrasted to the solenoidal field lens, which has second-order focusing. The ability to fine tune applied fields in the beam volume allows correction of focusing errors (aberrations) that are unavoidable in lenses with only external currents.

6.9 EDGE FOCUSING

The term edge focusing refers to the vertical forces exerted on charged particles at a sector magnet boundary that is inclined with respect to the main orbit. Figure 6.20 shows the fringing field pattern at the edge of a sector field. The vertical field magnitude decreases away from the magnet over a scale length comparable to the gap width. Fringing fields were neglected in treating perpendicular boundaries in Section 6.8. This is justified if the gap width is small compared to the particle gyroradius. In this case, the net horizontal deflection is about the same whether or not some field lines bulge out of the gap. With perpendicular boundaries, there is no force in the vertical direction because $B_y = 0$.

In analyzing the inclined boundary, the coordinate z is parallel to the beam axis, and the coordinate ξ is referenced to the sector boundary (Fig. 6.20). When the inclination angle β is nonzero, there is a component of **B** in the y direction which produces a vertical force at the edge when crossed into the particle v_z. The focusing action can be calculated easily if the edge is treated as a thin lens; in other words, the edge forces are assumed to provide an impulse to the particles. The momentum change in the vertical direction is

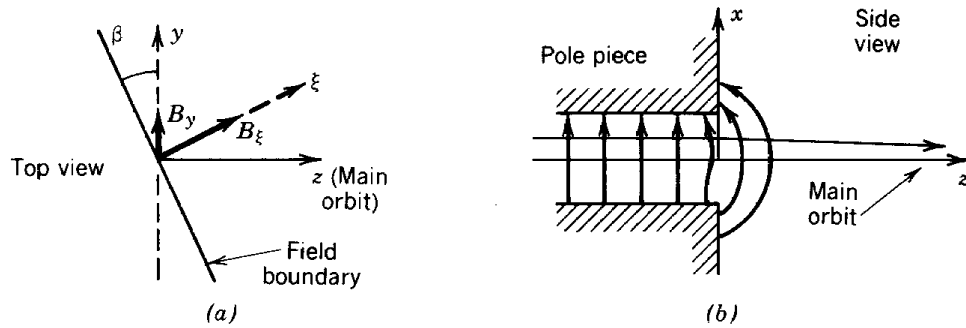$$\Delta P_x = \int dt \ (qv_z B_y). \tag{6.28}$$

Figure 6.20 Geometry for calculating vertical focusing by a sector magnet boundary inclined with respect to the main orbit (edge focusing). (*a*) Field components at exit boundary, viewed along vertical direction (top view). (*b*) View of exit boundary along horizontal direction (side view).
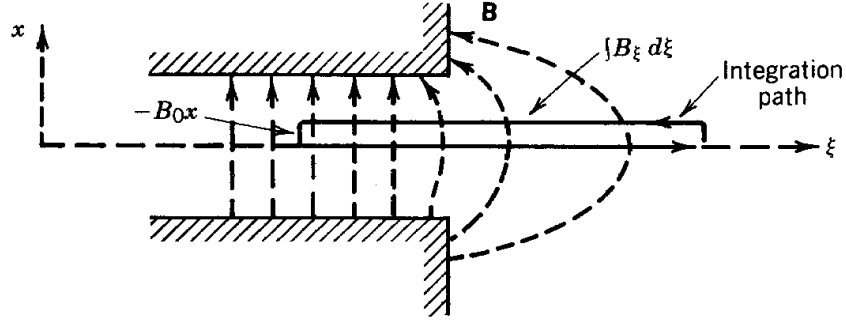
Figure 6.21   Geometry for evaluating field integral relevant to edge focusing.

The integral is taken over the time the particle is in the fringing field. The y component of magnetic field is related to the ξ component of the fringing field by $B_y = B_\xi \sin \beta$. The integral of Eq. (6.28) can be converted to an integral over the particle path noting that $v_z dt = dz$. Finally, the differential path element can be related to the incremental quantity $d\xi$ by $dz = d\xi / \cos \beta$. Equation (6.28) becomes

$$\Delta v_x = (e/\gamma m_o) \int d\zeta \, B_\zeta \, \tan\beta. \tag{6.29}$$

This integral can be evaluated by applying the equation $\int \mathbf{B} \cdot \mathbf{ds} = 0$ to the geometry of Figure 6.21. The circuital integral extends from the uniform field region inside the sector magnet to the zero field region outside. This implies that $\int B_\xi d\xi = B_o x$. Substituting into Eq. (6.29), the vertical momentum change can be calculated. It is proportional to x, and the focal length can be determined in the usual manner as

$$f_x = \frac{\gamma m_o v_z / q B_o}{\tan\beta} = \frac{r_{go}}{\tan\beta}. \tag{6.30}$$

The quantity r_{go} is the particle gyroradius inside the constant-field sector magnet. When $\beta = 0$ (perpendicular boundary), there is no vertical focusing, as expected. When $\beta > 0$, there is vertical focusing, and the horizontal focusing is decreased. If β is positive and not too large, there can still be a positive horizontal focal length. In this case, the sector magnet can focus in both directions. This is the principal of the dual-focusing magnetic spectrometer, illustrated in Figure 6.22. Conditions for producing an image of a point source can be calculated using geometric arguments similar to those already used. Combined edge and sector focusing has also been used in a high-energy accelerator, the zero-gradient synchrotron [A. V. Crewe, *Proc. Intern. Conf. High Energv Accelerators*, CERN, Geneva, 1959, p. 359] (Section 15.5).

6. 10 MAGNETIC QUADRUPOLE LENS

The magnetic quadrupole field was introduced in Section 5.8. A quadrupole field lens is illustrated in Figure 5.16. It consists of a magnetic field produced by hyperbolically shaped pole pieces extending axially a length l. In terms of the transverse axes defined in Figure 5.161, the field components are $B_x = B_o y/a$ and $B_y = B_o x/a$. Because the transverse magnetic deflections are normal to the field components, $F_x \sim x$ and $F_y \sim y$. Motions in the transverse directions are independent, and the forces are linear. We can analyze motion in each direction separately, and we know (from Section 6.3) that the linear fields will act as one-dimensional focusing (or defocusing) lenses.

The orbit equations are

$$d^2 y/dz^2 = (qB_o/\gamma m_o a v_z) \; y, \tag{6.31}$$

$$d^2 x/dz^2 = -(qB_o/\gamma m_o a v_z) \; x. \tag{6.32}$$

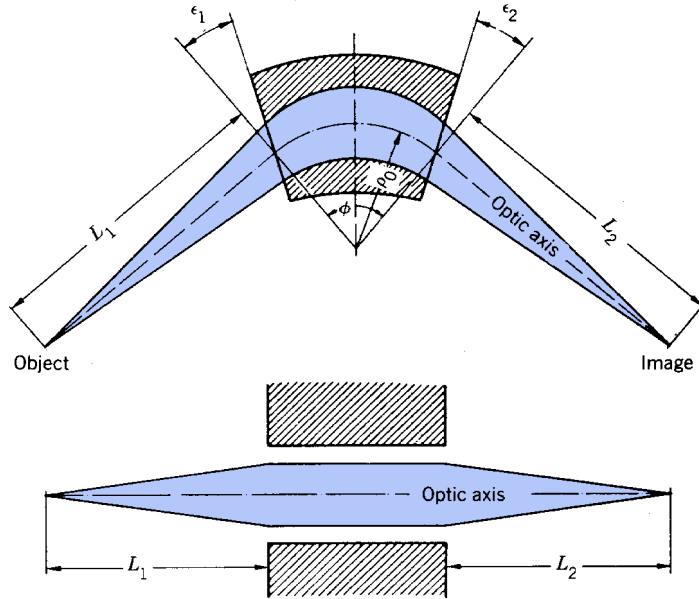The time derivatives were converted to axial derivatives. The solutions for the particle orbits are

Figure 6.22 A homogeneous sector field in which the particle beam crosses the boundary obliquely. Proper choice of the angles ε_1 and ε_2 gives stigmatic focusing in both the radial and vertical directions. (Courtesy, H. Wollnik.)

134

$$x(z) = x_1 \cos\sqrt{\kappa_m}z + x_1' \sin\sqrt{\kappa_m}z / \sqrt{\kappa_m}, \qquad (6.33)$$

$$x'(z) = -x_1 \sqrt{\kappa_m} \sin\sqrt{\kappa_m}z + x_1' \cos\sqrt{\kappa_m}z. \qquad (6.34)$$

$$y(z) = y_1 \cos\sqrt{\kappa_m}z + y_1' \sin\sqrt{\kappa_m}z / \sqrt{\kappa_m}, \qquad (6.35)$$

$$y'(z) = y_1 \sqrt{\kappa_m} \sin\sqrt{\kappa_m}z + y_1' \cos\sqrt{\kappa_m}z. \qquad (6.36)$$

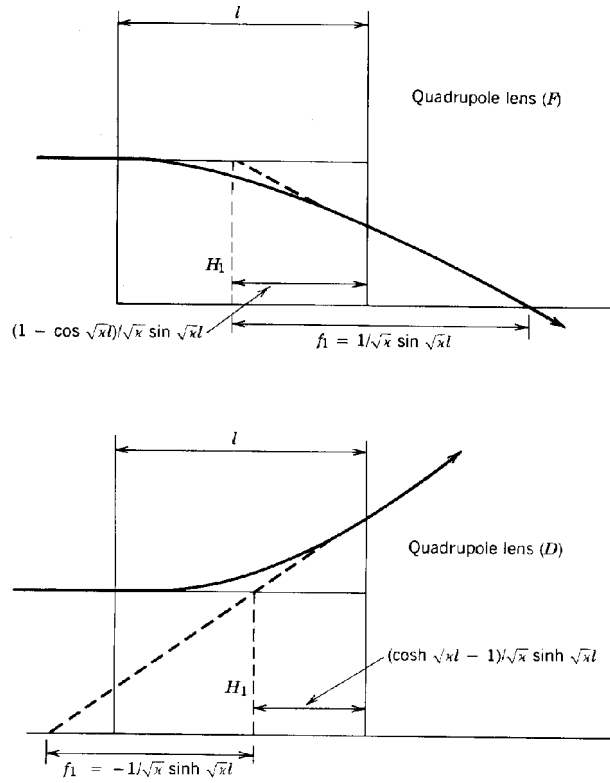where x_1, y_1, x_1', and y_1' are the initial positions and angles. The parameter κ_m is

Figure 6.23 Principal planes and focal lengths for a magnetic quadrupole lens.

135

$$\kappa_m = qB_o/\gamma m_o a v_z \quad (m^{-2}) \tag{6.37}$$

where B_o is the magnetic field magnitude at the surface of the pole piece closest to the axis and a is the minimum distance from the axis to the pole surface. A similar expression applies to the electrostatic quadrupole lens

$$\kappa_e = qE_o/\gamma m_o a v_z^2. \quad (m^{-2}) \tag{6.38}$$

In the electrostatic case, the x and y axes are defined as in Figure 4.14.

The principal plane and focal length for a magnetic quadrupole lens are shown in Figure 6.23 for the x and y directions. They are determined from the orbit expressions of Eqs. (6.33) and (6.34). The lens acts symmetrically for particle motion in either the $+z$ or $-z$ directions. The lens focuses in the x direction but defocuses in the y direction. If the field coils are rotated $90°$ (exchanging North and South poles), there is focusing in y but defocusing in x. Quadrupole lenses are used extensively for beam transport applications. They must be used in combinations to focus a beam about the axis. Chapter 8 will show that the net effect of equal focusing and defocusing quadrupole lenses is focusing.

7

Calculation of Particle Orbits in Focusing Fields

In this chapter, we shall study methods for calculating particle orbits in extended regions of static electromagnetic forces. One important application of such calculations is the determination of electric or magnetic lens properties. Once the fields have been calculated by the Laplace equation, orbit solutions lead to the four discrete quantities that characterize a linear lens (focal lengths and principal points). Properties of orbits in complex optical systems with many focusing elements or in long periodic lens arrays can then be predicted by the combination of the discrete lens parameters through matrix algebra; this is the subject of Chapter 8. The matrix approach gives information on orbits only at the lens boundaries. If detailed information on orbits inside the lenses is required, then the numerical methods of this chapter must be extended through the entire optical system. The matrix approach is not applicable to some accelerators, such as the betatron, with focusing forces that are invariant along the direction of beam propagation. In this case, the best approach is the direct solution of orbits in the extended fields.

   Section 7.1 discusses general features of particle orbits in constant transverse forces and introduces betatron oscillations. Some concepts and parameters fundamental to charged particle accelerators are introduced in Section 7.2, including beam distribution functions, focusing channel acceptance, the ν value in a circular accelerator, and orbital resonance instabilities. An example of focusing in continuous fields, particle motion in a magnetic gradient field, is treated in Section 7.3. This transport method is used in betatrons and cyclotrons.

   Methods to solve particle orbits in cylindrically symmetric electric and magnetic fields are reviewed in the second part of the chapter. The paraxial ray equation is derived in Section 7.5. This equation has extensive applications in all regimes of particle acceleration, from cathode ray

tubes to multi-GeV linacs. As a preliminary to the paraxial ray equation, the Busch theorem is derived in Section 7.4. This theorem demonstrates the conservation of canonical angular momentum in cylindrically symmetric electric and magnetic fields. Section 7.6 introduces methods for the numerical solution of the paraxial ray equation. Two examples are included: determination of the beam envelope in an electrostatic acceleration column and calculation of the focal length of an electrostatic immersion lens. The numerical methods can also be applied to the direct solution of three-dimensional equations of particle motion.

7.1 TRANSVERSE ORBITS IN A CONTINUOUS LINEAR FOCUSING FORCE

In many instances, particle motion transverse to a beam axis is separable along two Cartesian coordinates. This applies to motion in a magnetic gradient field (Section 7.3) and in an array of quadrupole lenses (Section 8.7). Consider one-dimensional transverse paraxial particle motion along the z axis in the presence of a linear force, $F_x = F_o(x/x_b)$. The quantity F_o is the force at the edge of the beam, x_b. The y motion can be treated separately. The axial velocity is approximately constant (Section 6.3). The equation of motion is (Section 2.10)

$$\gamma m_o \ (d^2x/dt^2) \ \cong \ F_o \ (x/x_b). \tag{7.1}$$

In the absence of acceleration, Eq. (7.1) can be expressed as

$$(d^2x/dz^2) \ = \ (F_o/\gamma m_o v_z^2) \ (x/x_b) \tag{7.2}$$

in the paraxial approximation. Equation (7.2) has the solution

$$x(z) \ = \ x_o \ \cos(2\pi z/\lambda_x \ + \ \varphi), \tag{7.3}$$

where

$$\lambda_x \ = \ 2\pi \ \sqrt{\gamma m_o v_z^2 x_b/F_o}.$$

Particle motion is harmonic. All particle orbits have the same wavelength; they differ only in amplitude and phase. Transverse particle motions of this type in accelerators are usually referred to as *betatron oscillations* since they were first described during the development of the betatron [D.W. Kerst and R. Serber, Phys. Rev. **60**, 53 (1941)]. The quantity λ_x is called the *betatron wavelength.*

138

Calculation of Particle Orbits in Focusing Fields

It is often useful to replace the action of an array of discrete lenses by an equivalent continuous transverse focusing force rather than apply the formalisms developed in Chapter 8. This approximation is used, for example, to compare the defocusing effect of continuous-beam space charge forces with confinement forces to derive the maximum allowed current in a quadrupole channel. Orbits in an array of identical, discrete lenses approach the harmonic solution of Eq. (7.3) when the distance between lenses is small compared to the betatron wavelength, as shown in Figure 7.1. Consider lenses of focal length f and axial spacing d in the limit that $d \ll f$ (thin-lens approximation). We want to calculate the change in x and v_x passing through one drift space and one lens. If v_x is the transverse velocity in the drift region, then (following Fig. 7.1)

$$\Delta x = (v_x/v_z) \, d. \tag{7.4}$$

Similarly, by the definition of the focal length.

$$\Delta v_x/v_z - -x / f , \tag{7.5}$$

where x is the particle position entering the thin lens. Equations (7.4) and (7.5) can be converted to differential equations by associating Δz with d and letting $\Delta z \Rightarrow 0$,

$$dx/dz = v_x/v_z, \quad dv_x/dz = - (v_z/fd) \, x.$$

The solution to this equation is again harmonic, with $\lambda_x = (fd)^{1/2}$. The condition for the validity of the continuous approximation, $\lambda_x \gg d$, is equivalent to $d \ll f$. Averaging the transverse force over many lenses gives

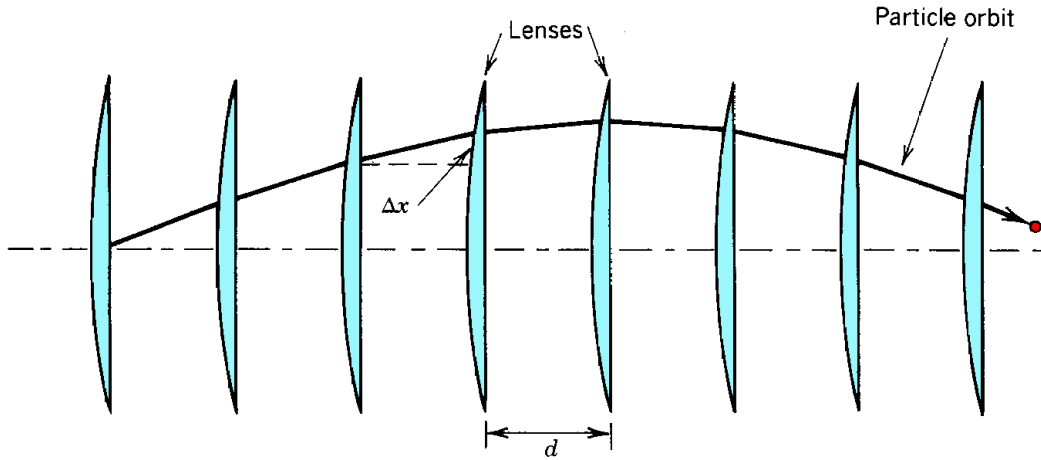$$\overline{F}_x = (\gamma m_o v_z^2/fd) \, x. \tag{7.6}$$

Figure 7.1 Particle orbit in an array of uniform, equally spaced, thin lenses.

Equation (7.6) is derived by expressing Eq. (7.5) in terms of time derivatives and multiplying both sides by γm_o. The conclusion is that particle orbits in any periodic linear focusing system approach harmonic orbits when the betatron wavelength is long compared to the period of the system.

7.2 ACCEPTANCE AND ν VALUE OF A FOCUSING CHANNEL

Perfectly laminar beams cannot be achieved in practice. Imperfections have their origin, in part, in the particle source. For example, thermonic sources produce spatially extended beams at finite current density with a random distribution of transverse velocity components resulting from thermal effects. Laminarity can also be degraded by field errors in beam transport elements. The result is that the particles that constitute a beam have a spread in position and a spread in velocity at each position. The capability of a focusing system is parametrized by the range of particle positions and transverse velocities that can be transported without beam loss. This parameter is called the *acceptance*.

In order to understand the significance of acceptance, we must be familiar with the concept of a particle distribution. The transverse particle distribution of a beam at an axial location is the set of the positions and velocities of all particles $(x_i(z), v_{xi}(z), y_i(z), v_{yi}(z))$. In cylindrical beams, particles are parametrized by $(r_i(z), v_{ri}(z), \theta_i(z), v_{\theta i}(z))$. Methods of collective physics have been developed to organize and to manipulate the large amount of information contained in the distribution. When motions in two dimensions are independent (as in the betatron or a quadrupole focusing channel), distributions in x-v_x and y-v_y can be handled independently.

One-dimensional distributions are visualized graphically by a phase space plot. For motion in the x direction, the axes are v_x (ordinate) and x (abscissa). At a particular axial location, each particle is represented by a point on the plot $(x_i(z), v_{xi}(z))$. A beam distribution is illustrated in Figure 7.2. Normally, there are too many particles in a beam to plot each point; instead, contour lines have been drawn to indicate regions of different densities of particle points. In the specific case shown, particles in the beam are symmetric about the x axis but asymmetric in velocity. This corresponds to a beam launched on the axis with an aiming error. The vertical extent of the distribution indicates that there is a velocity spread at each position. In a laminar beam, all particles at the same position have the same transverse velocity. The phase space plot for a laminar beam is therefore a straight line of zero thickness.

Acceptance is the set of all particle orbit parameters (x_i, v_{xi}) at the entrance to a focusing system or optical element that allow particles to propagate through the system without loss. Acceptance is indicated as a bounded area on a phase space plot. Clearly, the particle distribution at the entrance to a focusing channel must be enclosed within the acceptance to avoid beam loss. For example, the acceptance of a one-dimensional aperture is illustrated in Figure 7.3a. All particles with displacement $x_i < x_o$ pass through, independent of v_{xi}. An acceptable particle distribution boundary is designated as a dashed line. *Matching* a beam to a focusing system consists of operating on the beam distribution so that it is enclosed in the acceptance. For example, matching
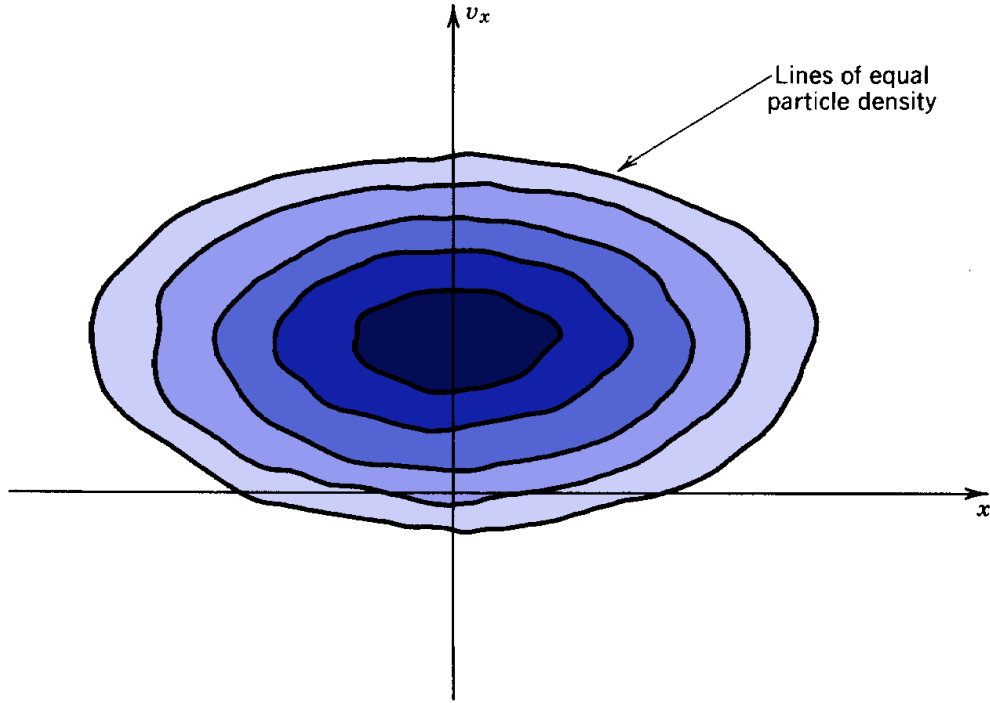
Figure 7.2 Phase space distribution of particles in a beam. Density of particles ((number of particles)/($\Delta x \, \Delta v_x$)) versus x and v_x. Beam is centered on axis, but aimed in $+x$ direction.

to the aperture is simple. The beam is focused by an upstream lens so that the displacement of the peripheral particles is less than x_o. As a second example, consider the acceptance of the continuous linear focusing system discussed in Section 7.1. We assume that there is some maximum dimension beyond which particles are lost, $x_{max} = x_o$. This may be the width of the vacuum chamber. The focusing force and the maximum width define the maximum transverse velocity for confined particle orbits,

$$v_x \leq v_z \, (2\pi x_o/\lambda_x). \tag{7.7}$$

The acceptance of a linear focusing system has boundaries on both axes of an x-v_x plot (Fig. 7.3b). A more detailed analysis shows that the allowed orbit parameters fill an ellipse with major (or minor) radii x_o and $(2\pi x_o/\lambda_x)v_z$. The maximum velocity for the discrete lens system (in the continuous approximation) is

$$v_x \leq v_z \, \sqrt{x_o^2/fd}. \tag{7.8}$$

A large acceptance means that the system can transport particles with a wide spread in entrance position and angle. A transport system with small acceptance places constraints on the size of and
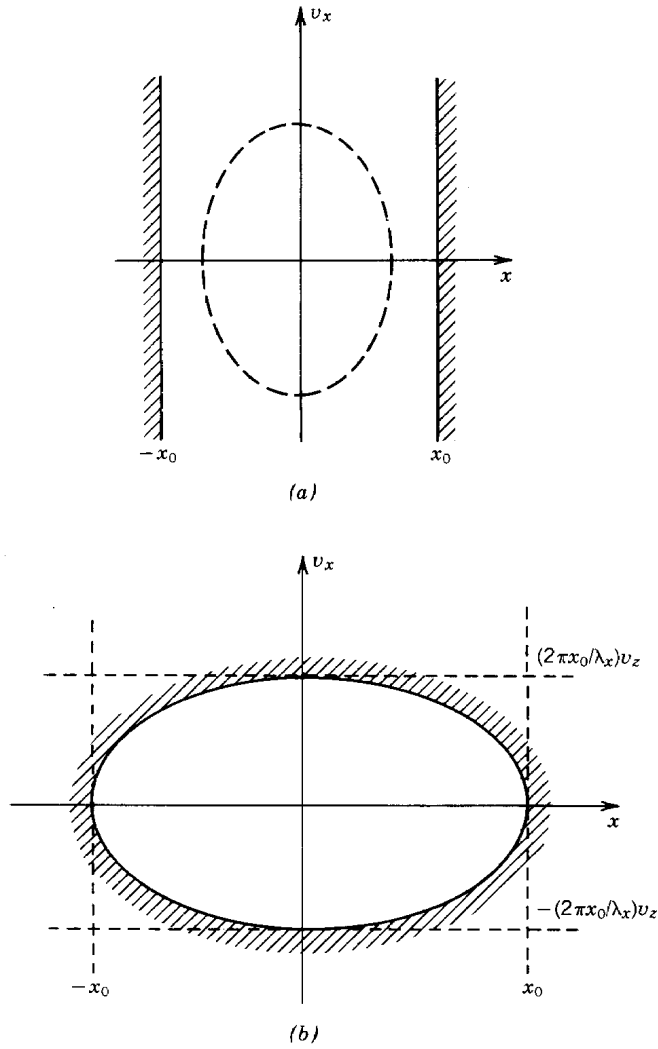
141

Figure 7.3 Acceptance of transport elements. (*a*) A one-dimensional aperture; slot of width $2x_0$. Dashed line indicates a beam distribution that can pass without attenuation. (*b*) One-dimensional continuous focusing system with linear forces.

current density from a particle source. Generally, low beam flux is associated with small acceptance. For a given maximum channel dimension, the acceptance grows with increased focusing force (F_o). This results in shorter betatron wavelength.

The quantity ν is defined for circular transport systems, such as betatrons, synchrotrons, or storage rings. It is the ratio of the circumference of the system (C) to the betatron wavelength. The betatron wavelength may differ in the two transverse directions, so that

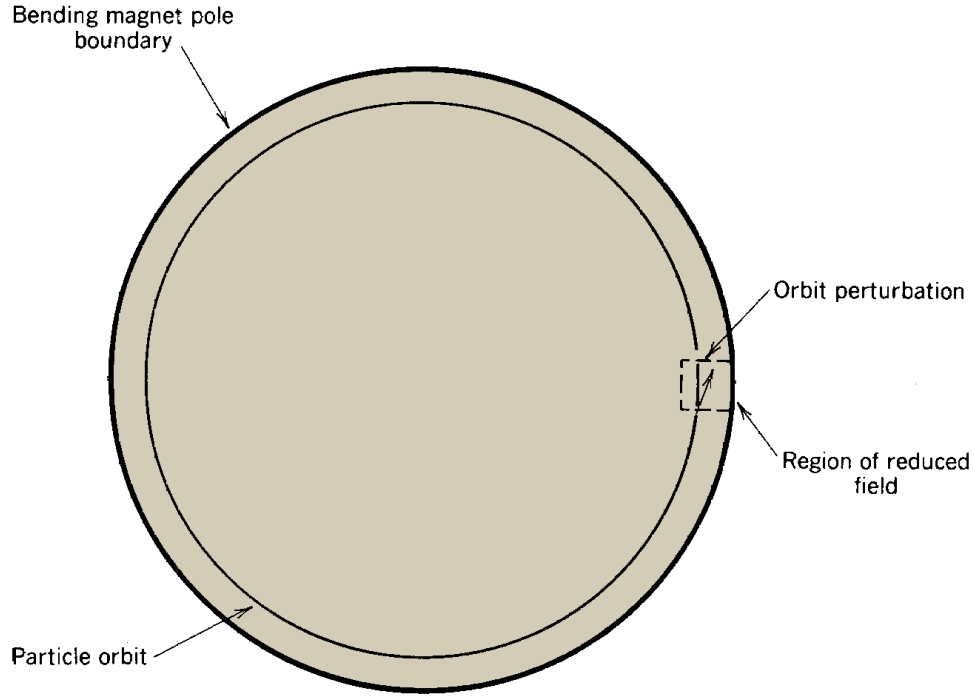$$\nu_x = C/\lambda_x, \qquad \nu_y = C/\lambda_y. \tag{7.9}$$

Figure 7.4 Bending magnetic field of a circular accelerator with a field error.

The number v is also given by

$$v = \frac{frequency\ of\ transverse\ oscillations}{frequency\ of\ rotation} . \tag{7.10}$$

A short betatron wavelength is equivalent to a high value of v. Thus, increased v is associated with stronger focusing and increased acceptance.

When the quantity v has an integer value, there is the possibility of a resonance instability in a circular system [E. D. Courant, J. Appl. Phys. **20**, 611 (1949)]. The physical basis of a resonance instability at $v_x = 1$ is illustrated in Figure 7.4. Assume that a circular accelerator has an imperfection at an azimuthal position, such as a dip in field magnitude of a bending magnet. The reduced field represents a localized outward force that gives particles an impulse each time they pass. If $v_x \neq 1$ the impulse acts during different phases of the betatron oscillation. The driving force is nonresonant, and the resulting oscillation amplitude is finite. When $v_x = 1$ the driving force is in resonance with the particle oscillation. The impulse is correlated with the betatron oscillation so that the oscillation amplitude increases on each revolution.

Another view of the situation is that the field perturbation acts to couple periodic motion in the axial direction (rotation) to periodic motion in the transverse direction (betatron oscillation). Coupling is strong when the harmonic modes have the same frequency. The distribution of beam

energy is anisotropic; the axial energy is much larger than the transverse energy. Thus, energy is transferred to the transverse oscillations, ultimately resulting in particle loss. The condition $v_x = 1$ or $v_y = 1$ must always be avoided.

The model of Figure 7.5 is an analogy for resonant instabilities. A harmonic oscillator is deflected by a time-dependent forcing function. We assume the forcing function exerts an impulse Δp with periodicity $2\pi/\omega$:

$$F(t) = \Delta p \; \delta \; (t - 2m\pi/\omega) \quad (m = 1,2,3,...).$$

The Fourier analysis of this function is

$$F(t) = \frac{\Delta p \; \omega}{\pi} \left[\tfrac{1}{2} + \sum_{n+1}^{\infty} \cos(n\omega t) \right]. \tag{7.11}$$

The steady-state response of an undamped oscillator with characteristic frequency ω_o to a forcing function with frequency $n\omega$ is

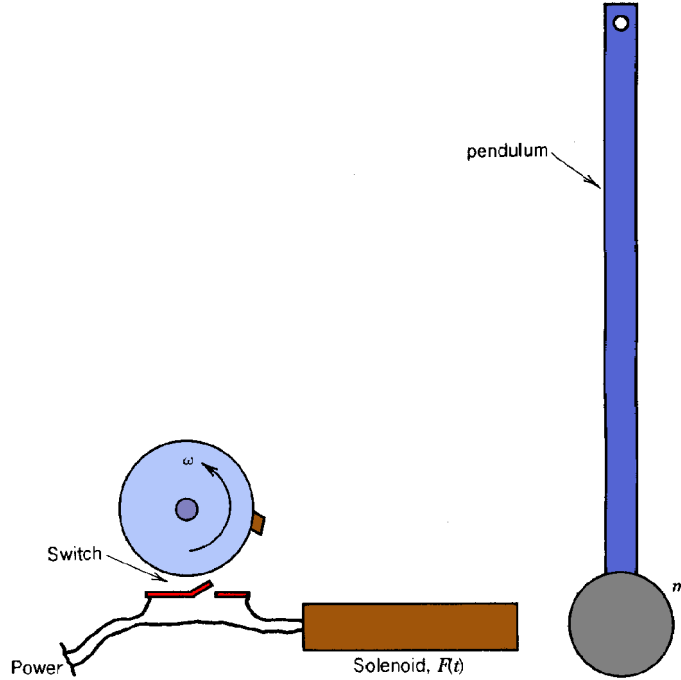$$x(t) = \frac{\Delta p \; \omega}{m\pi} \frac{\cos(n\omega t)}{\left(\omega_o^2 - (n\omega)^2 \right)} . \tag{7.12}$$

Figure 7.5   Analogy for resonance instability; pendulum driven by a periodic impulse.

The response of the linear system to the force of Eq. (7.11) is (by superposition)

$$x(t) = \frac{\Delta p\ \omega}{m\pi} \left(\frac{\cos(\omega t)}{\omega_o^2 - n\omega^2} + \frac{\cos(2\omega t)}{\omega_o^2 - 4\omega^2} + \frac{\cos(3\omega t)}{\omega_o^2 - 9\omega^2} + ... \right) . \qquad (7.13)$$

The pendulum mass represents a beam particle deflected from the primary orbit. The betatron oscillation frequency is ω_o. If we assume that $F(t)$ represents a system perturbation at a particular azimuth, then ω is the rotation frequency of the particle. By Eq. (7.10), $v = \omega_o/\omega$. Equation (7.13) can be rewritten

$$x(t) = \frac{\Delta p\ \omega}{m\pi} \left(\frac{\cos(\omega t)}{v^2 - 1} + \frac{\cos(2\omega t)}{v^2 - 4} + \frac{\cos(3\omega t)}{v^2 - 9} + ... \right) . \qquad (7.14)$$

Thus, the steady-state amplitude of particle oscillations diverges when v has an integer value. A complete analysis of the time-dependent response of the particles shows that the maximum growth rate of oscillations occurs for the $v = 1$ resonance and decreases with higher-order numbers. Systems with high v and strong focusing are susceptible to resonance instabilities. Resonance instabilities do not occur in weak focusing systems where $v < 1$.

7.3 BETATRON OSCILLATIONS

The most familiar example of focusing in an accelerator by continuous fields occurs in the betatron. In this device, electrons are confined for relatively long times as they are inductively accelerated to high energy. We shall concentrate on transport problems for constant energy particles in this section. The treatment is generalized to particles with changing energy in Chapter 11.

   Section 3.7 showed how a uniform magnetic field confines an energetic charged particle in a circular orbit normal to the field. Particles can drift freely along the field direction. In a betatron, particles are enclosed in a toroidal vacuum chamber centered on the main circular orbit. Beams always have spreads in angle and position of particle orbits about the main orbit. It is necessary to supplement the uniform field with additional field components so that non-ideal particle orbits oscillate about the main axis rather than drift away. Coordinates to analyze particle motion are shown in Figure 7.6. One set *(x, z, s)* is referenced to the primary orbit: *s* points along the beam axis, *x* is normal to *z* and the field, while *z* is directed along the field. We shall also use polar coordinates *(r, θ, z)* centered at the main orbit gyrocenter, which is also the axis of symmetry of the field.
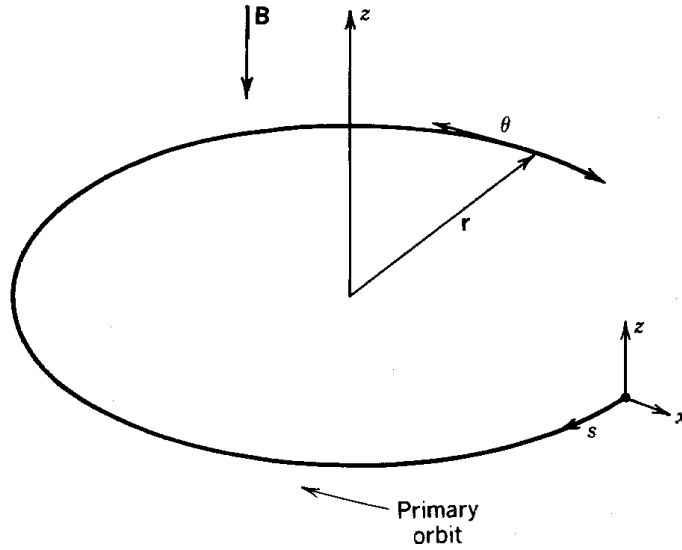
Figure 7.6 Coordinate system for analyzing betatron oscillations in an axisymmetric magnetic field with a radial gradient.

To begin, consider motion in a uniform magnetic field, B_o. Orbits viewed normal to the field are circles, including the orbits of perturbed particles (Fig. 7.7). The particle path shown as a solid line Figure 7.7 has nonzero radial velocity at the primary orbit. This is equivalent to a displacement of its gyrocenter from the system axis. Note that excursions away from the primary orbit are bounded and approximately harmonic. In this sense, there is *radial focusing* in a uniform magnetic field. A particle distribution with a spread in v_x occupies a bounded region in x. This is not true in the z direction. A spread in v_z causes the boundary of the particle distribution to expand indefinitely. In order to confine a beam, we must either add additional focusing lenses around the torus to supplement the bending field or modify the bending field. We shall consider the latter option and confine attention to fields with azimuthal symmetry.
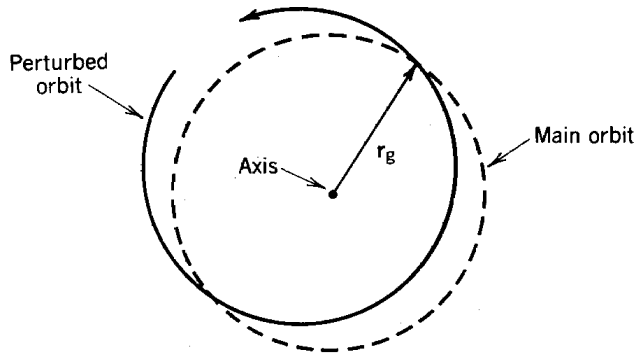

Figure 7.7 Radial focusing in a uniform bending field. Transverse velocity with respect to the main orbit corresponds to a displaced gyrocenter.

146

Calculation of Particle Orbits in Focusing Fields

The zero-order particle velocity is in the θ direction relative to the field axis. The magnetic field must have a radial component in order to exert a force in the z direction. Consider, first, the field distribution from an air core magnet. Figure 7.8a shows a uniform solenoidal field. If extra windings are added to the ends of the solenoid (Fig. 7.8b), the field magnitude increases away from the midplane. The bent field lines have a component B_r. In the paraxial approximation

$$B_r \cong -(r/2) \ [dB_z(0,z)/dz]. \tag{7.15}$$

The variation of B_r and B_z about the axis of symmetry of the field is sketched in Figure 7.8c. The axial field is minimum at $z = 0$; therefore, B_r varies approximately linearly with z about this plane at a constant radius. Directions of the cross products are indicated in Figure 7.8b. The axial force is in the $-z$ direction for $z > 0$ and in the $+z$ direction for $z < 0$. Particles are confined about the plane of minimum B_z. A field with magnitude decreasing away from a plane is defocusing.
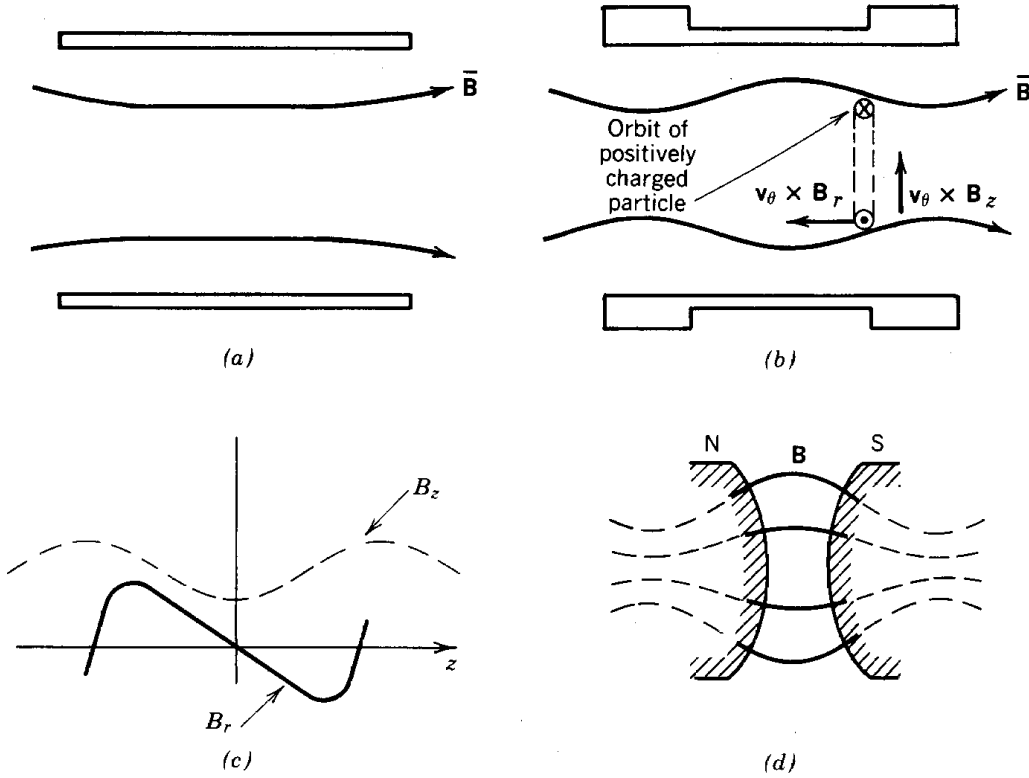

Figure 7.8 Axisymmetric magnetic field with radial gradient. (a) Field lines of a solenoidal coil. (b) Addition of end coils to generate magnetic mirror; forces on particle with axicentered orbit. (c) Axial variations of B_z and B_r in a mirror field. (d) Generation of mirror field in a gap by shaping magnet poles to conform to magnetic equipotential lines.

147

Calculation of Particle Orbits in Focusing Fields

The geometry of Figure 7.8b is used for the confinement of hot fusion plasmas. It is called the *magnetic mirror* because particles are reflected from the region of increased B_z. In accelerator applications, particles are confined to a small region about $z = 0$. Following the discussion of Section 5.7, iron is used to carry the magnetic flux in all other regions to minimize power requirements. We can easily determine the shape of non-saturated pole pieces that will generate the same field patterns as Figures 7.8a and b by following the method of Section 5.5. The pole faces must lie on surfaces of constant magnetic potential normal to the field lines. After choosing the gap width, the surfaces are determined by connecting a curve everywhere normal to the field lines (Fig. 7.8d). Most vacuum field patterns generated by distributed coils can be duplicated by shaped pole pieces.

The equation $\nabla \times \mathbf{B} = 0$ implies that

$$\partial B_z/\partial r = \partial B_r/\partial z. \tag{7.16}$$

Taking the partial derivative of Eq. (7.15) leads to

$$\partial B_z/\partial r = - (r/2) \ [\partial^2 B_z(0,z)/\partial z^2]$$

$$or \quad B_z(r,z) \cong B_o - (r^2/4) \ [\partial^2 B_z(0,z)/\partial z^2]. \tag{7.17}$$

The second derivative of B_z is positive at the symmetry plane for a magnetic mirror. Thus, $B_z(r, 0)$ is not uniform, but has a negative radial gradient. The bending field gradient is usually parametrized by the *field index*. The field index is a function of radius given by

$$n(r) = - [r/B_z(r,0)] \ [\partial B_z(r,0)/\partial r]. \tag{7.18}$$

Comparing Eqs. (7.17) and (7.18), the magnitude of the field index increases quadratically with radius in the symmetry plane of a paraxial magnetic field:

$$n(r) = [r^2/2B_z(r)] \ [\partial^2 B_z(0,z)/\partial z^2].$$

The field index is positive for a mirror field.

We can now derive equations for the orbits of constant energy particles in a bending field with a gradient. Assume that the spread of particle angles and position is small so that the beam is localized about an ideal circular orbit with $r = r_g$ and $z = 0$. The bending field and field index values at the position of the, ideal orbit are $B_o = B_z(r_g,0)$ and $n_o = -(r_g/B_o)[\partial B_z(0,z)/\partial r]$. The bending field and radius of the ideal orbit are related by $r_g = \gamma_o m_o v_\theta/qB_o$. Small orbit perturbations imply that $x = r - r_g \ll r_g$, $z \ll r_g$, $v_x \ll v_\theta$, $v_z \ll v_\theta$ and $v_\theta = v_o$ (a constant). The magnetic field

components are approximated by a Taylor expansion about the point $(r_g, 0)$.

$$B_r \cong B_r(r_g, 0) + (\partial B_r/\partial r)\ x + (\partial B_r/\partial z)\ z, \qquad (7.19)$$

$$B_z \cong B_z(r_g, 0) + (\partial B_z/\partial r)\ x + (\partial B_z/\partial z)\ z. \qquad (7.20)$$

The derivatives are taken at $r = r_g$, $z = 0$. A number of terms can be eliminated. In the symmetry plane, B_z is a minimum so that $\partial B_z/\partial z = 0$. Inspection of Figure 7.8b shows that $B_r(r_g, 0) = 0$. Because B_r is zero everywhere in the symmetry plane, $\partial B_r/\partial r = 0$. Combining this with the condition $\nabla \cdot \mathbf{B} = 0$ implies that $\partial B_z/\partial z = 0$. Finally, the equations $\nabla \times \mathbf{B} = 0$ sets the constraint that $\partial B_r/\partial z = \partial B_z/\partial r$. The magnetic field expressions become

$$B_r \cong (\partial B_z/\partial r)\ z, \qquad (7.21)$$

$$B_z \cong B_o + (\partial B_z/\partial r)\ x, \qquad (7.22)$$

Replacing the bending field gradient with the field index, we find that

$$B_r \cong -\ (n_o B_o/r_g)\ z, \qquad (7.23)$$

$$B_z \cong B_o -\ (n_o B_o/r_g)\ x, \qquad (7.24)$$

We can verify by direct substitution that these fields satisfy the paraxial relation of Eq. (6.7).

The next step is to determine the particle equations of motion for small x and z. The particle energy is a constant (parametrized by γ_o) because only static magnetic fields are present. The relativistic equations of motion are

$$\gamma_o m_o\ (d^2 r/dt^2) = \gamma_o m_o v_\theta^2/r - q v_\theta B_z, \qquad (7.25)$$

$$\gamma_o m_o\ (d^2 z/dt^2) = q v_\theta B_r. \qquad (7.26)$$

The radial equation can be simplified by substituting $x = r - r_g$ and the field expression of Eq. (7.24),

$$d^2 x/dt^2 = v_\theta^2/(r_g + x) - q v_\theta\ (B_o - n_o B_o x/r_g)/\gamma m_o$$

$$\cong (v_\theta^2/r_g) - (v_\theta/r_g)^2\ x - q v_\theta B_o/\gamma_o m_o + (n_o q v_\theta B_o/\gamma_o m_o r_r)\ x. \qquad (7.27)$$

The second expression was derived using the binomial expansion and retaining only first-order terms in xlr,. The zero-order force terms on the right-hand side cancel. The first-order equation of

radial motion is

$$(d^2x/dt^2) \cong -(v_\theta/r_g)^2 \, (1 - n_o) \, x = -\omega_g^2 \, (1 - n_o) \, x. \tag{7.28}$$

The last form is written in terms of the gyrofrequency of the ideal particle orbit. The equation for motion along the bending field lines can be rewritten as

$$(d^2z/dt^2) \cong -\omega_g^2 \, n_o \, z. \tag{7.29}$$

Equations (7.28) and (7.29) describe uncoupled harmonic motions and have the solutions

$$x = x_o \, \cos[\sqrt{1-n_o} \, \omega_g t + \varphi_1], \tag{7.30}$$

$$z = z_o \, \cos[\sqrt{n_o} \, \omega_g t + \varphi_2]. \tag{7.31}$$

The equations for betatron oscillations have some interesting features. In a uniform field ($n_o = 0$), first-order radial particle motion is harmonic about the ideal orbit with frequency ω_g. This is equivalent to a displaced circle, as shown in Figure 7.7. When a field gradient is added, the transverse oscillation frequency is no longer equal to the rotation frequency. We can write

$$\omega_x/\omega_g = \sqrt{1-n_o} = v_x. \tag{7.32}$$

When n_o is positive (a negative field gradient, or mirror field), v_x is less than unity and the restoring force decreases with radius. Particles moving outward are not reflected to the primary axis as soon; conversely, particles moving inward are focused back to the axis more strongly. The result is that the orbits precess, as shown in Figure 7.9. When $n_o > 1$, the field drops off too rapidly to restore outward moving particles to the axis. In this case, $\sqrt{1-n_o}$ is imaginary so that x grows exponentially. This is an example of an *orbital instability*.

In the z direction, particle orbits are stable only when $n_o > 0$. Relating the z oscillation frequency to ω_g gives

$$v_z = \sqrt{n_o}. \tag{7.33}$$

We conclude that particles can be focused around the primary circular orbit in an azimuthally symmetric bending magnet if the field has a negative radial gradient such that
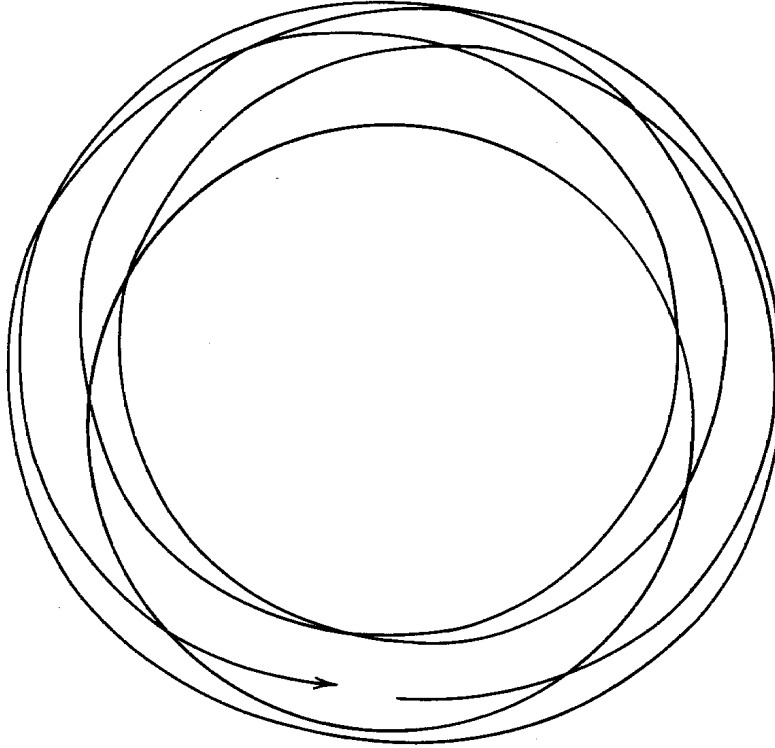
Figure 7.9 Precessing particle orbit in an axisymmetric magnetic field with field index $n = 0.5$; z axis out of page.

$$0 < n_o < 1. \tag{7.34}$$

Focusing of this type in a circular accelerator is called weak focusing. In the stable regime, both v_x and v_z are less than unity. Therefore, resonant instability is not a critical problem in weak focusing machines.

7.4 AZIMUTHAL MOTION OF PARTICLES IN CYLINDRICAL BEAMS

In principle, we have collected sufficient techniques to calculate particle orbits in any steady-state electric or magnetic field. Three equations of motion must be solved simultaneously for the three dimensions. Three components of electric and magnetic fields must be known throughout the region of interest. In practice, this is a difficult procedure even with digital computers. It is costly in either calculational time or memory space to specify field components at all positions.

The paraxial ray equation affords a considerable simplification for the special case of cylindrical beams where particle orbits have small inclination angles with respect to the axis. Use of paraxial forms (Section 6.2) means that electric and magnetic fields can be calculated quickly from
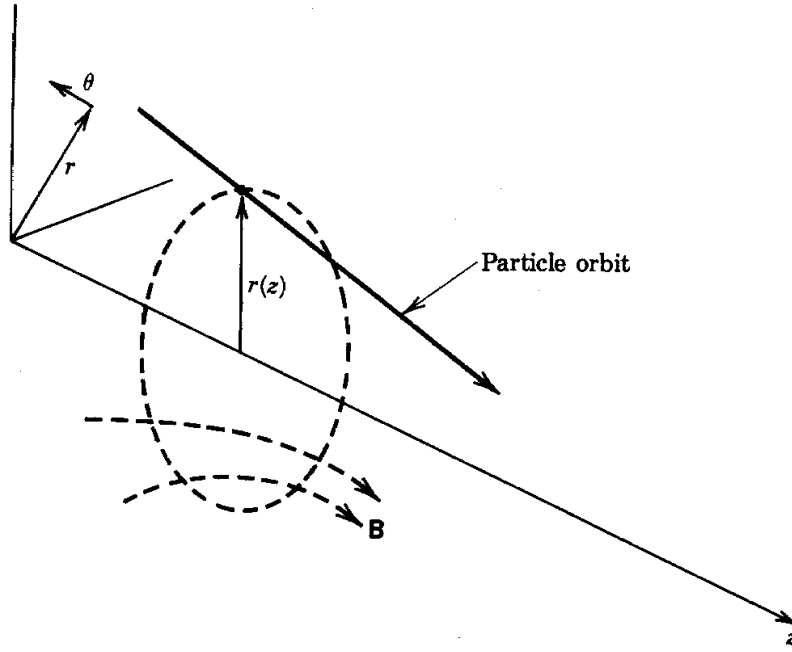
Figure 7.10 Coordinate system and quantities to derive Busch's theorem.

specified quantities on the axis. Symmetry arguments and conservation principles are used to simplify the particle equations of motion. The result is that only one equation for radial motion need be solved to determine the beam envelope. The paraxial ray equation is derived in Section 7.5. In this section, we shall determine a result used in the derivation, the conservation of canonical angular momentum. The method used, the Busch theorem [H. Busch, Z. Phys. **81**, 974 (1926)] provides more physical insight than the usual approach from the Hamiltonian formulation.

Consider a region of azimuthally symmetric, paraxial electric and magnetic fields where particles move almost parallel to the z axis. A cylindrical coordinate system (r, θ, z) is referenced to the beam axis (Fig. 7.10). (Note that this coordinate system differs from the one used in Section 7.3.) We seek an equation that describes the azimuthal motion of charged particles in terms of on-axis quantities. The Lorentz force law for azimuthal motion [Eq. (3.34)] is

$$(dP_\theta/dt) + p_r \, (d\theta/dt) = q \, [(dr/dt) \, B_z - (dz/dt) \, B_r] + qE_\theta. \tag{7.35}$$

Inspection of Eq. (7.35) shows that changes in v_θ arise from either interactions of particle velocity with static magnetic field components or an azimuthal electric field. In the paraxial approximation, we will see that such an electric field can arise only from time variations of axial magnetic flux. We will treat the two terms on the right-hand side of Eq. (7.35) separately and then combine them to a modified equation for azimuthal motion. In the modified equation, v_θ depends only on the quantity $B_z(0,z)$.

152

Calculation of Particle Orbits in Focusing Fields

To begin, consider a particle moving thorough a region of static field components B_r and B_z (Fig. 7.10). The *flux function* ψ is defined as the flux of axial magnetic field enclosed in a circle of radius r at z, where r and z are particle coordinates. (Note that this is a calculational definition; the particle does not necessarily move in a circle.) The flux function changes as the particle moves along its orbit. First, assume that the particle moves radially a distance Δr. The change in ψ is

$$\Delta\psi \cong B_z(r,z)\ 2\pi r\ \Delta r. \tag{7.36}$$

Equation (7.36) reflects the fact that B_z is almost constant in the paraxial approximation and that the area of the circle increases by about $2\pi r \Delta r$. Similarly, axial motion produces a change in ψ of

$$\Delta\psi \cong (\pi r^2)\ (\partial B_z/\partial r)\ \Delta z\ =\ -2\pi r\ B_r\ \Delta r. \tag{7.37}$$

The area of the circle is constant, but the magnitude of B_z may change if there is an axial gradient. The last form is derived by substitution from Eq. (6.7).

The change in ψ from a particle motion is obtained by adding Eqs. (7.36) and (7.37). Dividing both sides of the sum by Δt and taking the limit $\Delta t \Rightarrow 0$, we find that

$$d\psi/dt \cong 2\pi r\ [B_z\ (dr/dt)\ -\ B_r\ (dz/dt)]. \tag{7.38}$$

The derivative indicates the change in flux function arising from particle motion when the magnetic fields are static. The right-hand side of Eq. (7.38) is identical to the right side of Eq. (7.35) multiplied by $2\pi r$. Substituting, Eq. (7.35) becomes

$$dp_\theta/dt\ +\ p_r\ d\theta/dt\ =\ (d\psi/dt)/2\pi r. \tag{7.39}$$

The left-hand side of Eq. (7.39) can be modified by noting that $p_\theta = \gamma m_o r(d\theta/dt)$ and $p_r = \gamma m_o(dr/dt)$:

$$\frac{dp_\theta}{dt}\ +\ p_r\ \frac{d\theta}{dt}\ =\ \gamma m_o \left(r\ \frac{d^2\theta}{dt^2}\ +\ \frac{dr}{dt}\ \frac{d\theta}{dt}\ +\ \frac{dr}{dt}\ \frac{d\theta}{dt} \right)\ =\ \frac{1}{r}\ \frac{d(\gamma m_o r^2 d\theta/dt)}{dt}.$$

The final result is that

$$d(\gamma m_o r^2\ d\theta/dt)/dt\ =\ q(d\psi/dt)/2\pi.$$

or

153

$$\gamma m_o r v_\theta \; + \; q\psi/2\pi \; = \; q\psi_o/2\pi. \tag{7.40}$$

The quantity ψ_o is a constant equal to the value of ψ when $v_\theta = 0$. Solving for v_θ,

$$v_\theta \; = \; -(q/2\pi\gamma m_o r) \; (\psi - \psi_o). \tag{7.41}$$

The azimuthal velocity is a function only of r, ψ and ψo. Because particles usually have v$\theta = 0$ when they are generated, ψo is taken as the flux in the source plane enclosed in a circle of radius ro, where ro is the extraction radius. Variation of Bz is second order with radius in the paraxial approximation, so that $\psi \cong (\pi r^2)B_z(0,z).\theta$

Equation (7.40) can be cast in the form familiar from Hamiltonian dynamics by substituting Eq. (4.53) into Eq. (3.25):

$$\psi \; = \; \int_0^r \; (2\pi r' dr') \; [(1/r')\partial(r'A_\theta)/\partial r'] \; = \; 2\pi r A_\theta. \tag{7.42}$$

A_θ is the only allowed component of the vector potential in the paraxial approximation. In this circumstance, the vector potential has a straightforward physical interpretation. It is proportional to the flux enclosed within a radius divided by $2\pi r$. The quantity $\psi/2\pi$ is thus synonymous with the stream function (Section 4.7). Lines of constant enclosed flux must lie along field lines because field lines do not cross one another.

To complete the derivation, we must include the effects on azimuthal motion when the magnetic field changes in time. An azimuthal electrostatic field is not consistent with symmetry in θ because the existence of such a field implies variation of φ along θ. A symmetric azimuthal electric field can be generated inductively by a changing axial magnetic field. We will derive a modified form for the term qE_θ in Eq. (7.35) by neglecting spatial gradients of B_z. By Faraday's law [Eq. (3.26)], the azimuthal electric field acting on a particle at radius r is $E_\theta = d\psi/dt$, where the derivative implies variation of ψ in time neglecting spatial variations. If we add contributions from spatial and temporal variations of ψ, we arrive at Eq. (7.41) as the general modified equation of azimuthal motion. The time derivative is interpreted as the change in ψ arising from all causes. In the Hamiltonian formulation of particle dynamics, the canonical angular momentum in the presence of a magnetic field is constant and is defined as

$$P_\theta \; = \; \gamma m_o r v_\theta \; + \; q r A_\theta \; = \; q\psi_o/2\pi. \tag{7.43}$$

7.5 THE PARAXIAL RAY EQUATION

The paraxial ray equation is derived by combining the properties of paraxial fields, the

conservation of canonical angular momentum, and the conservation of energy. It can be used to determine the envelope (outer radius) of a beam as a function of position along the axis in terms of the electrostatic potential and longitudinal magnetic field on the axis, $\varphi(0, z)$ and $B_z(0, z)$.

The equation is based on the following assumptions.

     1.The beam is cylindrically symmetric.

     2.Beam properties vary in space but not in time.

     3.The fields are cylindrically symmetric, with components E_r, E_z, B_r and B_z. This encompasses all axisymmetric electrostatic lenses and the solenoidal magnetic lens.

     4.The fields are static.

     5.Particle motion is paraxial.

     6. Fields are paraxial and transverse forces are linear.

In the following derivation, it is also assumed that particle orbits are laminar and that there are no self-fields. Terms can be added to the paraxial ray equation to represent spreads in transverse velocity and space charge forces.

The laminarity of orbits means that the radial projections of all particle orbits are similar. They differ only in amplitude. It is thus sufficient to treat only the boundary orbit. The axial velocity is approximately constant in any plane normal to the axis. Time derivatives are replaced by $v_z(d/dz)$ because we are interested in the steady-state beam envelope as a function of axial position. The azimuthal equation of motion is (Section 7.4)

$$d\theta/dt = - (q/2\pi\gamma m_o r^2) \ (\psi - \psi_o). \tag{7.44}$$

The quantity y may vary with axial position since zero-order longitudinal electric fields are included. The only nontrivial equation of motion is in the radial direction:

$$d(\gamma m_o \ dr/dt)/dt - \gamma m_o v_\theta^2/r = q \ (E_r + v_\theta B_z)$$

$$= m_o \ dr/dt \ d\gamma/dt + \gamma m_o \ d^2r/dt^2 - \gamma m_o v_\theta^2/r. \tag{7.45}$$

Conservation of energy can be expressed as

$$(\gamma - 1) \ m_c c^2 = \int_{z_o}^{z} dz' \ qE_z = q\varphi. \tag{7.46}$$

The quantity z_o is the location of the source where particles have zero kinetic energy. The absolute electrostatic potential is used. A change in position leads to a change in γ:

$$\Delta\gamma = qE_z\Delta z/m_o c^2.$$

Dividing both sides by Δt and taking the limit of zero interval, we find that

$$d\gamma/dt = qE_z v_z/m_o c^2 = qE_z \beta/m_o c. \tag{7.47}$$

Equations (7.44) and (7.47) are used to replace $d\gamma/dt$ and $d\theta/dt$ in Eq. (7.45).

$$\frac{d^2 r}{dt^2} + \frac{qE_z\beta(dr/dt)}{\gamma m_o c} + \frac{qB_z^2 r}{4\gamma^2 m_o^2} - \frac{q^2\psi_o^2}{4\pi^2\gamma^2 m_o^2}\frac{1}{r^3} - \frac{qE_r}{\gamma m_o} = 0. \tag{7.48}$$

The radial electric field is replaced according to $E_r = (-r/2)(dE_z/dz)$. The derivative is a total derivative since the fields are assumed static and E_z has no first-order radial variation. The final step is to replace all time derivatives with derivatives in z. For instance, it can be easily shown from Eq. (7.47) that $\partial E_z/\partial z = (m_o c^2/q)(d^2\gamma/dz^2)$. The second time derivative of r becomes $v_z^2(d^2 r/dz^2) + v_z(dr/dz)(dv_z/dz)$. When the substitutions are carried out, the paraxial ray equation is obtained.

$$r'' + \frac{\gamma' r'}{\beta^2\gamma} + \left[\frac{\gamma''}{2\beta^2\gamma} + \left(\frac{qB_z}{2\beta\gamma m_o c}\right)^2\right] r - \left(\frac{q\psi_o}{2\pi\beta\gamma m_o c}\right)^2 \frac{1}{r^3} = 0. \tag{7.49}$$

The prime symbol denotes a differentiation with respect to z. The quantities γ, γ', γ'', and B_z are evaluated on the axis. The quantity $\gamma(0, z)$ and its derivatives are related to the electrostatic potential [Eq. (7.46)] which is determined via the Laplace equation.

Consider the final term in Eq. (7.49). The quantity ψ_o is the magnetic flux enclosed by the beam at the source. This is elucidated in Figure 7.11 for an electron beam. The figure shows an immersed cathode located within the magnetic field. When ψ_o is nonzero, the final term in Eq. (7.49) has a strong radial dependence through the $1/r^3$ factor. The term has a dominant defocusing effect when the beam is compressed to a small spot. This is a result of the fact that particles
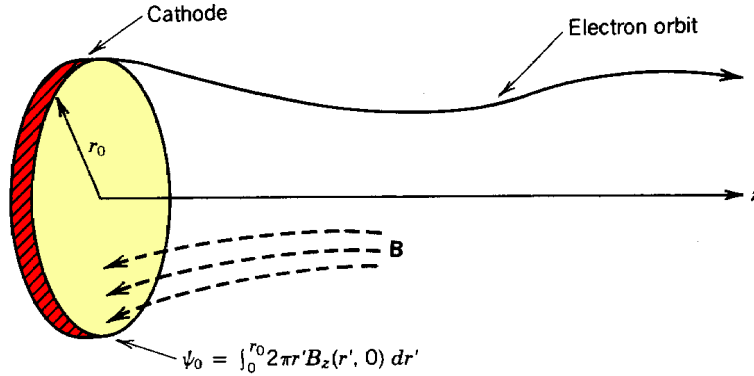

Figure 7.11 Electron emission from an immersed cathode.

produced in a magnetic field have a nonzero canonical angular momentum and are unable to pass through the axis. Thus, care should be taken to exclude magnetic fields from the cathode of the electron source in applications calling for fine focusing. When $\psi_o = 0$, the paraxial ray equation is linear since the remaining terms contain only first powers of r'', r', and r.

The nonrelativistic approximation can be used for beams of ions or low-energy electrons. Substituting $\gamma = 1 - q\varphi/m_oc^2$ in the limit $q\varphi \ll m_oc^2$, Eq. (7.49) becomes

$$2\varphi r'' + \varphi' r' + \left(\frac{\varphi''}{2} + \frac{qB_z^2}{4m_o} \right) - \frac{q\psi_o^2/4\pi^2 m_o}{r^3} = 0. \tag{7.50}$$

If there are only electric fields present, Eq. (7.50) reduces to the familiar form

$$r'' + (\varphi'/2\varphi) \, r' + (\varphi''/4\varphi) \, r = 0. \tag{7.51}$$

where, again, the prime symbol indicates an axial derivative. An alternate form for Eq. (7.51) is

$$\frac{d(r'\varphi)}{dz} + \frac{r^3}{4} \frac{d(\varphi'/r^2)}{dz} = 0. \tag{7.52}$$

7.6 NUMERICAL SOLUTIONS OF PARTICLE ORBITS

The paraxial ray equation is a second-order differential equation that describes a beam envelope or the radial orbit of a particle. It is possible to solve the equation analytically in special field geometries, such as the narrow-diameter aperture lens or the solenoidal lens with sharp field boundaries. In most realistic situations, it is rare to find closed forms for field variations on axis that permit analytic solutions. Thus, numerical methods are used in almost all final designs of charged particle optical systems. In this section, we shall briefly consider a computational method to solve the paraxial ray equation. The method is also applicable to all second-order differential equations, such as the general particle equations of motion.

A second-order differential equation can be written as two first-order equations by treating r' as a variable:

$$(dr/dr) - r' = 0, \qquad (7.53)$$

$$(dr'/dx) - f(r,r',z) = 0, \qquad (7.54)$$

where $f(r, r', z)$ is a general function. For instance, $f = -(\varphi'r'/2\varphi + \varphi''r/4\varphi)$ in Eq. (7.51). Equations (7.53) and (7.54) must be solved simultaneously. In order to illustrate the method of

solution, consider the simpler example of the equation

$$(dr/dz) - f(r,z) = 0. \qquad (7.55)$$

An obvious first approach to solving Eq. (7.55) by finite difference methods would be to approximate the derivative by $(\Delta r/\Delta z)$ to arrive at the algorithm,

$$r(z+\Delta z) \cong r(z) + f(r,z)\,\Delta z. \qquad (7.56)$$

Given an initial condition, $r(z_o)$, the solution $r(z)$ can be determined in steps.
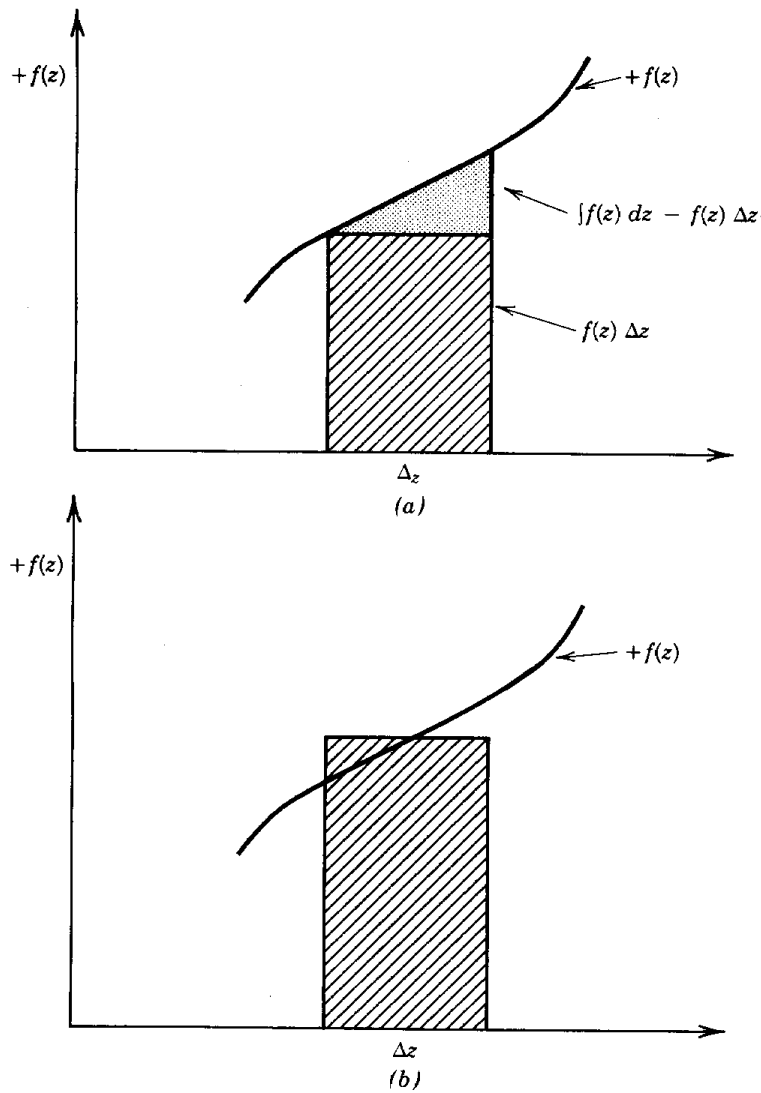

Figure 7.12 Approximations to the integral for the numerical solution of Eq. (7.56). (*a*) Eulerian finite difference method. (*b*) Two-step finite difference method.

The algorithm of Eq. (7.56) is called the *Eulerian difference method*. The drawback of this approach is apparent if we express Eq. (7.55) in integral form.

$$r(z+\Delta z) \, - \, r(z) \; = \; \int_{z}^{z+\Delta z} f(r,z') \; dz'. \tag{7.57}$$

Because we do not know $r(z)$ over the interval Δz, the essence of a finite difference method is to find an estimate of the integral that leads to a good approximation for the continuous function. The estimate of the Eulerian method is $\int f(r, z') \, dz' \cong f(r, z)\Delta z$, as shown in Figure 7.12 a. This introduces a first-order error, so that the final result will be accurate to only order Δz.

  We could get a much better approximation for the integral if we knew the value of $f(r, z)$ at $z + \Delta z/2$. The integral is then approximated as $f(r, z+\Delta z/2)\Delta z$. There is cancellation of first-order errors as shown in Figure 7.12b. The basis of the two-step method is to make an initial estimate of the value of $f(r, z+\Delta z/2)\Delta z$ by the Eulerian method and then to use the value to advance r. The two-step algorithm is

$$\begin{aligned} \textit{Step} \; 1: \qquad & r(z+\Delta z/2) \; \cong \; r(z) \; + \; f(r,z) \; \Delta z/2, \\[2mm] \textit{Step} \; 2: \qquad & r(z+\Delta z) \; \cong \; r(z) \; + \; f(r(z+\Delta z/2),z+\Delta z/2) \; \Delta z. \end{aligned} \tag{7.58}$$

Although this involves two operations to advance r, it saves computation time in the long run because the error between the finite difference approximation and the actual value is of order Δz^2. The two-step method is an example of a *space-centered* (or t*ime-centered*) difference method becuase the integral is estimated symmetrically in the interval. The extension of the algorithm of Eqs. (7.58) to the case of two coupled first-order differential equations [Eqs. (7.53) and (7.54)] is

$$\begin{aligned} \textit{Step} \; 1: \qquad & r(z+\Delta z/2) \; \cong \; r(z) \; + \; r' \; \Delta z/2, \\[2mm] & r'(z+\Delta z/2) \; \cong \; r'(z) \; - \; f[r(z),r'(z),z] \; \Delta z/2. \\[2mm] \textit{Step} \; 2: \qquad & r(z+\Delta z) \; \cong \; r(z) \; + \; r'(z+\Delta z/2) \; \Delta z, \\[2mm] & r'(z+\Delta z) \; \cong \; r'(z) \; - \; f[r(z+\Delta z/2),r'(z+\Delta z/2),z+\Delta z/2) \; \Delta z. \end{aligned} \tag{7.59}$$

The extra work involved in programming a higher-order finite difference scheme is worthwhile even for simple orbit problems. Figure 7.13 shows results for the calculation of a circular orbit described by the equations $(d^2x/dt^2) + y = 0$, $(d^2y/dt^2) - x = 0$. The initial coordinates are $(x = 1, y = 0)$. The relative error in final position $(\Delta x/x)$ after one revolution is plotted as a function of the number of time steps $(\Delta t = 2\pi/n)$. The two-step method achieves 1% accuracy with only 25 steps,
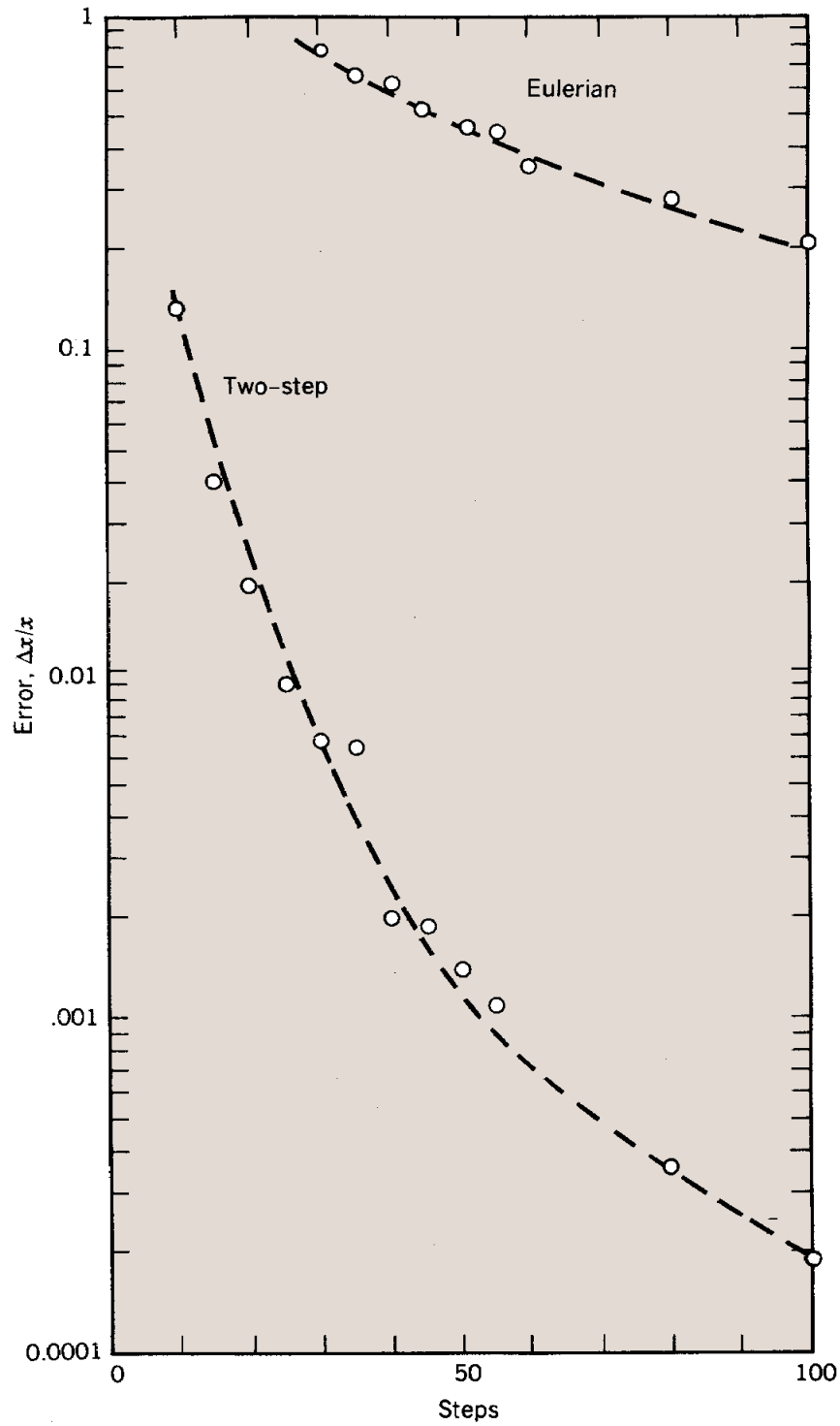
Figure 7.13 Convergence of solutions; Two-step versus Eulerian method. Solutions of equations to generate a circle of unit radius. Difference in radius after one revolution plotted versus number of computational steps per revolution.

while the accuracy of the Eulerian method is no better than 20% after 100 steps.

   As an example of the solution of the paraxial ray equation, consider ion acceleration in an electrostatic acceleration column. The nonrelativistic equation with electric fields only [Eq. (7.51)] can be used. The column, illustrated in Figure 7.14, is found on Van de Graaff accelerators and on electrostatic injectors for high-energy accelerators. A static potential in the range 0.1 to 10 MeV exists between the entrance and the extraction plates. The inside of the column is at high vacuum while the outside is usually immersed in a high-voltage insulating medium such as sulfur hexafluoride gas or transformer oil. A solid vacuum insulator separates the two regions. The insulator has greater immunity to vacuum breakdown if it is separated into a number of short sections by metal grading rings (see Section 9.5). The rings are connected to a high-resistance voltage divider so that the voltage is evenly distributed between the insulator sections. Thick grading rings can also play a role in focusing a beam on the axis of the column.
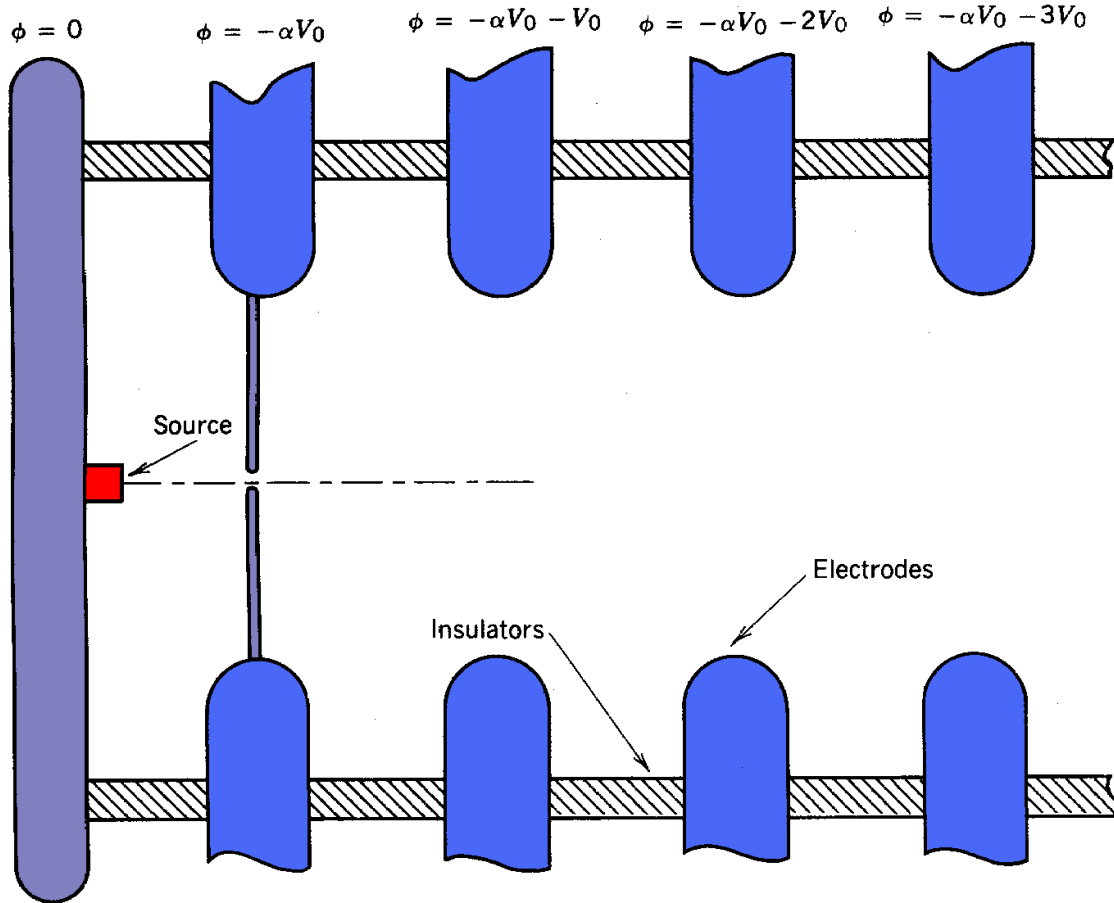

$\phi = 0$ $\phi = -\alpha V_0$ $\phi = -\alpha V_0 - V_0$ $\phi = -\alpha V_0 - 2V_0$ $\phi = -\alpha V_0 - 3V_0$

Figure 7.14   Definition of quantities to determine particle orbits in an electrostatic acceleration column.
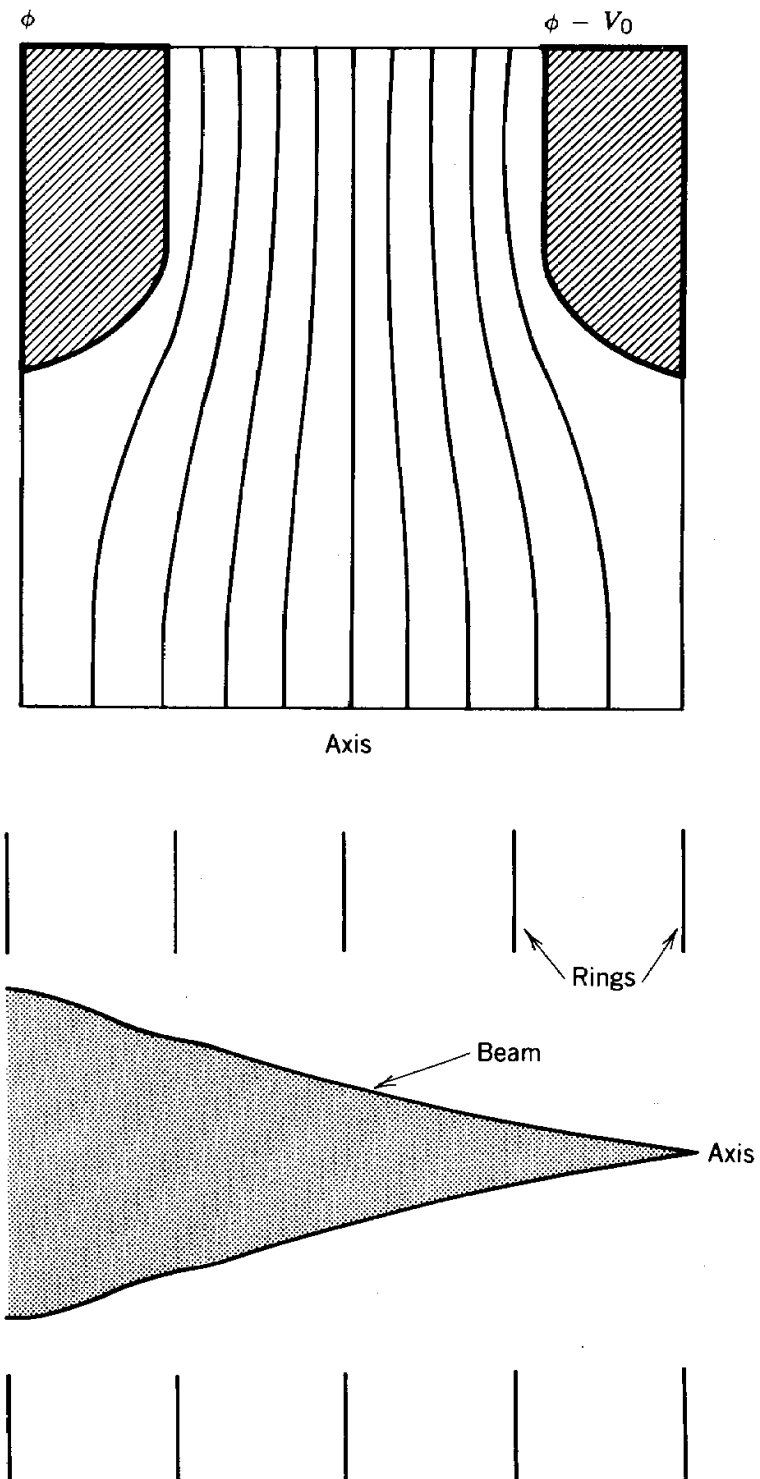
ϕ

$\phi - V_0$

Axis

Rings

Beam

Axis

Figure 7.15 Electrostatic acceleration column. (*a*) Equipotential lines between two grading rings. (*b*) Paraxial ray solution for beam envelope.

Consider, first, the field distribution when the rings are thin. If the thin rings extend to a radius that is large compared to the aperture, then the electric field on the axis is uniform with z. The quantity φ'' is zero; hence the third term in Eq. (7.51) vanishes and there is no radial focusing. The second term in Eq. (7.51) is nonzero, but it does not lead to beam focusing. This term corresponds to the decrease in dr/dz from the increase in v_z with acceleration. In contrast, there are focusing forces when the grading rings are thick. In this case equipotential lines are periodically compressed and expanded along the axis (Fig. 7.15a) leading to radial electric fields.

We express potential relative to the particle source (absolute potential). Assume that ions are injected into the column with energy $q\alpha V_o$, where $-\alpha V_o$ is the absolute potential of the entrance plate. The potential decreases moving down the column (Fig. 7.14). Radial electric field is taken in the form

$$E_r(r,z) \cong - (\beta r/2)\ \sin(2\pi z/d), \tag{7.60}$$

where d is the ring spacing and the origin ($z = 0$) corresponds to the entrance plate. The form of Eq. (7.60) is confirmed by a numerical solution of the Laplace equation (Fig. 7.15a), which also gives the parameter β. The longitudinal electric field is calculated from Eqs. (6.5) and (7.60) as

$$E_Z(r,z) \cong V_o/d - V_o\ (\beta d/2\pi V_o)\ \cos(2\pi z/d), \tag{7.61}$$

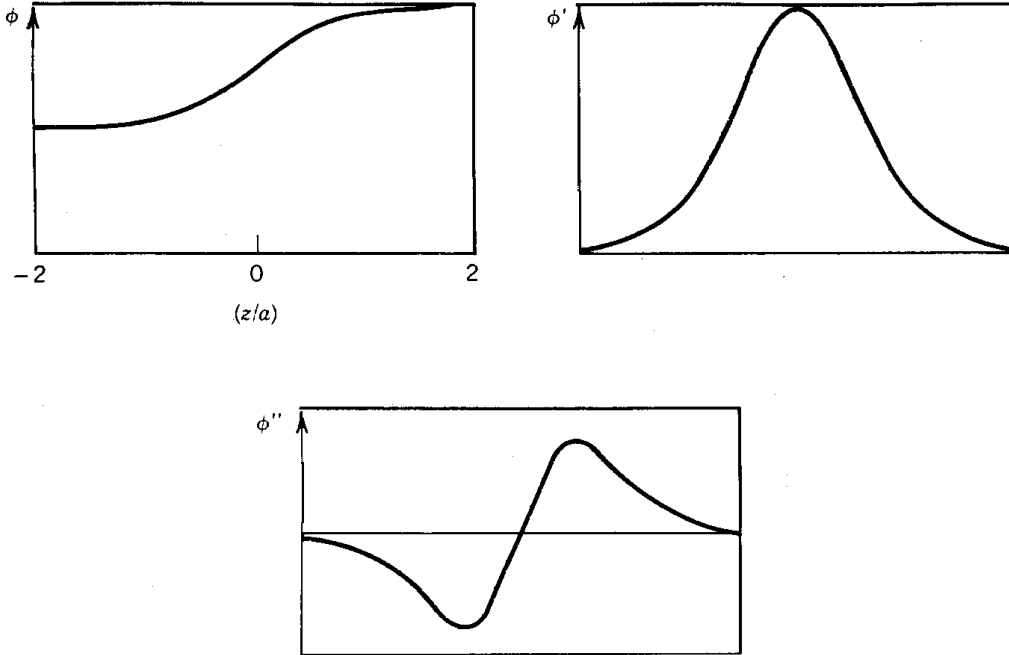where Vo is the voltage between rings. This leads to the following expression and its first two

Figure 7.16 Solutions for axial variation of electrostatic potential (ϕ) and its first two derivatives (ϕ', ϕ'') crossing an immersion lens with tube radius a.

for the absolute potential:

$$\varphi(0,z) \cong V_o \left[-\alpha - z/d + (\beta d^2/4\pi^2) \sin(2\pi z/d) \right]. \tag{7.62}$$

The derivatives φ' and φ'' can be determined from Eq. (7.62).

   Substitution of Eq. (7.62) and its derivatives into Eq. (7.51) leads to the results illustrated in Figure 7.15b for a choice of $\beta = 0.27$ and $\alpha = 1.5$. Note that in the region between the symmetry planes of rings there is a focusing section followed by a defocusing section. The cumulative effect is focusing because the particle gains axial energy and is less affected by positive radial fields on the downstream side.

   As a final application, consider the immersion lens of Section 6.6. The variation of axial potential corresponding to Figure 6.10 is plotted in Figure 7.16. An empirical fit to the potential between two accelerating tubes with a smallgap and radius a is given by [see P. Grivet, **Electron Optics, Vol. I**, translated by P. W. Hawkes, (Pergamon, Oxford, 1972) 208].

$$\varphi(0,z) \cong [\kappa+1] \left[1 + (1-\kappa) \tanh(1.318z/a)/(1+\kappa) \right]/2. \tag{7.63}$$

In Eq. 7.63 a is the tube radius and $\kappa = \varphi_1/\varphi_2$ (where φ_1 is the upstream absolute potential and φ_2 is the downstream potential). Equation (7.63) was used as input to a two-step paraxial ray equation program to obtain the orbits of Figure 6.11. The orbit solutions lead to the thin-lens focal length of Figure 6.12.

8

Transfer Mattices and Periodic Focusing Systems

Periodic focusing channels are used to confine high-energy beams in linear and circular accelerators. Periodic channels consist of a sequence of regions called focusing cells containing one or more charged particle optical elements. A focusing cell is the smallest unit of periodicity in the channel. The main application of periodic channels is in high-energy accelerators that utilize strong focusing. For example, the focusing channel of a linear ion accelerator consists typically of a series of magnetic quadrupole lenses with alternating north-south pole orientation. Thus, along either transverse axis, the lenses are alternately focusing and defocusing. We shall see that such a combination has a net focusing effect that is stronger than a series of solenoid lenses at the same field strength. A quadrupole focusing channel can therefore be constructed with a much smaller bore diameter than a solenoid channel of the same acceptance. The associated reduction in the size and power consumption of focusing magnets has been a key factor in the development of modern high-energy accelerators. Periodic focusing channels also have application at low beam energy. Configurations include the electrostatic accelerator column, the electrostatic Einzel lens array and periodic permanent magnet (PPM) channels used in high-power microwave tubes.

   The transfer matrix description of beam transport in near optical elements facilitates the study of

periodic focusing channels. The matrix description is a mathematical method to organize information about the transverse motions of particles about the main beam axis. Matrices are particularly helpful when dealing with systems with a large number of different elements. The effects on particles of a single element and combinations of elements are described by the familiar rules of matrix algebra. All the lenses and beam bending devices described in Chapter 6 have associated transfer matrices.

The transfer matrices for the focusing and defocusing axes of a quadrupole lens are derived in Section 8.1. Section 8.2 lists transfer matrices for a variety of common optical elements. The rules for combining matrices to describe complex optical systems are reviewed in Section 8.3. The rules are applied in Section 8.4 to the quadrupole doublet and triplet lenses. These lenses combine quadrupole fields to provide focusing along both transverse axes. Periodic systems are introduced by the example of an array of thin one-dimensional lenses separated by drift spaces (Section 8.5). The discussion illustrates the concepts of phase advance and orbital stability. Matrix algebra is used to extend the treatment to general linear focusing systems. Given the transverse matrix for a focusing cell, the stability limits on beam transport can be derived by studying the mathematical properties of the matrix power operation (Section 8.6). The chapter concludes with a detailed look at orbit stability in a long quadrupole channel (Section 8.7).

8.1 TRANSFER MATRIX OF THE QUADRUPOLE LENS

Transfer matrices describe changes in the transverse position and angle of a particle relative to the main beam axis. We assume paraxial motion and linear fields. The axial velocity v_z and the location of the main axis are assumed known by a previous equilibrium calculation. If x and y are the coordinates normal to z, then a particle orbit at some axial position can be represented by the four-dimensional vector (x, x', y, y'). In other words, four quantities specify the particle orbit. The quantities x' and y' are angles with respect to the axis; they are equivalent to transverse velocities if v_z is known. We further assume that the charged particle optical system consists of a number of separable focusing elements. Separable means that boundary planes between the elements can be identified. We seek information on orbit vectors at the boundary planes and do not inquire about details of the orbits within the elements. In this sense, an optical element operates on an entrance orbit vector to generate an output orbit vector. The transfer matrix represents this operation.

Orbits of particles in a magnetic quadrupole lens were discussed in Section 6.10. The same equations describe the electric quadrupole with a correct choice of transverse axes and the replacement $\kappa_m \Rightarrow \kappa_e$. In the following discussion, κ can represent either type of lens. According to Eqs. (6.31) and (6.32), motions in the x and y directions are separable. Orbits can therefore be represented by two independent two-dimensional vectors, $\mathbf{u} = (x, x')$ and $\mathbf{v} = (y, y')$. This separation holds for other useful optical elements, such as the magnetic sector field (Section 6.8) and the focusing edge (Section 6.9). We shall concentrate initially on analyses of orbits along one coordinate. Orbit vectors have two components and transfer matrices have dimensions 2×2.

Consider motion in the x direction in a quadrupole lens oriented as shown in Figure 5.16. The

lens is focusing in the x direction. If the lens has a length l, the exit parameters are related to the entrance parameters by

$$x_f = x_i \cos(\sqrt{\kappa}l) + x_i' \sin(\sqrt{\kappa}l)/\sqrt{\kappa}, \qquad (8.1)$$

$$x_f' = -x_i \sqrt{\kappa} \sin(\sqrt{\kappa}l) + x_i' \cos(\sqrt{\kappa}l). \qquad (8.2)$$

The lens converts the orbit vector $\boldsymbol{u}_i = (x_i, x_i')$ into the vector $\boldsymbol{u}_f = (x_f, x_f')$. The components of $\boldsymbol{u}_f$ are linear combinations of the components of $\boldsymbol{u}_i$. The operation can be written in matrix notation as

$$\boldsymbol{u}_f = \boldsymbol{A}_F \, \boldsymbol{u}_i, \qquad (8.3)$$

if $\boldsymbol{A}_F$ is taken as

$$\boldsymbol{A}_F = \begin{bmatrix} \cos(\sqrt{\kappa}l) & \sin(\sqrt{\kappa}l)/\sqrt{\kappa} \\ -\sqrt{\kappa}\sin(\sqrt{\kappa}l) & \cos(\sqrt{\kappa}l) \end{bmatrix}, \qquad (8.4)$$

where the subscript F denotes the focusing direction. For review, the rule for multiplication of a 2 × 2 matrix times a vector is

$$\begin{bmatrix} a_{11} & a_{12} \\ a_{21} & a_{22} \end{bmatrix} \begin{pmatrix} x \\ x' \end{pmatrix} = \begin{pmatrix} a_{11}x + a_{12}x' \\ a_{21}x + a_{22}x' \end{pmatrix}. \qquad (8.5)$$

If the poles in Figure 5.16 are rotated 90°, the lens defocuses in the x direction. The transfer matrix in this case is

$$\boldsymbol{A}_D = \begin{bmatrix} \cosh(\sqrt{\kappa}l) & \sinh(\sqrt{\kappa}l)/\sqrt{\kappa} \\ \sqrt{\kappa}\sinh(\sqrt{\kappa}l) & \cosh(\sqrt{\kappa}l) \end{bmatrix}, \qquad (8.6)$$

Quadrupole lenses are usually used in the limit $\sqrt{\kappa}\, l \le 1$. In this case, the trigonometric and hyperbolic functions of Eqs. (8.4) and (8.6) can be expanded in a power series. For reference, the power series forms for the transfer matrices are

$$\boldsymbol{A}_F = \begin{bmatrix} 1-\Gamma^2/2+\Gamma^4/24+... & (\Gamma-\Gamma^3/6+...)/\sqrt{\kappa} \\ -\sqrt{\kappa}(\Gamma-\Gamma^3/6+...) & 1-\Gamma^2/2+\Gamma^4/24+... \end{bmatrix}, \qquad (8.7)$$

and

$$A_D = \begin{bmatrix} 1 + \Gamma^2/2 + \Gamma^4/24 + ... & (\Gamma + \Gamma^3/6 + ...)/\sqrt{\kappa} \\ \sqrt{\kappa}(\Gamma + \Gamma^3/6 + ...) & 1 + \Gamma^2/2 + \Gamma^4/24 + ... \end{bmatrix},$$ (8.8)

where $\Gamma = \sqrt{\kappa}l$. The example of the quadrupole illustrates the method for finding the transfer matrix for a linear optical element. Numerical or analytic orbit calculations lead to the identification of the four matrix components. The transfer matrix contains complete information on the properties of the lens as an orbit operator.

When the action of a focusing system is not decoupled in x and y, the full four-dimensional vector must be used and the transfer matrices have the form

$$\begin{bmatrix} \blacksquare & \blacksquare & \square & \square \\ \blacksquare & \blacksquare & \square & \square \\ \square & \square & \blacksquare & \blacksquare \\ \square & \square & \blacksquare & \blacksquare \end{bmatrix}.$$

A focusing system consisting of quadrupole lenses mixed with axisymmetric elements (such as solenoid lens) has coupling of x and y motions. The transfer matrix for this system has coupling components represented by the open boxes above. Sometimes, in the design of particle spectrometers (where beam energy spread is of prime concern), an extra dimension is added to the orbit vector to represent chromaticity, or the variations of orbit parameters with energy [see P. Dahl, **Introduction to Electron and Ion Optics** (Academic Press, New York, 1973) Chapter 2] In this case, the orbit vector is represented as $\boldsymbol{u} = (x, x', y, y', T)$.

8 .2 TRANSFER MATRICES FOR COMMON OPTICAL ELEMENTS

The following examples illustrate the concept of ray transfer matrices and indicate how they are derived. The simplest case is the thin one-dimensional lens, illustrated in Figure 8.1. Only the angle of the orbit changes when a particle passes through the lens. Following Section 6.4, the transformation of orbit variables is

$$x_f = x_i,$$
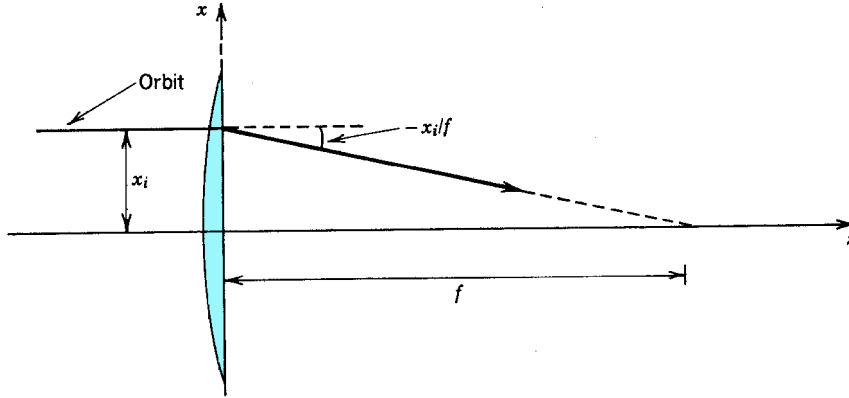
$$x_f' - x_i' - x/f,$$ (8.9)

168

Figure 8.1 Effect of a thin lens (focal length f) on a particle orbit initially parallel to the axis.

where f is the focal length. This can be written in the form of Eq. (8.3) with the transfer matrix,

$$A = \begin{bmatrix} 1 & 0 \\ -1/f & 1) \end{bmatrix}. \tag{8.11}$$

The matrix for a diverging lens is the same except for the term a_{21} which equals $+1/f$. In general, the sign of a_{21} indicates whether the optical element (or combination of elements) is focusing or defocusing.

An optical element is defined as any region in a focusing system that operates on an orbit vector to change the orbit parameters. Thus, there is a transfer matrix associated with translation in field-free space along the z axis (Fig. 8.2). In this case, the distance from the axis changes according to $x_f = x_i + x_i'd$, where d is the length of the drift space. The angle is unchanged. The transfer matrix is

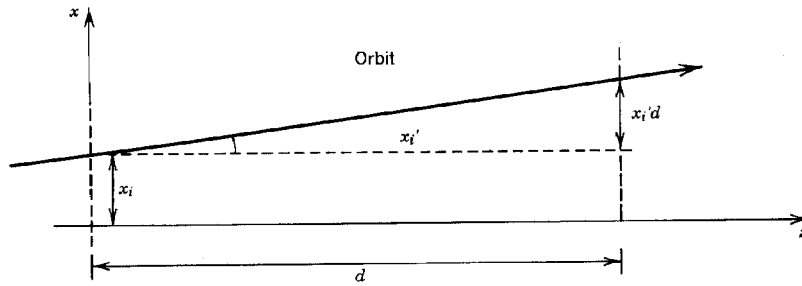$$A = \begin{bmatrix} 1 & d \\ 0 & 1) \end{bmatrix}. \tag{8.12}$$

Figure 8.2 Modification of a particle orbit passing through a drift region of length d.

Transfer Matrices and Periodic Focusing Systems

We have already studied the magnetic sector lens with uniform field (Section 6.8). A gradient can be added to the sector field to change the focal properties by varying the width of the gap, as shown in Figure 8.3. Consider the following special case. The magnet has boundaries perpendicular to the main orbit so that there is no edge focusing. Furthermore, the field gradient is parallel to the radius of curvature of the main orbit. With these assumptions, the sector field of Figure 8.3 is a pie-shaped segment of the betatron field studied in Section 7.3. The field variation near the main radius is characterized by the field index n_o [Eq. (7.18)]. Motions about the main axis in the horizontal and vertical direction are decoupled and are described by independent 2×2 matrices. Applying Eq. (7.30), motion in the horizontal plane is given by

$$x = A \cos[\sqrt{1-n_o}\ (z/r_g) + \varphi],\qquad(8.12)$$

$$x = dx/dz = -[\sqrt{1-n_o}/r_g]\ A\ \sin[\sqrt{1-n_o}\ (z/r_g) + \varphi].\qquad(8.13)$$

The initial position and angle are related to the amplitude and phase by $x_i = A\cos\varphi$ and $x_i' = -\sqrt{1-n_o}\ A\ \sin\varphi/r_g$. In order to determine the net effect of a sector (with transit distance $-d = \alpha r_g$) on horizontal motion, we consider two special input vectors, $(x_i, 0)$ and $(0, x_i')$. In the first case $\varphi = 0$ and in the second $\varphi = \pi/2$. According to Eqs. (8.12) and (8.13), the final orbit parameters for a particle entering parallel to the main axis are

$$x_f = x_i \cos(\sqrt{1-n_o}\ d\ /\ r_g),\qquad(8.14)$$

and

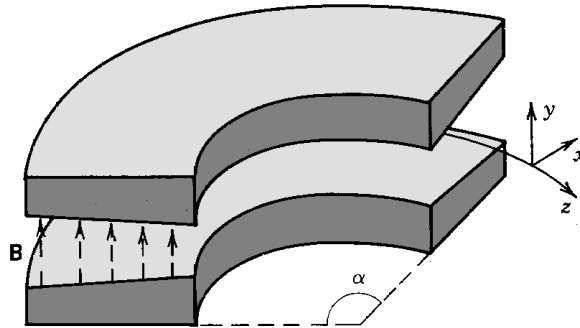$$x_f' = -x_i\ (\sqrt{1-n_o}/r_g)\ \sin(\sqrt{1-n_o}\ d\ /\ r_g),\qquad(8.15)$$

Figure 8.3 Sector magnet of angular extent α with a negative field gradient along the radius of curvature of the main particle orbit.

Similarly, if the particle enters on the main axis at an angle, the final orbit parameters are

$$x_f = x_i' \, r_g \, \sin(\sqrt{1-n_o} \, d \, / \, r_g) \, / \, \sqrt{1-n_o} \, , \tag{8.16}$$

and

$$x_f' = x_i' \, \cos(\sqrt{1-n_o} \, d \, / \, r_g). \tag{8.17}$$

The factor d/r_g is equal to α, the angle subtended by the sector. Combining the results of Eqs. (8.14)-(8.17), the transfer matrix is

$$A_H = \begin{bmatrix} \cos(\sqrt{1-n_o} \, \alpha) & r_g \sin(\sqrt{1-n_o} \, \alpha)/\sqrt{1-n_o} \\ -\sqrt{1-n_o} \, \sin(\sqrt{1-n_o} \, \alpha)/r_g & \cos(\sqrt{1-n_o} \, \alpha) \end{bmatrix}. \tag{8.18}$$

Similarly, for the vertical direction,

$$A_V = \begin{bmatrix} \cos(\sqrt{n_o} \, \alpha) & r_g \sin(\sqrt{n_o} \, \alpha)/\sqrt{n_o} \\ -\sqrt{n_o} \, \sin(\sqrt{n_o} \, \alpha)/r_g & \cos(\sqrt{n_o} \, \alpha) \end{bmatrix}. \tag{8.19}$$

Following the development of Section 6.8, initially parallel beams are focused in the horizontal direction. The focal point is located a distance

$$f' = r_g/\tan(\sqrt{1-n_o} \, \alpha) \tag{8.20}$$

beyond the sector exit. This should be compared to Eq. (6.27). When n_o is negative (a positive field gradient moving out along the radius of curvature), horizontal focusing is strengthened. Conversely, a positive field index decreases the horizontal focusing. There is also vertical focusing when the field index is positive. The distance to the vertical focal point is

$$f' = r_g/\tan(\sqrt{n_o} \, \alpha) \tag{8.21}$$

If $n_o = +0.5$, horizontal and vertical focal lengths are equal and the sector lens can produce a two-dimensional image. The dual-focusing property of the gradient field is used in charged particle spectrometers.

Particles may travel in either direction through a sector magnet field, so there are two transfer

matrices for the device. The matrix for negatively directed particles can be calculated directly. The transfer matrix for particles moving backward in the sector field is the *inverse* of the matrix for forward motion. The inverse of a 2×2 matrix

$$A = \begin{bmatrix} a_{11} & a_{12} \\ a_{21} & a_{22} \end{bmatrix}$$

is

$$A = \frac{1}{\det A} \begin{bmatrix} a_{22} & -a_{12} \\ -a_{21} & a_{11} \end{bmatrix}. \tag{8.22}$$

The quantity $\det A$ is the determinant of the matrix A, defined by

$$\det A = a_{11}a_{22} - a_{12}a_{21}. \tag{8.23}$$

The determinant of the sector field transfer matrix in the horizontal direction is equal to 1. The inverse is

$$A_H^{-1} = \begin{bmatrix} \cos(\sqrt{1-n_o}\ \alpha) & -r_g \sin(\sqrt{1-n_o}\ \alpha)/\sqrt{1-n_o} \\ \sqrt{1-n_o}\ \sin(\sqrt{1-n_o}\ \alpha)/r_g & \cos(\sqrt{1-n_o}\ \alpha) \end{bmatrix}. \tag{8.24}$$

Equation (8.24) is equal to Eq. (8.18) with the replacement $\alpha \Rightarrow -\alpha$. The negative angle corresponds to motion in the $-z$ direction. The effect of the element is independent of the direction. The same holds true for any optical element in which the energy of the charged particle is unchanged. We can verify that in this case $\det A = 1$.

Acceleration gaps in linear accelerators have the geometry of the immersion lens (Figure 6.10). This lens does not have the same focal properties for particle motion in different directions. Assume the focal length for motion of nonrelativistic particles in the accelerating direction, f_a, is known. This is a function of the lens geometry as well as the absolute potentials of each of the tubes. The upstream potential is φ_1 while the downstream potential is φ_2. The quantity ξ is defined as the ratio of the exit velocity to the entrance velocity and is equal to $\xi = \sqrt{\varphi_2/\varphi_1}$. In the thin-lens approximation, a particle's position is constant but the transverse angle is changed. If the particle entered parallel to the axis in the accelerating direction, it would emerge at an angle $-x_i/f_a$. Similarly, a particle with an entrance vector $(0, x_i')$ emerges at an angle x_i'/ξ. The traverse velocity is the same, but the longitudinal velocity increases. The general form for the transfer matrix of a thin electrostatic lens with acceleration is
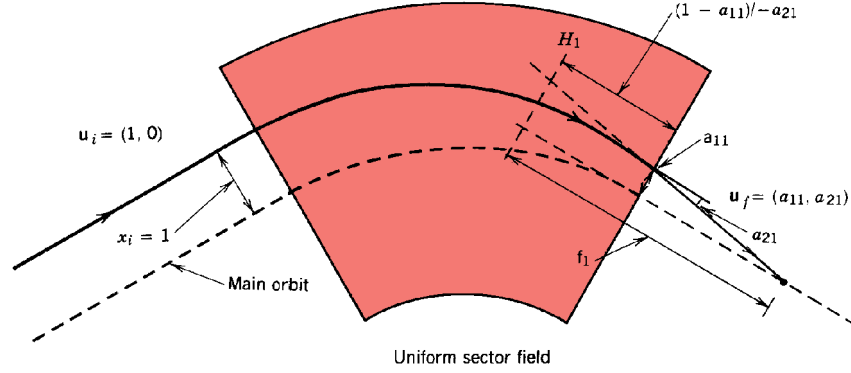
Figure 8.4 Horizontal particle motion in a uniform-field sector magnet. Relationship between the elements of the transfer matrix and the principal planes and focal lengths of Gaussian optics.

$$A = \begin{bmatrix} 1 & 0 \\ -1/f_a & 1/\xi \end{bmatrix}.$$ (8.25)

The determinant has the value $\det A = 1/\xi \neq 1$. The transfer matrix for a decelerating lens is the inverse of A. Applying Eq. (8.22) and inverting signs so that the particle travels in the $+z$ direction,

$$A = \begin{bmatrix} 1 & 0 \\ -\xi/f_a & \xi \end{bmatrix}.$$ (8.26)

In the thin-lens limit, the accelerating and decelerating focal lengths are related by $f_d = f_a/\xi$.

To conclude the discussion of transfer matrices, we consider how the four components of transfer matrices are related to the focal lengths and principal planes of Gaussian optics (Chapter 6). Consider the uniform sector field of Figure 8.4. This acts as a thick lens with a curved main axis. An orbit vector *(1, 0)* is incident from the left. The relationship between the emerging orbit and the matrix components as well as the focal length and principal plane H_1 are indicated on the figure. Applying the law of similar triangles, the focal length is given by $f_1 = -1/a_{11}$. The principal plane is located a distance $z_1 = (1 - a_{11})/a_{21}$ from the boundary. Thus, the components a_{11} and a_{21} are related to f_1 and H_1. When the matrix is inverted, the components a_{12} and a_{22} move to the first column. They are related to f_2 and H_2 for particles traveling from right to left. The matrix and Gaussian descriptions of linear lenses are equivalent. Lens properties are completely determined by four quantities.

8.3 COMBINING OPTICAL ELEMENTS

Matrix algebra makes it relatively easy to find the cumulative effect of a series of transport devices. A single optical element operates on an entrance orbit vector, u_0, changing it to an exit vector, u_1. This vector may be the entrance vector to another element, which subsequently changes it to u_2. By the superposition property of linear systems, the combined action of the two elements can be represented by a single matrix that transforms u_0 directly to u_2.

   If A is the transfer matrix for the first element and B for the second, the process can be written symbolically,

$$u_1 = A\ u_0, \qquad u_2 = B\ u_1 = B\ (A\ u_0),$$

$$or$$

$$u_2 = C\ u_0.$$

The matrix C is a function of A and B. The functional dependence is called *matrix multiplication* and is denoted $C = BA$. The rule for multiplication of two 2×2 matrices is

$$C = \begin{bmatrix} c_{11} & c_{12} \\ c_{21} & c_{22} \end{bmatrix} = \begin{bmatrix} b_{11} & b_{12} \\ b_{21} & b_{22} \end{bmatrix} \begin{bmatrix} a_{11} & a_{12} \\ a_{21} & a_{22} \end{bmatrix}, \tag{8.27}$$

where

$$c_{11} = b_{11}a_{11} + b_{12}a_{21}, \qquad c_{12} = b_{11}a_{12} + b_{12}a_{22},$$

$$c_{21} = b_{21}a_{11} + b_{22}a_{21}, \qquad c_{22} = b_{21}a_{21} + b_{22}a_{22}.$$

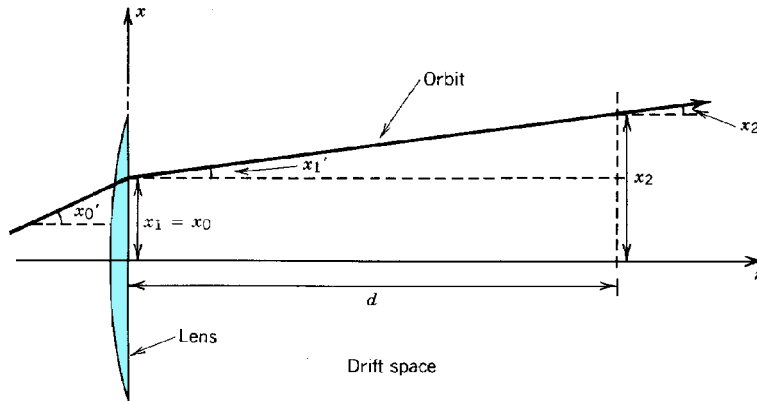We shall verify the validity of Eq. (8.27) for the example illustrated in Figure 8.5. The optical

Figure 8.5 Orbit of a particle passing through a thin lens of focal length f and along a drift distance d.

174

system consists of two one-dimensional elements, a thin lens with focal length f followed by a drift space d. The particle entrance orbit is (x_0, x_0'). The position and angle emerging from the lens are $x_1 = x_0$ and $x_1' = x_0' - x_0/f$. Traveling through the drift space, the orbit angle remains constant but the displacement changes by an amount $\Delta x = x_1'd$. The total transformation is

$$x_2 = x_0 + (x_0' - x_0/f)\, d = x_0\, (1 - d/f) = x_0' d, \tag{8.28}$$

$$x_2' = x_0' - x_0/f. \tag{8.29}$$

Inspection of Eqs. (8.28) and (8.29) yields the 2×2 transformation matrix,

$$\mathbf{C} = \begin{bmatrix} 1-d/f & d \\ -1/f & 1 \end{bmatrix} = \begin{bmatrix} 1 & d \\ 0 & 1 \end{bmatrix} \begin{bmatrix} 1 & 0 \\ -1/f & 1 \end{bmatrix}. \tag{8.30}$$

We can easily verify that $\mathbf{C}$ is the matrix product of Eq. (8.11) by Eq. (8.10).

It is important to note that the mathematic order of matrix multiplication must replicate the geometric order in which the elements are encountered. Matrix multiplication is not commutative, so that $\mathbf{AB} \neq \mathbf{BA}$. The inequality can be demonstrated by calculating the transfer matrix for a drift space followed by a lens. The effect of this combination is not the same as a lens followed by a drift space. Consider a parallel orbit entering the two systems. In the drift-lens geometry, the particle emerges at the same position it entered. In the second combination, the final position will be different. Multiplying transfer matrices in the improper order is a frequent source of error. To reiterate, if a particle travels in sequence through elements represented by $\mathbf{A}_1$, $\mathbf{A}_2$, ... , $\mathbf{A}_{n-1}$, $\mathbf{A}_n$, then the combination of these elements is a matrix given by

$$\mathbf{C} = \mathbf{A}_n\, \mathbf{A}_{n-1}\, ...\, \mathbf{A}_2\, \mathbf{A}_1. \tag{8.31}$$

The astigmatic focusing property of quadrupole doublets (Section 8.4) is an important consequence of the noncommutative property of matrix multiplication.

We can use matrix algebra to investigate the imaging property of a one-dimensional thin lens. The proof that a thin lens can form an image has been deferred from Section 6.4. The optical system consists of a drift space of length d_2, a lens with focal length f and another drift space d_1 (see Fig. 6.7). The vectors (x_0, x_0') and (x_3, x_3') represent the orbits in the planes σ_1 and σ_2. The planes are object and image planes if all rays that leave a point in σ_1 pass through a corresponding point in σ_2, regardless of the orbit angle. An equivalent statement is that x_3 is a function of x_0 with no dependence on x_0'. The transfer matrix for the system is

$$C = \begin{bmatrix} 1 & d_1 \\ 0 & 1 \end{bmatrix} \begin{bmatrix} 1 & 0 \\ -1/f & 1 \end{bmatrix} \begin{bmatrix} 1 & d_2 \\ 0 & 1 \end{bmatrix}$$

$$= \begin{bmatrix} 1 - d_1/f & d_1 + d_2 - d_1 d_2/f \\ -1/f & 1 - d_2/f \end{bmatrix}.$$

(8.32)

The position of the output vector in component form is $x_3 = c_{11} x_0 + c_{12} x_0'$. An image is formed if $c_{12} = 0$. This is equivalent to $1/f = (1/d_1) + (1/d_2)$. This is the thin-lens formula of Eq. (6.15). When the image condition holds, $M = x_2/x_1 = c_{11}$.

8.4 QUADRUPOLE DOUBLET AND TRIPLET LENSES

A quadrupole lens focuses in one coordinate direction and defocuses in the other. A single lens cannot be used to focus a beam to a point or to produce a two-dimensional image. Two-dimensional focusing can be accomplished with combinations of quadrupole lenses. We will study the focal properties of two (doublets) and three quadrupole lenses (triplets). Quadrupole lens combinations form the basis for most high-energy particle transport systems. They occur as extended arrays or as discrete lenses for final focus to a target. Quadrupole lens combinations are convenient to describe since transverse motions are separable in x and y if the poles (electrodes) are aligned with the axes as shown in Figures 4.14 (for the electrostatic lens) and 5.16 (for the magnetic lens). A 2×2 matrix analysis can be applied to each direction.

The magnetic quadrupole doublet is illustrated in Figure 8.6. We shall consider identical lenses in close proximity, neglecting the effects of gaps and edge fields. It is not difficult to extend the treatment to a geometry with a drift space between the quadrupoles. Relative to the x direction,
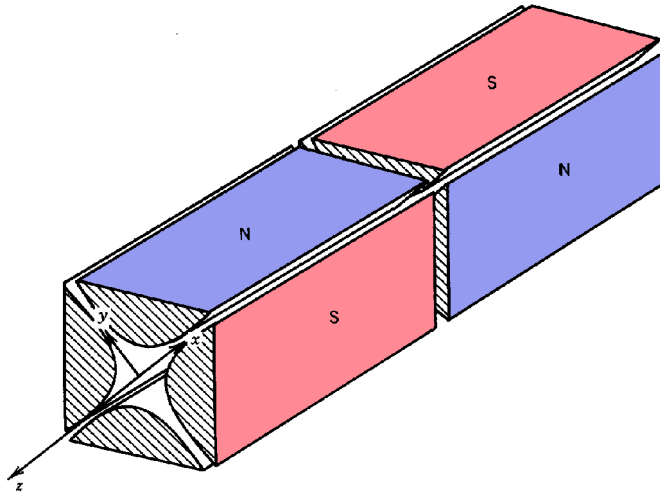

Figure 8.6   Magnetic quadrupole doublet lens.

the first element is focusing and the second is defocusing. This is represented symbolically as

F	D

where particles move from left to right. Conversely, in the y direction the doublet is denoted

D	F

The transfer matrices for the combination of the two elements can be found by matrix multiplication of Eqs. (8.4) and (8.6). The multiplication must be performed in the proper order. The result for an *FD* channel is

$$C_{FD} = \begin{bmatrix} \cos\Gamma\cosh\Gamma - \sin\Gamma\sinh\Gamma & (\cosh\Gamma\sin\Gamma + \cos\Gamma\sinh\Gamma)/\sqrt{\kappa} \\ \sqrt{\kappa}(\cos\Gamma\sinh\Gamma - \cosh\Gamma\sin\Gamma) & \cos\Gamma\cosh\Gamma + \sin\Gamma\sinh\Gamma \end{bmatrix}. \tag{8.33}$$

where $\Gamma = \sqrt{\kappa}l$. Similarly, for a *DF* channel,

$$C_{DF} = \begin{bmatrix} \cos\Gamma\cosh\Gamma + \sin\Gamma\sinh\Gamma & (\cosh\Gamma\sin\Gamma + \cos\Gamma\sinh\Gamma)/\sqrt{\kappa} \\ \sqrt{\kappa}(\cos\Gamma\sinh\Gamma - \cosh\Gamma\sin\Gamma) & \cos\Gamma\cosh\Gamma - \sin\Gamma\sinh\Gamma \end{bmatrix}. \tag{8.34}$$

Equations (8.33) and (8.34) have two main implications. First, the combination of equal defocusing and focusing elements leads to net focusing, and, second, focusing is different in the *x* and *y* directions. As we found in the previous section, the term c_{21} of the transfer matrix determines whether the lens is focusing or defocusing. In this case, $c_{21} = \sqrt{\kappa}\ (\cos\sqrt{\kappa}l\sinh\sqrt{\kappa}l - \cosh\sqrt{\kappa}l\sin\sqrt{\kappa}l)$. We can verify by direct computation that $c_{21} = 0$ at $\sqrt{\kappa}l = 0$ and it is a monotonically decreasing function for all positive values of $\sqrt{\kappa}l$. The reason for this is illustrated in Figure 8.7, which shows orbits in the quadrupoles for the *FD* and *DF* directions. In both cases, the orbit displacement is larger in the focusing section than in the defocusing section; therefore, the focusing action is stronger. Figure 8.7 also shows that the focal points in the *x* and *y* directions are not equal. An initially parallel beam is compressed to a line rather than a point in the image planes. A lens with this property is called *astigmatic*. The term comes from the Latin word *stigma*, meaning a small mark. A lens that focuses equally in both directions can focus to a point or produce a two-dimensional image. Such a lens is called *stigmatic*. The term anastigmatic is also used. Astigmatism in the doublet arises from the displacement term c_{11}. Although initially parallel orbits emerge from *FD* and *DF* doublets with the
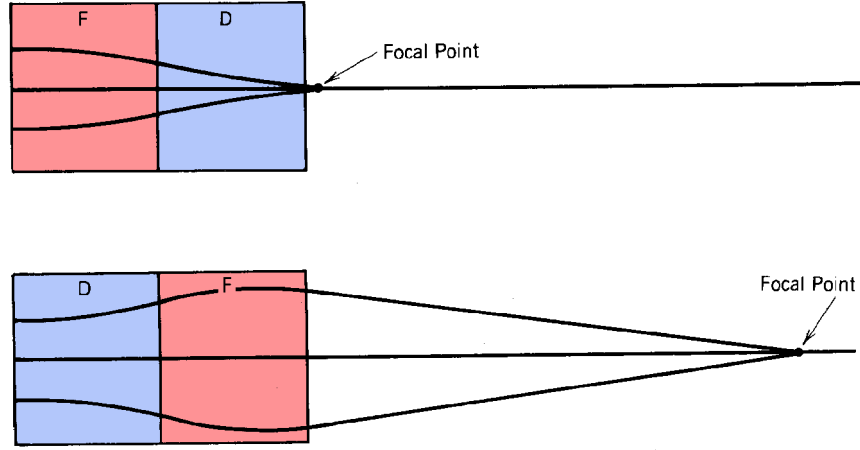
Figure 8.7 Astigmatism in a doublet lens. Orbits of particles initially parallel to the axis projected in the x and y planes.

same angle, the displacement is increased in the *DF* combination, and decreased in the *FD*.

The transfer matrix for a three-element optical system consisting of a drift space of length $l/2$, a thin lens with focal length f, and another drift space is

$$A = \begin{bmatrix} 1-l/2f & l-l^2/4f \\ -1/f & 1-l/2f \end{bmatrix}. \tag{8.35}$$

Comparison of Eq. (8.35) with Eqs. (8.7) and (8.8) shows a correspondence if we take $f = \pm 1/\kappa l$. Thus, to order $(\sqrt{\kappa}l)^2$, quadrupole elements can be replaced by a drift space of length l with a thin lens at the center. This construction often helps to visualize the effect of a series of quadrupole lenses. A similar power series approximation can be found for the total ray transfer matrix of a doublet. Combining Eqs. (8.7) and (8.8) by matrix multiplication

$$C_{DF} = \begin{bmatrix} 1+\kappa l^2 & 2l \\ -2\kappa^2 l^3/3 & 1-\kappa l^2 \end{bmatrix}. \tag{8.36}$$

$$C_{FD} = \begin{bmatrix} 1-\kappa l^2 & 2l \\ -2\kappa^2 l^3/3 & 1+\kappa l^2 \end{bmatrix}. \tag{8.37}$$

Equations (8.36) and (8.37) are correct to order $(\sqrt{\kappa}l)^4$.

Stigmatism can be achieved with quadrupoles in a configuration called the triplet. This consists of three quadrupole sections. The entrance and exit sections have the same length ($l/2$) and pole orientation, while the middle section is rotated $90°$ and has length l. Orbits in the x and y planes of
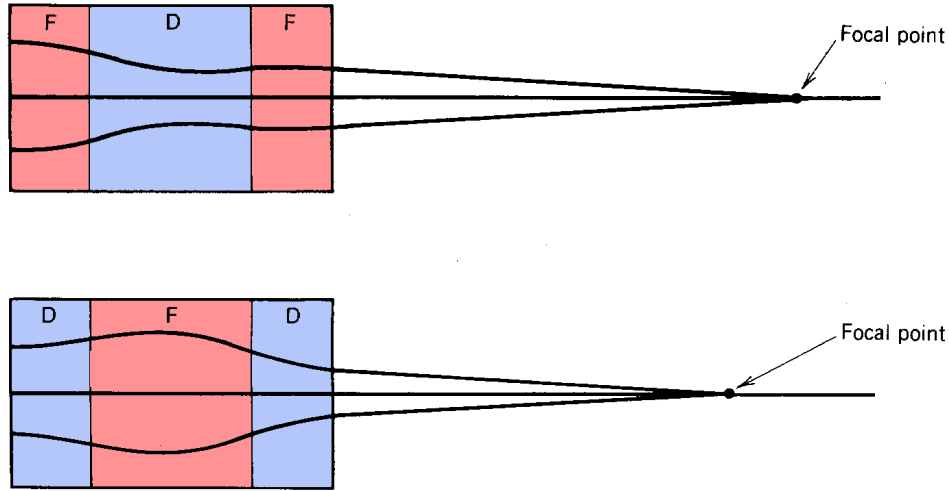
Figure 8.8   Improved stigmatic properties of a quadrupole triplet lens. Orbits of particles initially parallel to the axis projected in the x and y planes.

the triplet are illustrated in Figure 8.8. An exact treatment (using the trigonometric-hyperbolic forms of the transfer matrices) shows that the exit displacements are identical in both planes for equal entrance displacements. The power series expansions [Eqs. (8.7) and (8.8)] can be used to show that the exit angles are approximately equal. When the calculation is carried out, it is found that all terms of order $(\sqrt{\kappa}l)^2$ mutually cancel from the total matrix. The following result holds for both the *FDF* and *DFD* combinations:

$$C_{triplet} = \begin{bmatrix} 1 & 2l \\ -\kappa^2 l^3/6 & 1 \end{bmatrix}. \tag{8.38}$$

Equation (8.38) is accurate to order $(\sqrt{\kappa}l)^4$.

8.5 FOCUSING IN A THIN-LENS ARRAY

As an introduction to periodic focusing, we shall study the thin-lens array illustrated in Figure 8.9. Orbits in this geometry can be determined easily. The focusing cell boundaries can have any location as long as they define a periodic collection of identical elements. We will take the boundary at the exit of a lens. A focusing cell consists of a drift space followed by a lens, as shown in Figure 8.9.

The goal is to determine the positions and angles of particle orbits at cell boundaries. The following equations describe the evolution of the orbit parameters traveling through the focusing cell labeled *(n+1)* in the series [see Eqs. (8.10) and (8.11)]. The subscript n denotes the orbit
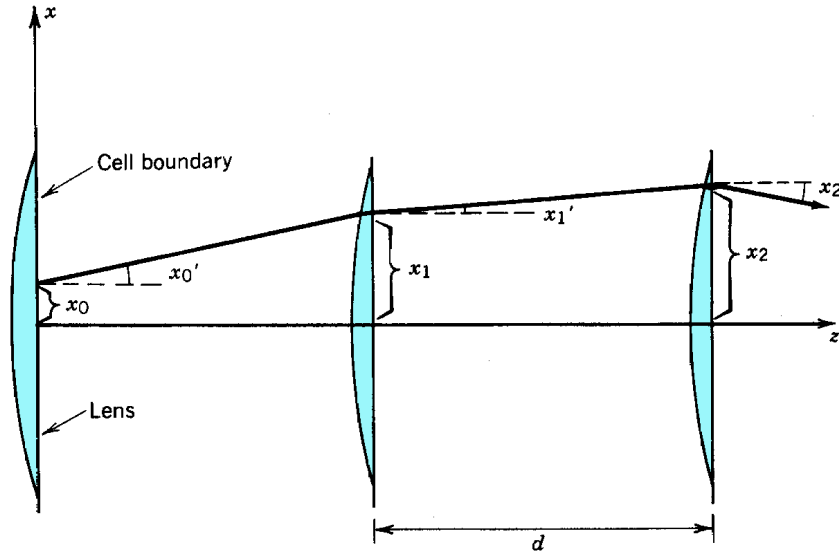
179

Figure 8.9 Particle orbit in first three cells of a uniform thin-lens array.

parameter at the exit of the *nth* focusing cell:

$$x_{n+1} = x_n + dx_n', \qquad (8.39)$$

$$x_{n+1}' = x_n' - x_{n+1}/f. \qquad (8.39)$$

Equation (8.39) can be solved for x_n'

$$x_n' = (x_{n+1} - x_n)/d. \qquad (8.41)$$

Equation (8.41) can be substituted in Eq. (8.40) to yield

$$x_{n+1}' = [(1 - d/f) x_{n+1} - x_n]/d. \qquad (8.42)$$

Finally, an equation similar to Eq. (8.41) can be written for the transition through focusing cell *(n+2)*

$$x_{n+1}' = (x_{n+2} - x_{n+1})/d. \qquad (8.43)$$

Setting Eqs. (8.42) and (8.43) equal gives the difference equation

180

$$x_{n+2} - 2 (1-d/2f) x_{n+1} + x_n = 0. \tag{8.44}$$

This is the finite difference equivalent of a second-order differential equation. We found in Section 4.2 that the finite difference approximation to the second derivative of a function involves the values of the function at three adjacent mesh points.

We seek a mathematical solution of Eq. (8.44) in the form

$$x_n = x_o \exp(jn\mu). \tag{8.45}$$

Defining $b = 1 - d/2f$ and substituting in Eq. (8.44),

$$\exp[j(n+2)\mu] - 2b \exp[j(n+1)\mu] + \exp(jn\mu) = 0, \quad or$$

$$\exp(2j\mu) - 2b \exp(j\mu) + 1 = 0. \tag{8.46}$$

Applying the quadratic formula, the solution of Eq. (8.46) is

$$\exp(j\mu) = b \pm j \sqrt{1-b^2}. \tag{8.47}$$

The complex exponential can be rewritten as

$$\exp(j\mu) = \cos\mu + j \sin\mu = \cos\mu + j \sqrt{1-\cos^2\mu} . \tag{8.48}$$

Comparing Eqs. (8.47) and (8.48), we find that

$$\mu = \pm\cos^{-1}b = \pm\cos^{-1}(1-d/2f). \tag{8.49}$$

The solution of Eq. (8.47) is harmonic when $|b| \leq 1$. The particle displacement at the cell boundaries is given by the real part of Equation 8.45,

$$x_n = x_0 \cos(n\mu + \varphi). \tag{8.50}$$

Equation (8.50) gives the displacement measured at a cell boundary. It does not imply that particle orbits between boundaries are harmonic. In the thin-lens array, it is easy to see that orbits are straight lines that connect the points of Eq. (8.45). The quantity μ is called the *phase advance* in a focusing cell. The meaning of the phase advance is illustrated in Figure 8.10. The case shown has $\mu = 2\pi/7 = 51.4°$. Particle orbits between cell boundaries in other focusing systems are generally not straight lines. Orbits in quadrupole lens arrays are more complex, as we will see in Section 8.7.
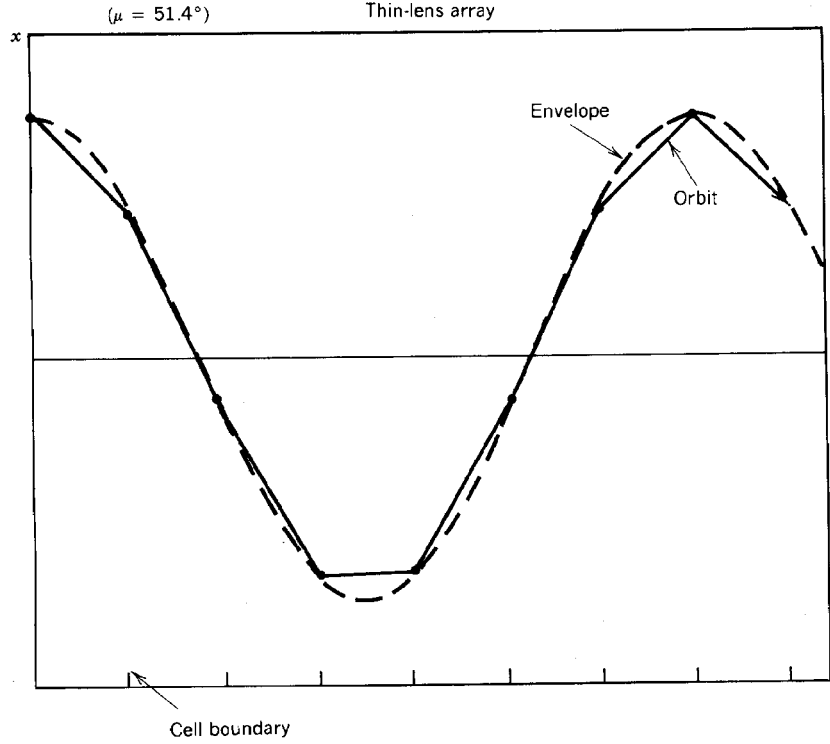
Figure 8.10 Particle orbit in a thin-lens array with phase advance per cell of 51.4°. Solid line: Actual particle orbit. Dotted line: Envelope function to calculate particle displacement at cell boundaries.

The orbit angle at cell boundaries can be determined by substituting Eq. (8.45) in Eq. (8.41). The result is

$$x_n^{/} = (x_o/d) \left(\exp[j(n+1)\mu] - \exp(jn\mu)\right) = (x_o/d) \exp(jn\mu) [\exp(j\mu)-1]. \qquad (8.51)$$

Note that when $\mu \Rightarrow 0$, particle orbits approach the continuous envelope function $x(z) = x_0 \cos(\mu z/d + \varphi)$. In this limit, the last factor in Eq. (8.51) is approximately $j\mu$ so that the orbit angle becomes

$$x_n^{/} = Re([jx_0\mu/d] [\exp(jn\mu)]) \cong -(x_0\mu/d) \sin(n\mu z/d). \qquad (8.52)$$

An important result of the thin-lens array derivation is that there are parameters for which all particle orbits are unstable. Orbits are no longer harmonic but have an exponentially growing displacment when
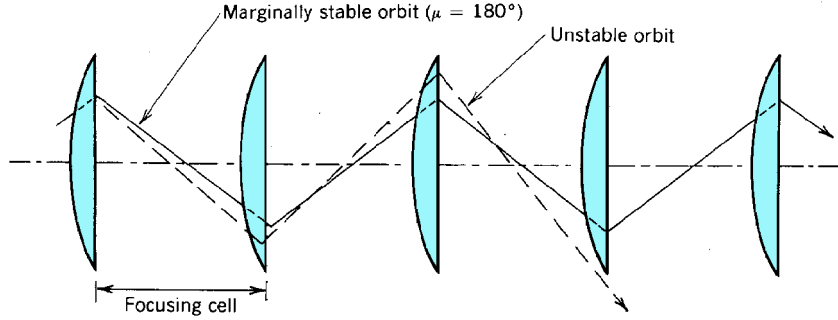
$$|b| = |1-d/2f| \geq 1. \qquad (8.53)$$

Figure 8.11   Orbital instability in a thin-lens array. Solid-line: Marginally stable orbit ($\mu \to 180°$). Dashed line: Unstable orbit resulting from a slight decrease of lens focal length.

Setting $1 - d/2f$ equal to -1 gives the following stability condition for transport in a thin-lens array,

$$f \geq d/4 \quad (stability). \tag{8.54}$$

There is a maximum usable lens strength for a given cell length. The physical interpretation of this instability can be visualized by reference to Figure 8.11. The lens system has $f = d/4$ so that the particle orbit is marginally stable. In this case, $b = -1$ and $\mu = 180°$. The orbit crosses the boundary with a displacement of equal magnitude but opposite sign. If the focusing strength of the lens is increased slightly ($f < d/4$), then the particle has an increased magnitude of displacement at each cell boundary as shown by the dotted line. The amplitude of displacement increases without limit.

8.6 RAISING A MATRIX TO A POWER

We want to generalize the treatment of the previous section to investigate orbits and stability properties for any linear focusing system. Focusing cells may be complex in high-energy accelerators. They may include quadrupole lenses, bending magnets, gradient fields, and edge focusing. Nonetheless, the net effect of a focusing cell can be represented by a single 4×4 transfer matrix no matter how many sequential elements it contains. When transverse motions along Cartesian coordinates are decoupled, each direction is separately characterized by a 2×2 matrix.

   A periodic focusing system consists of a series of identical cells. We shall restrict consideration to transport in the absence of acceleration. This applies directly to storage rings, beamlines, and electron confinement in a microwave tube. It is also a good approximation for accelerators if the betatron wavelength is short compared to the distance over which a particle's energy is doubled.

   If a particle enters a periodic channel with an orbit vector $\boldsymbol{u}_0$, then the vector at the boundary between the first and second focusing cells is $\boldsymbol{u}_1 = \boldsymbol{C}\boldsymbol{u}_0$. The quantity $\boldsymbol{C}$ is the transfer matrix for a cell. After traversing n cells, the orbit vector is

$$u_n = C^n u_0. \tag{8.55}$$

The quantity C^n denotes the matrix multiplication of C by itself n times. The behavior of particle orbits in periodic focusing systems is determined by the matrix power operation. In particular, if all components of C^n are bounded as $n \Rightarrow \infty$, then particle orbits are stable.

Analytic expressions for even small powers of a matrix can rapidly become unwieldy. The involved terms encountered in matrix multiplication are evident in Eqs. (8.33) and (8.34). We must use new methods of analysis to investigate the matrix power operation. We will concentrate on 2×2 matrices; the extension to higher-order matrices involves more algebra but is conceptually straightforward. We have already encountered the determinant of a matrix in Section 8.2. The determinant of a transfer matrix is always equal to unity when there is no acceleration. Another useful quantity is the *trace* of a matrix, defined as the sum of diagonal elements. To summarize, if

$$C = \begin{bmatrix} c_{11} & c_{12} \\ c_{21} & c_{22} \end{bmatrix},$$

then

$$\det C = c_{11}c_{22} - c_{12}c_{21} \tag{8.56}$$

and

$$Tr\ C = c_{11} + c_{22}. \tag{8.57}$$

Transfer matrices have *eigenvalues* and *eigenvectors*. These quantities are defined in the following way. For most square matrices, there are orbit vectors and numerical constants that satisfy the equation

$$C\ \mathbf{v}_i = \lambda_i\ \mathbf{v}_i. \tag{8.58}$$

The vectors for which Eq. (8.58) is true are called eigenvectors (characteristic vectors) of the matrix. The numerical constants (which may be complex numbers) associated with the vectors are called eigenvalues.

The following results are quoted without proof from the theory of linear algebra. The order of a square matrix is the number of rows (or columns). A square matrix of order m with nonzero determinant has m eigenvectors and m different eigenvalues. The eigenvectors have the property of *orthogonality*. Any m-dimensional orbit vector can be represented as a linear combination of eigenvectors. In the case of a 2×2 transfer matrix, there are two eigenvectors. Any orbit vector

184

at the entrance to a periodic focusing system can be written in the form

$$\boldsymbol{u_0} = a_1 \, \boldsymbol{v_1} + a_2 \, \boldsymbol{v_2}. \tag{8.59}$$

If the orbit given by the input vector of Eq. (8.59) passes through n focusing cells of a periodic system, it is transformed to

$$\boldsymbol{u_0} = \boldsymbol{C}^n \, \boldsymbol{u_0} = a_1 \, \lambda_1^n \, \boldsymbol{v_1} + a_2 \, \lambda_2^n \, \boldsymbol{v_2}. \tag{8.60}$$

Equation (8.60) demonstrates the significance of the eigenvector expansion for determining the power of a matrix. The problem of determining the orbit after a large number of focusing cells is reduced to finding the power of two numbers rather than the power of a matrix. If λ_1^n and λ_2^n are bounded quantities for $n \gg 1$, then orbits are stable in the focusing system characterized by the transfer matrix $\boldsymbol{C}$.

The eigenvalues for a 2 x 2 matrix can be calculated directly. Writing Eq. (8.58) in component form for a general eigenvector (v, v'),

$$(c_{11} - \lambda) \, v + c_{12} \, v' = 0, \tag{8.61}$$

$$c_{21} \, v + (c_{22} - \lambda) \, v' = 0. \tag{8.62}$$

Multiplying Eq. (8.62) by $c_{12}/(c_{22} - \lambda)$ and subtracting from Eq. (8.61), we find that

$$\frac{(c_{11} - \lambda) \, (c_{22} - \lambda) \, - \, c_{12} c_{21}}{(c_{22} - \lambda)} \, v = 0. \tag{8.63}$$

Equation (8.63) has a nonzero solution when

$$(c_{11} - \lambda) \, (c_{22} - \lambda) \, - \, c_{12} c_{21} = 0. \tag{8.64}$$

This is a quadratic equation that yields two values of λ. The values can be substituted into Eq. (8.61) or (8.62) to give v_1' in terms of v_1 and v_2' in terms of v_2. Equation (8.64) can be rewritten

$$\lambda^2 - \lambda \, Tr\boldsymbol{C} + \det\boldsymbol{C} = 0. \tag{8.65}$$

The solution to Eq. (8.65) can be found from the quadratic formula using the fact that $\det\boldsymbol{C} = 1$.

$$\lambda_1, \lambda_2 = (Tr\boldsymbol{C}/2) \pm \sqrt{(Tr\boldsymbol{C}/2)^2 - 1}. \tag{8.66}$$

185

The product of the two eigenvalues of Eq. (8.66) is

$$\lambda_1\,\lambda_2 \;=\; (TrC/2)^2 \;-\; [(TrC/2)^2 - 1] \;=\; 1. \tag{8.67}$$

The fact that the product of the eigenvalues of a transfer matrix is identically equal to unity leads to a general condition for orbital stability. We know that the eigenvalues are different if *detC* and *TrC* are nonzero. If both eigenvalues are real numbers, then one of the eigenvalues must have a magnitude greater than unity if the product of eigenvalues equals 1. Assume, for instance, that $\lambda_1 > 1$. The term λ_1 will dominate in Eq. (8.60). The magnitude of the orbit displacement will diverge for a large number of cells so that orbits are unstable. Inspecting Eq. (8.65), the condition for real eigenvalues and instability is $|TrC/2| > 1$.

When $|TrC/2| \leq 1$, the square root quantity is negative in Eq. (8.65) so that the eigenvalues are complex. In this case, Eq. 8.66 can be rewritten

$$\lambda_1,\lambda_2 \;=\; (TrC/2) \;\pm\; j\,\sqrt{1 - (TrC/2)^2}. \tag{8.68}$$

If we make the formal substitution

$$TrC/2 \;=\; \cos\mu, \tag{8.69}$$

then Eq. (8.68) becomes

$$\lambda_1,\lambda_2 \;=\; \cos\mu \;\pm\; j\,\sin\mu \;=\; \exp(\pm j\mu).. \tag{8.70}$$

Euler's formula was applied to derive the final form. The eigenvalues to the *n*th power are *exp(±njμ)*. This is a periodic trigonometric function. The magnitude of both eigenvalues is bounded for all powers of *n*. Thus, the orbit displacement remains finite for n $\Rightarrow \infty$ and the orbits are stable. To reiterate, if the action of a cell of a periodic focusing system is represented by a transfer matrix **C**, then orbits are stable if

$$|TrC/2| \;\leq\; 1 \quad (\textit{stability}). \tag{8.71}$$

This simple rule holds for any linear focusing cell.

We have concentrated mainly on mathematics in this section. We can now go back and consider the implications of the results. The example of the drift space and thin lens will be used to illustrate application of the results. The transfer matrix is

$$C \;=\; \begin{bmatrix} 1 & d \\ -1/f & 1-d/f \end{bmatrix}. \tag{8.72}$$

The determinant is equal to unity. The trace of the matrix is $TrC = 2 - d/f$. Applying Eq. (8.71), the condition for stable orbits is

$$|1 - d/2f| \leq 1, \tag{8.73}$$

as we found before. Similarly, $\cos\mu = 1 - d/2f$. Thus, the parameter μ has the same value as Eq. (8.49) and is associated with the phase advance per cell. This holds in general for linear systems. When the orbits are stable and the eigenvalues are given by Eq. (8.70), the orbit vector at the cell boundaries of any linear focusing cell is

$$\mathbf{u}_n = a_1 \mathbf{v}_1 \exp(jn\mu) + a_2 \mathbf{v}_2 \exp(-jn\mu). \tag{8.74}$$

The solution is periodic; orbits repeat after passing through $N = 2\pi/\mu$ cells.

The eigenvectors for the transfer matrix [Eq. (8.72)] can be found by substituting the eigenvalues in Eq. (8.61). The choice of v is arbitrary. This stands to reason since all orbits in a linear focusing system are similar, independent of magnitude, and the eigenvectors can be multiplied by a constant without changing the results. Given a choice of the displacement, the angle is

$$v' = (\lambda - c_{11}) \, v \, / \, c_{12}. \tag{8.75}$$

The eigenvectors for the thin-lens array are

$$\mathbf{v_1} = (\ 1, [\exp(j\mu) - 1]/d\ ), \tag{8.76}$$

$$\mathbf{v_2} = (\ 1, [\exp(-j\mu) - 1]/d\ ), \tag{8.77}.$$

Suppose we wanted to treat the same orbit considered in Section 8.5 [Eq. (8.45)]. The particle enters the first cell parallel to the axis with a displacement equal to x_0. The following linear combination of eigenvectors is used.

$$\mathbf{u}_o = x_0 \, \mathbf{v_1}. \tag{8.78}$$

The displacement after passing through n cells is

$$x_n = x_0 \, Re[\exp(jn\mu)] = x_0 \, \cos(n\mu). \tag{8.79}$$

as we found from the finite difference solution. The angle after n cells is

$$x_n' = x_0 \, \exp(jn\mu) \, [\exp(j\mu) - 1]/d. \tag{8.80}$$

The expression is identical to Eq. (8.51). Both models lead to the same conclusion. We can now proceed to consider the more complex but practical case of *FD* quadrupole focusing cells.

8.7 QUADRUPOLE FOCUSING CHANNELS

Consider the focusing channel illustrated in Figure 8.12. It consists of a series of identical, adjacent quadrupole lenses with an alternating 90' rotation. The cell boundary is chosen so that the cell consists of a defocusing section followed by focusing section (*DF*) for motion in the *x* direction. The cell is therefore represented as *FD* in the *y* direction. Note that individual lenses do not comprise a focusing cell. The smallest element of periodicity contains both a focusing and a defocusing lens. The choice of cell boundary is arbitrary. We could have equally well chosen the boundary at the entrance to an *F* lens so that the cell was an *FD* combination in the *x* direction. Another valid choice is to locate the boundary in the middle of the *F* lens so that focusing cells are quadrupole triplets, *FDF*. Conclusions related to orbital stability do not depend on the choice of cell boundary.

The transfer matrix for a cell is the product of matrices $\mathbf{C} = \mathbf{A}_F\mathbf{A}_D$. The individual matrices are given by Eqs. (8.4) and (8.6). Carrying out the multiplication,

$$\mathbf{C} = \begin{bmatrix} \cos\Gamma\cosh\Gamma + \sin\Gamma\sinh\Gamma & (\cos\Gamma\sinh\Gamma + \sin\Gamma\cosh\Gamma)/\sqrt{\kappa} \\ \sqrt{\kappa}(\cos\Gamma\sinh\Gamma - \sin\Gamma\cosh\Gamma) & \cos\Gamma\cosh\Gamma - \sin\Gamma\sinh\Gamma \end{bmatrix}. \tag{8.81}$$

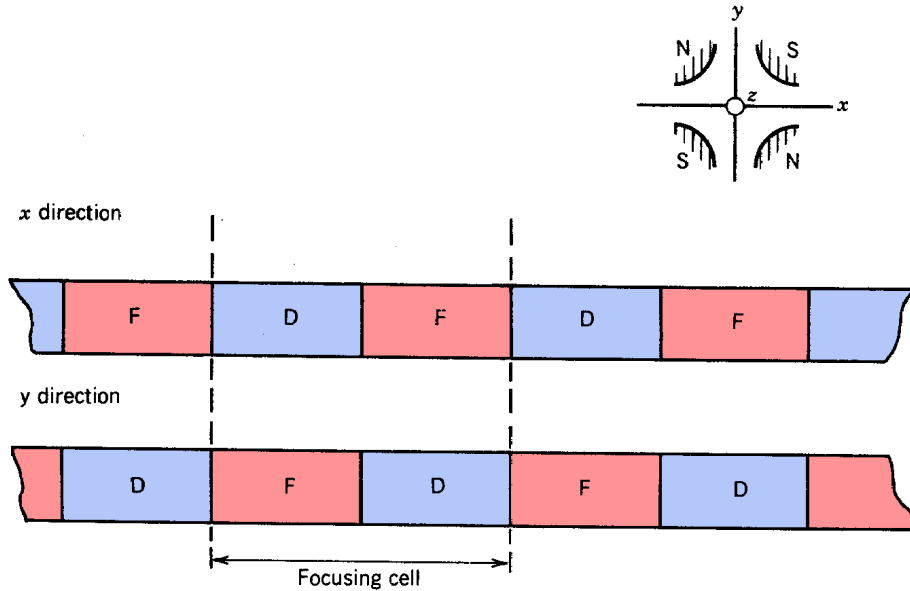where $\Gamma = \sqrt{\kappa}l$. Taking $|TrC/2| < 1$ the condition for stable orbits is

Figure 8.12 Array of quadrupole lenses in an FD configuration. Action of lenses indicated for motion in *x* and *y* directions.

$$-1 \leq \cos\Gamma \ \cosh\Gamma \leq +1. \tag{8.82}$$

Figure 8.13 shows a plot of $f(\Gamma) = \cos\Gamma \ \cosh\Gamma$ versus Γ. Only positive values of Γ have physical meaning. Orbits are stable for Γ in the range

$$0 \leq \Gamma \leq 1.86. \tag{8.83}$$

A stable orbit (calculated by direct solution of the equation of motion in the lens fields) is plotted in Figure 8.14a. The orbit has $\Gamma = 1$, so that $\mu = 0.584 = 33.5°$. Higher values of Γ correspond to increased lens strength for the same cell length. Orbits are subject to the same type of overshoot instability found for the thin-lens array [Eq. (8.53)]. An unstable orbit with $\Gamma = 1.9$ is plotted in Figure 8.14b. At higher values of Γ, there are regions of Γ in which stable propagation can occur. Figure 8.14c illustrates a stable orbit with $\Gamma = 4.7$ ($\mu = 270°$). Orbits such as those of Figure 8.14c strike a fragile balance between focusing and defocusing in a narrow range of Γ. Higher-order stability bands are never used in real transport systems. For practical purposes, Γ must be in the range indicated by Eq. (8.83). The same result applies to motion in the y
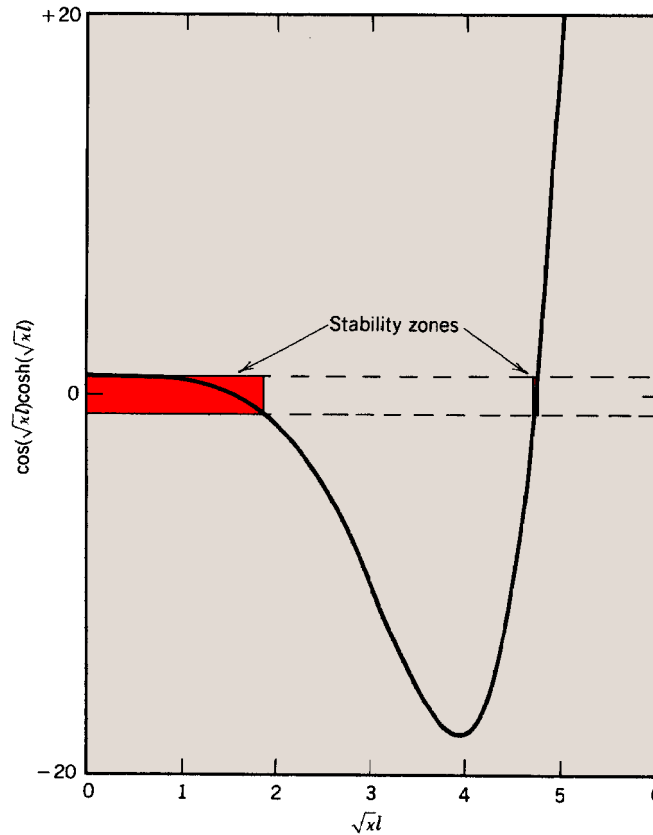

Figure 8.13 Orbital stability in an FD quadrupole array. Plot of $\cos(\sqrt{\kappa}\,l)\cosh(\sqrt{\kappa}\,l)$ versus $\sqrt{\kappa}\,l$.
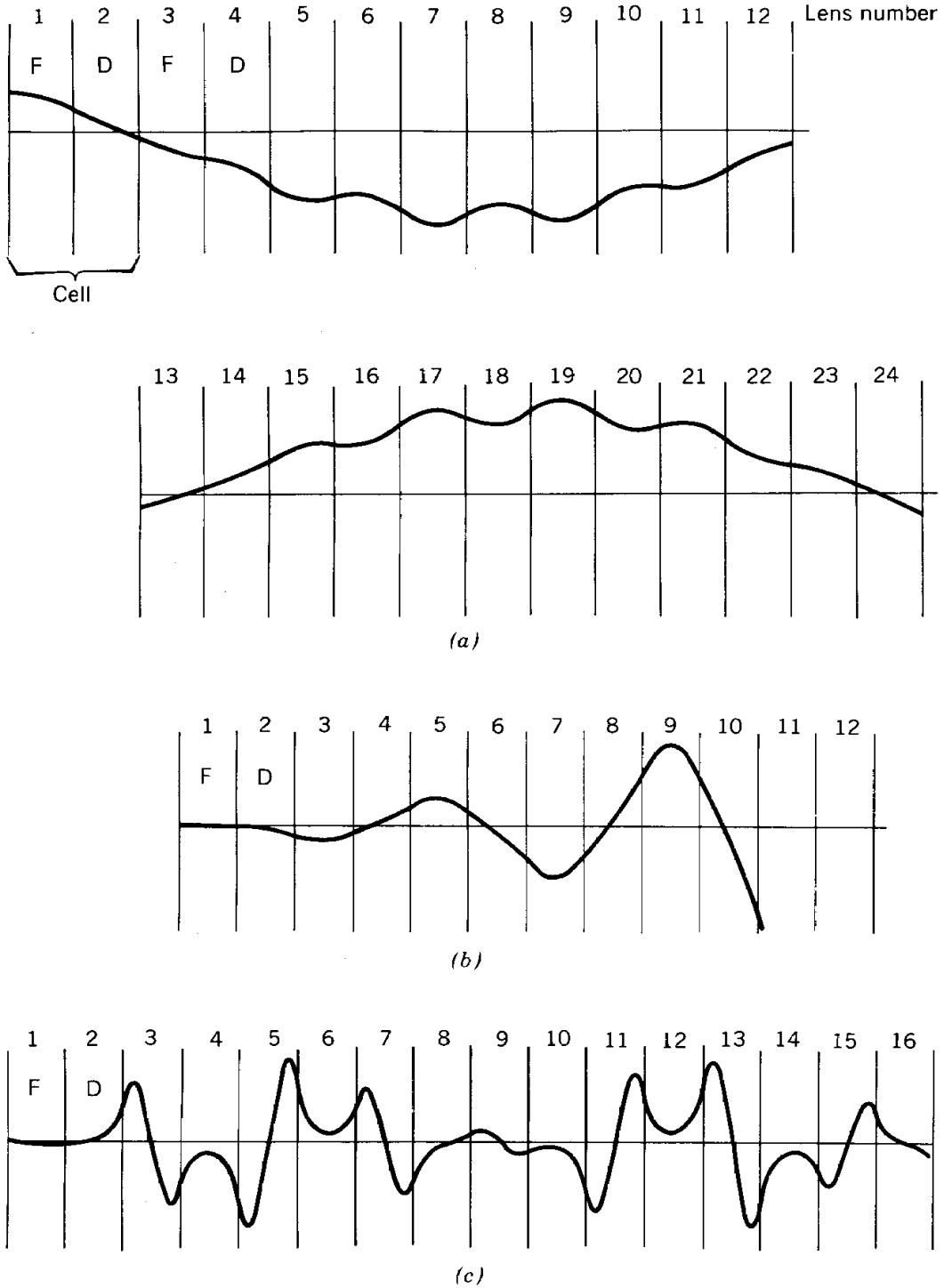
Figure 8.14 Numerical calculations of actual particle orbits in an FD quadrupole array. (a) $\sqrt{\kappa}\, l = 1$ (stable orbit, first passband). (b) $\sqrt{\kappa}\, l = 1.9$ (unstable orbit). (c) $\sqrt{\kappa}\, l = 4.7$ (stable orbit, second passband).

190

direction. The matrix coefficients are different from those of Eq. (8.81), but the quantity *TrC/2* is the same.

   Given a range of Γ for stable operation, it remains to determine an optimum value. Small phase advance ($\mu \ll 1$) has advantages. The effect of any one lens is small so that orbits approach the continuous focusing limit (Section 7.1). Beam envelope oscillations in a cell are small, and particle orbits are less affected by errors and misalignments of the lenses. Small μ is an effective choice for an array of lenses with positive focal length, such as the thin-lens array discussed in Section 8.5. The thin-lens array is a good model for a series of solenoidal magnetic lenses or unipotential electrostatic lenses. In such lens arrays, we can show that to first order the focusing strength is independent of μ for given applied fields. The focusing strength is proportional to the average transverse force that the lenses exert on the particles [Eq. (7.6)]. Neglecting edge fields, the focal length of a solenoidal lens is inversely proportional to the length of the lens, *d*. Thus, the product *fd* in Eq. (7.6) does not depend on the number of individual lenses per unit axial length. In other words, given a series of solenoids with phase advance μ, focal length *f*, and lens length *d*, the acceptance would be unchanged if the lens length and phase advance were halved and the focal length were doubled. Thus, it is generally best to use small phase advance and a fine division of cells in channels with only focusing lenses. The minimum practical cell length is determined by ease of mechanical construction and the onset of nonlinearities associated with the edge fields between lenses.

   This conclusion does not apply to *FD*-type focusing channels. In order to investigate scaling in this case, consider the quadrupole doublet treated using the expansions for small $\sqrt{\kappa}l$ [Eqs. (8.7), (8.8), and (8.35)]. In this approximation, the doublet consists of two lenses with focal lengths

$$f_F = +1/\kappa l, \qquad f_D = -1/\kappa l,$$

separated by a distance *l*. As with the solenoidal lens, the focal lengths of the individual lenses are inversely proportional to the lengths of the lens. The net positive focal length of the combination from Eqs. (8.36) and (8.37) is

$$f_{FD} = 3/2\kappa^2 l^3 = 3| f_F f_D |/2l \sim 1/d^3. \tag{8.84}$$

where *d = 2l* is the cell length.

   If we divide the quadrupole doublet system into smaller units with the same applied field, the scaling behavior is different from that of the solenoid channel. The average focusing force decreases, because the product $f_{FD}d$ is proportional to d^{-2}. This scaling reflects the fact that the action of an *FD* combination arises from the difference in average radius of the orbits in the *F* and *D* sections. Dividing the lenses into smaller units not only decreases the focusing strength of the *F* and *D* sections but also reduces the relative difference in transverse displacement. The conclusion is that *FD* focusing channels should be designed for the highest acceptable value of phase advance. The value used in practice is well below the stability limit. Orbits in channels with high μ are sensitive to misalignments and field errors. A phase advance of $\mu = 60°$ is usually

used.

In many strong focusing systems, alternate cells may not have the same length or focusing strength. This is often true in circular accelerators. This case is not difficult to analyze. Defining $\Gamma_1 = \sqrt{\kappa_1}\, l_1$ and $\Gamma_2 = \sqrt{\kappa_2}\, l_2$, the transfer matrix for motion in the *DF* direction is

$$
C = \begin{bmatrix} \cos\Gamma_1 & \sin\Gamma_1/\sqrt{\kappa_1} \\ -\sqrt{\kappa_1}\sin\Gamma_1 & \cos\Gamma_1 \end{bmatrix} \begin{bmatrix} \cosh\Gamma_1 & \sinh\Gamma_1/\sqrt{\kappa_1} \\ \sqrt{\kappa_1}\sinh\Gamma_1 & \cosh\Gamma_1 \end{bmatrix}. \tag{8.85}
$$

Performing the matrix multiplication and taking *TrC/2* gives the following phase advance:

$$
\cos\mu_{DF} = \cos\Gamma_1 \cosh\Gamma_2 + \left(\frac{\sin\Gamma_1 \, \sinh\Gamma_2}{2} \right) \left(\frac{\Gamma_2 l_1}{\Gamma_1 l_2} - \frac{\Gamma_1 l_2}{\Gamma_2 l_1} \right). \tag{8.86}
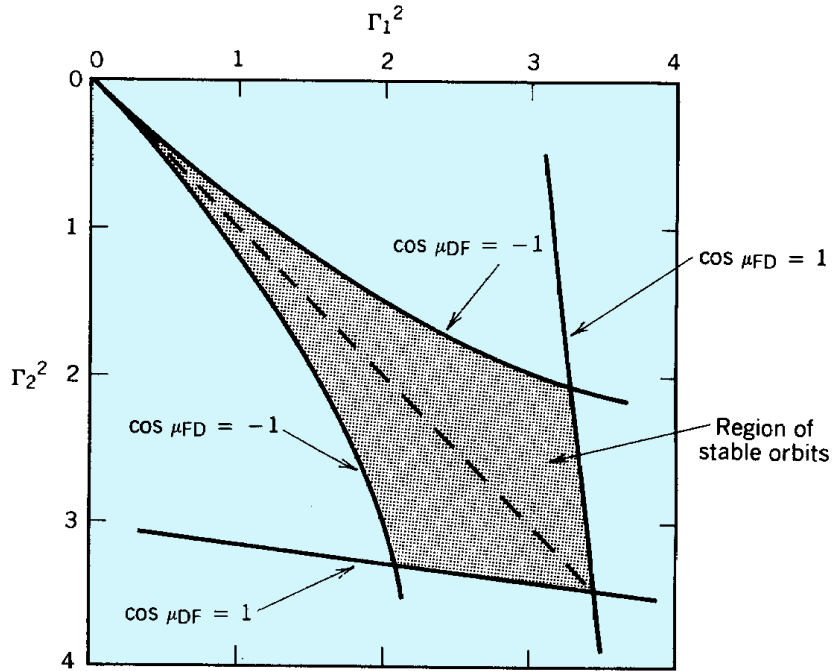$$

Figure 8.15 Necktie diagram. Orbital stability in an FD (DF) quadrupole array; the two lenses of a cell have unequal focusing strength. $\Gamma_1 = \sqrt{\kappa_1}\, l_1$, $\Gamma_2 = \sqrt{\kappa_2}\, l_2$. Region of parameter space with orbital stability in both x and y directions shaded. FD (lens 1 focusing, lens 2 defocusing), DF (lens 1 defocusing, lens 2 focusing).

Because the two lenses of the cell have unequal effects, there is a different phase advance for the *FD* direction, given by

$$\cos\mu_{FD} = \cosh\Gamma_1 \cos\Gamma_2 + \left(\frac{\sinh\Gamma_1 \sin\Gamma_2}{2} \right) \left(\frac{\Gamma_1 l_2}{\Gamma_2 l_1} - \frac{\Gamma_2 l_1}{\Gamma_1 l_2} \right). \tag{8.87}$$

There is little difficulty deriving formulas such as Eqs. (8.86) and (8.87). Most of the problem is
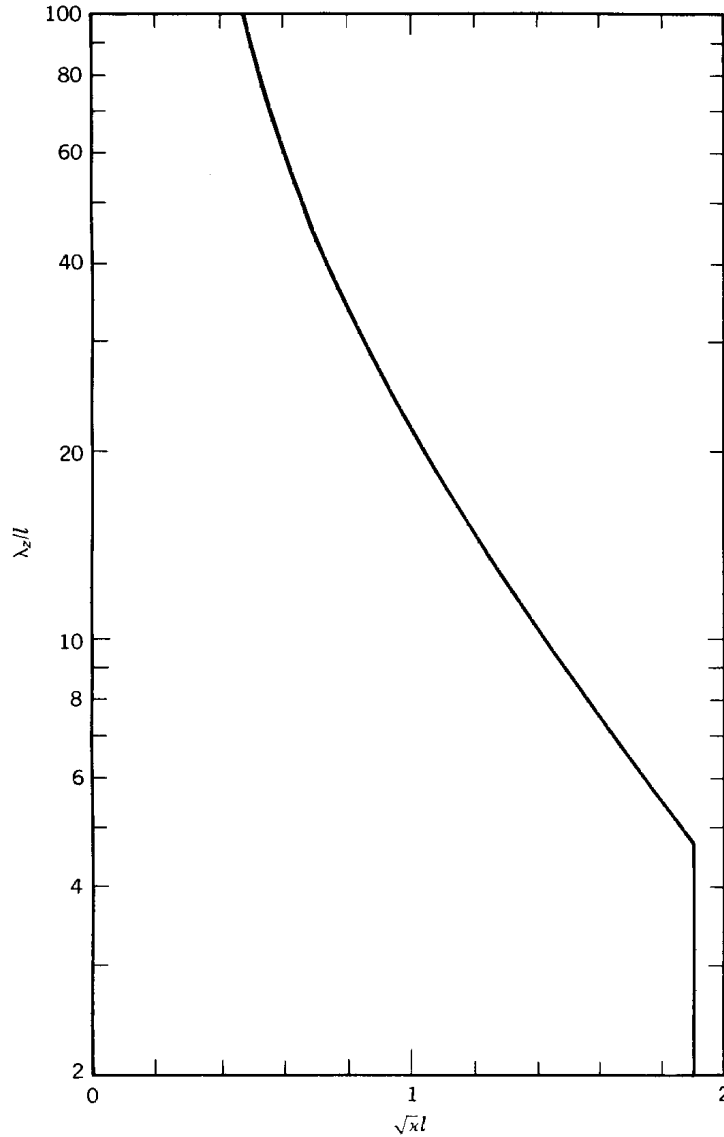

Figure 8.16 Betatron wavelength in a quadrupole focusing channel normalized to the length of a lens as a function of $\sqrt{\kappa_2}\, l$. FD channel with uniform lenses.

centered on plotting and interpreting the results. There are conditions in two directions that must be satisfied simultaneously for stable orbits:

$$-1 \leq \cos\mu_{FD} \leq +1, \qquad (8.88)$$

$$-1 \leq \cos\mu_{DF} \leq +1. \qquad (8.89)$$

The stability results are usually plotted in terms of $\Gamma_1{}^2$ and $\Gamma_2{}^2$ in a diagram such as Figure 8.15. This region of parameter space with stable orbits is shaded. Figure 8.15 is usually called a "necktie" diagram because of the resemblance of the stable region to a necktie, circa 1952. The shape of the region depends on the relative lengths of the focusing and defocusing lenses. The special case we studied with equal lens properties is a 45° line on the $l_1 = l_2$ diagram. The maximum value of Γ^2 is $(1.86)^2$. An accelerator designer must ensure that orbits remain well within the stable region for all regimes of operation. This is a particular concern in a synchrotron
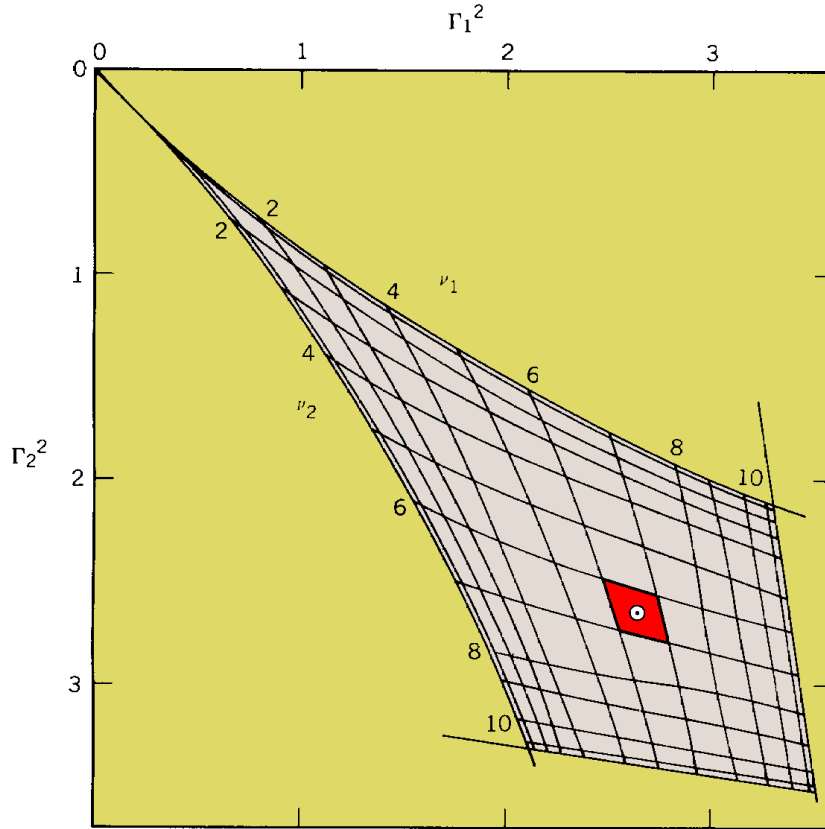

Figure 8.17 Beam focusing by an FD quadrupole array in a circular accelerator. Necktie diagram with conditions for orbital resonances included (24 cells per revolution). Possible operating point indicated at $\nu = 6.4$. (M. S. Livingston and J. P. Blewett, *Particle Accelerators*, used by permission, McGraw-Hill Book Co.).

where the energy of particles and strength of the focusing field varies during the acceleration cycle.

The betatron wavelength for orbits in a quadrupole channel is

$$\lambda_z = (2\pi d/\mu), \tag{8.90}$$

where d is the cell length and $d = 2l$. When F and D cells have the same parameters, Eq. (8.90) can be written

$$\lambda_z = \frac{2\pi d}{\cos^{-1}(\cos\Gamma\cosh\Gamma)}. \tag{8.91}$$

The quantity λ_z/l is plotted in Figure 8.16 as a function of Γ. The betatron wavelength is Important in circular machines. Particles may suffer resonance instabilities when the circumference of the accelerator or storage ring is an integral multiple of the betatron wavelength (Section 7.3). If we include the possibility of different focusing properties in the horizontal and verticle directions, resonance instabilities can occur when

$$\mu_{DF} = 2\pi n \ (d/C) \tag{8.92}$$

or

$$\mu_{FD} = 2\pi n \ (d/C) \tag{8.93}$$

with $n = 1,2,3,4,...$. Equations (8.92) and (8.93) define lines of constant $\cos\mu_{DF}$ or $\cos\mu_{FD}$, some of which are inside the region of general orbital stability. These lines, are included in the necktie diagram of Figure 8.17. They have the same general orientation as the lines $\cos\mu_{DF} = -1$ or $\cos\mu_{FD} = +1$. The main result is that particle orbits in a circular machine with linear FD forces must remain within a quadrilateral region of Γ_1-Γ_2 space. If this is not true over the entire acceleration cycle, orbital resonance instabilities may occur with large attendant particle losses.